Indirect Dimethyl Ether Production from Methanol Dehydration Reaction Using RHO and KFI-type Zeolites

by

Alireza Lotfollahzade Moghaddam

A Thesis in the Department of
Chemical and Materials Engineering

Presented in Partial Fulfillment of the Requirements
For the Degree of
Master of Applied Science (Chemical Engineering)

at Concordia University
Montreal, Quebec, Canada

Aug, 2023
© Alireza Lotfollahzade Moghaddam, 2023

CONCORDIA UNIVERSITY
School of Graduate Studies

This is to certify that the thesis prepared

By: Alireza Lotfollahzade Moghaddam

Entitled: Indirect Dimethyl Ether Production from Methanol Dehydration Reaction Using RHO and KFI-type Zeolites

and submitted in partial fulfillment of the requirements for the degree of

Master of Applied Science (Chemical Engineering)

complies with the regulations of the University and meets the accepted standards with respect to originality and quality.

Signed by the final examining committee:

Dr. Pantcho Stoyanov — Chair

Dr. Yaser Khojasteh — Examiner

Dr. Ashlee Howarth — Examiner

Dr. Melanie Hazlett — Thesis Supervisor(s)

Thesis Supervisor(s)

Approved by Dr. Sana Jahanshahi Anbuhi — Chair of Department or Graduate Program Director

Dr. Mourad Debbabi — Dean of Gina Cody School of Engine

Abstract

Indirect Dimethyl Ether Production from Methanol Dehydration Reaction Using RHO and KFI-type Zeolites

Alireza Lotfollahzade Moghaddam

The growing concern about environmental pollution necessitates the development of renewable and eco-friendly energy sources. Dimethyl ether (DME) has emerged as a promising alternative to diesel and LPG fuels and as a hydrogen carrier due to its favorable characteristics, such as high cetane number, oxygen content, absence of C-C bonds, and low CO and NOx emissions during combustion. Industrial DME production involves methanol dehydration, which requires a solid acid catalyst.

Common catalysts used in this process include γ-Al_2O_3 and ZSM-5 zeolite. However, γ-Al_2O_3 exhibits limited activity at lower temperatures, while ZSM-5 suffers from rapid deactivation and coke formation. Heteropoly acids have also been investigated as solid acid catalysts, but their low surface area limits their activity. Therefore, catalysts with increased acidity and improved selectivity towards DME are sought to enhance conversion efficiency and stability.

In this study, the use of alternative zeolites including KFI and RHO with varying crystallization times and template amounts was explored for methanol dehydration compared against commercial ZSM-5 and alumina catalysts. Steady-state methanol conversion experiments were carried out at 130 - 220°C using 30% methanol in an Ar balance. Long-term stability tests lasting 100 h were performed, and the catalysts were analyzed using SEM, EDS, XRD, BET, NH3-TPD, and TGA techniques.

The KFI and RHO zeolites exhibited equilibrium conversion (>90%) at lower temperatures (180-200°C) and demonstrated stability for more than 100 and 60 h, respectively. These outcomes can be attributed to high crystallinity, optimized crystal size, and large surface area resulting from the optimized synthesis process.

Acknowledgements

I would like to express my heartfelt gratitude to my supervisor, Dr. Melanie Hazlett, for her unwavering support, invaluable guidance, and tremendous patience throughout my thesis journey. Her expertise and mentorship have been instrumental in shaping my research experience and making it truly fulfilling.

I would also like to extend my appreciation to Dr. Jan Kopyscinski for his support and for providing the necessary setup and laboratory facilities to conduct my experiments. His assistance has been invaluable in conducting my research effectively.

I am grateful to Mr. Mohammad Ghavipour, a graduate student at McGill, for his assistance in the theoretical aspects of my experiments and for his contributions to the various experimental procedures. His expertise and collaboration have significantly enhanced the quality of my work.

I would like to express my appreciation to NSERC and Concordia University for their financial support, which has enabled me to pursue my research endeavors.

Lastly, I am deeply grateful to my family for their unwavering support, understanding, and unconditional love. Their patience and encouragement have been a constant source of strength throughout my thesis journey.

Dedication

I dedicate this thesis to my mother and father for their love and support throughout my life.

Contribution of Authors

1. Author: Alireza Lotfollahzade Moghaddam
- Reviewed literature related to the research topic.
- Planned the project, including experimental design and methodology.
- Synthesized the zeolite materials used in the project.
- Assisted in performing reactor experiments.
- Carried out characterization tests on the samples including SEM, EDS, TGA, and DRIFTS.
- Analyzed the experimental results.
- Wrote the papers based on the findings.
- Worked under the supervision and assistance of Dr. Melanie Hazlett, who served as the main supervisor for the project. Dr. Melanie Hazlett monitored all activities and progress, providing guidance and support throughout the research.

2. Author: Mohammad Ghavipour
- Conducted reactor experiments specifically related to the methanol to dimethyl ether conversion and NH_3-TPD (temperature-programmed desorption) experiments.
- Assisted in the interpretation and analysis of the experimental results.

3. Author: Dr. Jan
- Provided facilities and resources for the reactor experiments.
- Provided theoretical guidance and assistance.

4. Author: Dr. Melanie Hazlett
- The supervisor for the project.
- Monitored all project activities and progress.
- Assisted in performing well in all steps of the research.
- Provided theoretical and financial support to ensure the successful completion of the project.

Please note that the contributions mentioned above are not an exhaustive list of all the tasks and responsibilities undertaken by each author. The contributions mentioned reflect the major areas of involvement for each author in the context of the thesis project.

It is important to acknowledge and appreciate the collective effort of all the authors in contributing to the successful completion of the research project.

Table of Contents

List of Tables ix
List of Figures x
List of Symbols xv
CHAPTER 1: INTRODUCTION 1
CHAPTER 2: LITERATURE REVIEW 4
2.1 DME as an alternative energy source 4
2.2 DME production 8
2.3 Catalysts for methanol dehydration 11
2.3.1 Alumina as a methanol dehydration catalyst 13
2.3.2 Heteropoly Acids as methanol dehydration catalysts 17
2.4 Zeolites properties and synthesis 21
2.4.1 Introduction to zeolite properties and synthesis 21
2.4.2 Zeolites for Methanol Dehydration 26
CHAPTER 3: METHODOLOGY 37
3.1 Zeolite synthesis 37
3.2 Methanol dehydration reactions 39
3.3 Catalyst characterization 41
3.3.1 XRD 41
3.3.2 NH_3-TPD 43
3.3.3 DRIFTS 45
3.3.4 SEM 47
3.3.5 TGA 49
3.3.6 BET surface area and pore size distribution 50
CHAPTER 4: DME PRODUCTION USING METHANOL OVER RHO-TYPE ZEOLITE WITH DIFFERENT PREPARATION METHODS 53
4.1 Abstract 53
4.2 Introduction 53
4.3 Experimental 56
4.3.1 Catalyst synthesis 56

4.3.2 Characterization 57
4.3.3 Activity experiments 59
4.4 Results and discussion 60
4.4.1 Characterization 60
4.4.2 Catalytic activity 65
4.5 Conclusions 76
CHAPTER 5: THE EFFECT OF TEMPLATE AND CRYSTALLIZATION TIME ON KFI-TYPE ZEOLITE ACTIVITY FOR METHANOL DEHYDRATION TO DME 77
5.1 Abstract 77
5.2 Introduction 77
5.3 Experimental 80
5.3.1 Catalyst preparation 80
5.3.2 Characterization 82
5.3.3 Catalytic activity 83
5.4 Results and discussion 84
5.4.1 Characterization 84
5.4.2 Catalytic Activity 90
5.5 Conclusions 101
CHAPTER 6: CONCLUSIONS AND FUTURE WORK 103
6.1 Conclusions 103
6.2 Future Work 104
REFERENCES 105
APPENDICES 122
Appendix A: XRD Pattern of RHO Zeolites, Particle Size Distributions, and Reproducibility Experiments 122

List of Tables

Table 1. The physical and chemical properties of diesel, LPG, and DME for energy source applications [31]..... 8

Table 2. The acidity and surface area of different catalysts used for methanol dehydration. 28

Table 3. The molar ratio of precursors in initial gel, hydrothermal synthesis temperature, and crystallization time for different samples 38

Table 4. PhysicoChemical features of synthesized and commercial catalysts. 64

Table 5. Numerical result of NH_3-TPD analysis for acidity measurement..... 65

Table 6. Chemical and physical properties of investigated catalysts..... 88

Table 7. The acidity strength of synthesized and commercial zeolites [a] 90

Table 8. Methanol conversion at different temperature over commercial and synthesized zeolites 92

Table 9. Coke analysis and TOF calculated for various zeolites..... 100

List of Figures

Figure 1. Energy consumption over 1980 – 2021 years including (–) total, (–) Petroleum and other liquids, (–) coal, (–) natural gas, (–) renewable and biomass, (–), nuclear sources. [10] 5

Figure 2. DME production from different feedstocks through direct and indirect methods [8]..... 9

Figure 3. (A) Methanol Conversion vs. temperature over γ-Al_2O_3 catalyst: (a) without H_2O and (b) With 10% H_2O in the feed. (B) Impact of 10% H_2O addition in the feed on methanol conversion at T = 215 °C [81]. 14

Figure 4. The activity of different phases of alumina including η-Al_2O_3 (●), γ- Al_2O_3 (○), θ-Al_2O_3 (■), (χ + γ)- Al_2O_3 (□), δ- Al_2O_3 (▲), κ- Al_2O_3 (△) and α- Al_2O_3 (▼) for methanol dehydration [92]. 17

Figure 5. The a) methanol conversion (%) and b) DME production rate (mmol.h-1.gHSiW-1) using supported HSiW over SiO2, TiO_2, ZrO_2, Al_2O_3, BN, CeO_2 [71]..... 18

Figure 6. Methanol conversion at different temperatures over HPW (1), HSiW (2), and $Cs_{2.5}H_{0.5}PW$ (3) bulk catalysts, and the 20%HSiW/SiO_2 supported catalyst (4) under WHSV of 0.25 $g.g^{-1}.h^{-1}$ [95] 20

Figure 7. Methanol conversion and DME selectivity using 20%HSiW/SiO2 catalyst at 150 ℃ [95] 20

Figure 8. The framework structures and pore rings of frequently utilized zeolite types across diverse applications [102]. 22

Figure 9. Common employed methods to reach a zeolite type with different chemical, textural, and transport properties [99]. 24

Figure 10. Bronsted and Lewis acid sites creation in a zeolite structure[110–113] 25

Figure 11. The channel structure of a) EU-1 and b)MOR 1-D zeolites [120] 27

Figure 12. The amount of coke deposited over MOR (●), FER (○), and MFI (▲) under methanol dehydration reaction at 240 ℃ [72]. 30

Figure 13. The activity of different catalysts in a) methanol conversion and b) DME selectivity at 125 – 300 ℃ under the flow of 20 ml/min containing 4% methanol (~ WHSV of 0.5) [23]..... 31

Figure 14. Methanol dehydration vs. temperature using FER zeolites with different crystal sizes (M-FER = 5-10 μm, NP-FER = 0.30-0.50 μm, and NC-FER = 0.10 μm) [78]..... 32

Figure 15. DME yield at 180 – 320 ℃ over three samples of ZSM-5 (MFI) zeolite with different crystal sizes (Con-ZSM-5 = 1.2 µm, Meso-ZSM-5 = 0.30 µm, and Nano-ZSM-5 = 0.12 µm) [122] 33

Figure 16. The influence of alkaline treatment with different duration (1, 2, and 4 h) on ZSM-5 (MFI) activity toward a) methanol conversion and b) DME selectivity [23] 34

Figure 17. Teflon-lined stainless-steel bomb hydrothermal reactor 38

Figure 18. The schematic view of setup for DME production 40

Figure 19. The XRD patterns from (a) an amorphous and (b) a crystallized sample [132] 42

Figure 20. The theory of XRD and Bragg's law [134] 43

Figure 21. The common process of NH3-TPD test 44

Figure 22. IR spectroscopy methods including transmission IR (TIR), diffuse reflectance Fourier transform (DRIFTS), attenuated total reflection (ATR), and reflection-absorption IR (RAIRS) [137] 45

Figure 23. Hydroxyl, nitrile, and some other functional groups in a IR spectroscopy [137]. 46

Figure 24. The interaction of CN group in acetonitrile with Bronsted (1a and 1b) and Lewis (1c and 1d) acid sites [139] 47

Figure 25. Schematic drawing of an SEM instrument [141] 48

Figure 26. The 6 types of IUPAC classification for N_2 adsorption/desorption isotherms [146]. . 51

Figure 27. Calculating the $V_{micropores}$ and $S_{external}$ by t-plot method [150]. 52

Figure 28. XRD analysis of synthesized RHO zeolites using different conditions including (a) RHO_0T7, (b) RHO_0.5T10, (c) RHO_0.5T6, (d) RHO_0.5T8, (e) RHO_0.25T8, (f) RHO_0T8, (g) reference RHO [120]. 61

Figure 29. SEM results of crystallized RHO zeolites including (a) RHO_0T7, (b) RHO_0.5T10, (c) RHO_0.5T6, (d) RHO_0.5T8, (e) RHO_0.25T8, and (f) MFI_15. 62

Figure 30. The path of N_2 adsorption–desorption isotherms of synthesized zeolites: (a) RHO_0T7, (b) RHO_0.5T10, (c) RHO_0.5T6, (d) RHO_0.5T8, (e) RHO_0.25T8. 63

Figure 31. The NH_3-TPD profile of activated zeolites including (a) MFI_25, (b) MFI_15, (c) RHO_0T7, (d) RHO_0.5T10, (e) RHO_0.5T6, (f) RHO_0.5T8, (g) RHO_0.25T8. 65

Figure 32. Methanol dehydration at various temperatures using (●) RHO_0.5T8, (+) RHO_0.25T8, (▲) RHO_0T7, (×) SAPO-34, and (■) γ-Al_2O_3 catalysts with WHSV = 4 h^{-1}. 66

Figure 33. The activity of (□) RHO_0.5T10, (●) RHO_0.5T8, (△) RHO_0.5T6, (◆) MFI_15, and (○) MFI_25 zeolites in methanol dehydration reaction versus temperature with WHSV = 4 h^{-1} 68

Figure 34. Turnover frequency (h^{-1}) for RHO-type zeolites with different crystallization times and reference MFI zeolites 70

Figure 35. The conversion of methanol using (a) RHO_0.5T10, (b) MFI_15, (c) MFI_25, at their optimum temperatures for 100 h continuous reaction with WHSV = 4 h^{-1} (dash lines = conversion average over first 10 h) 71

Figure 36. SEM images of used catalysts before and after 100 h reaction including (a1) fresh KFI_1T7, (a2) used KFI_1T7, (b1) fresh MFI_15, (b2) used MFI_15, (c1) fresh MFI_25, (c2) used MFI_25. 72

Figure 37. TGA pattern recorded using (a) MFI_25, (b) MFI_15, (c) RHO_0.5T10 catalyst after 100 h reaction. 73

Figure 38. The assessment of Bronsted and Lewis types acidity of saturated samples with acetonitrile by FT-IR spectra (recorded spectra = black lines, peaks deconvolution: colorful lines): (a) MFI_25, (b) MFI_15, (c) RHO_0.5T10. 74

Figure 39. The composition of coke deposited on different zeolite types including (a) MFI_25, (b) MFI_25, (c) RHO_0.5T10 after 100 h reaction using dichloromethane. 75

Figure 40. XRD patterns of synthesized KFIs with different template amounts and hydrothermal processing time durations including (a) KFI_1T7, (b) KFI_1T3, (c) KFI_1T5, (d) KFI_0.5T5, (e) KFI_0T5, (f) reference from literature [195]. 85

Figure 41. SEM images of synthesized KFIs including (a) KFI_1T7, (b) KFI_1T3, (c) KFI_1T5, (d) KFI_0.5T5, (e) KFI_0T5, (f) MFI_15 86

Figure 42. N_2 adsorption–desorption isotherm patterns of (a) KFI_1T5, (b) KFI_0.5T5, (c) KFI_0T5 catalysts. 87

Figure 43. N_2 adsorption/desorption isotherm patterns of KFI with different crystallization times including (a) KFI_1T7, (b) KFI_1T5, (c) KFI_1T3. 88

Figure 44. NH_3-TPD pattern of (a) MFI_25, (b) MFI_15, (c) KFI_1T7, (d) KFI_1T3, (e) KFI_1T5, (f) KFI_0.5T5, (g) KFI_0T5 catalysts. 89

Figure 45. The catalytic activity of (■) KFI_1T5, (○) KFI_0.5T5, (◆) KFI_0T5, and (●) γ-Al_2O_3 for methanol dehydration at different temperature with WHSV = 4 h^{-1} 91

Figure 46. Methanol conversion versus temperature over (□) KFI_1T7, (■) KFI_1T5, (×) KFI_1T3, (▲) MFI_15, and (+) MFI_25 for methanol dehydration at different temperature with WHSV = 4 h^{-1} 93

Figure 47. The conversion of methanol using (a) KFI_1T7, (b) MFI_15, (c) MFI_25, at their optimum temperatures for 100 h continuous reaction with WHSV = 4 h^{-1} (dash lines = the average of first 10 h conversion). 96

Figure 48. SEM images of spent catalysts before and after 100 h reaction including (a1) fresh KFI_1T7, (a2) used KFI_1T7, (b1) fresh MFI_15, (b2) used MFI_15, (c1) fresh MFI_25, (c2) used MFI_25. 97

Figure 49. TGA path for spent (a) KFI_1T7 (b) MFI_15, (c) MFI_25 catalysts. 97

Figure 50. Turnover frequency calculated for KFI_1T7, MFI_15, and MFI_25 at low temperatures (130 – 170 °C) 98

Figure 51. IR Spectra of (a) MFI_25, (b) MFI_15, and (c) KFI_1T7 after saturation with acetonitrile (recorded pattern = solid line, after deconvolution = dash lines) 99

Figure 52. The results of coke analysis by GC-MS for (a) MFI_25, (b) MFI_15, (c) KFI_1T7.100

Figure 53. XRD patters of RHO zeolites including (a) RHO_0.5T10, (b) RHO_0.5T8, and (c) RHO_0.25T6 after activation by 1 M NH_4Cl solution. 122

Figure 54. Particle size distribution for RHO_0.5T6 using SEM images. 123

Figure 55. Particle size distribution for RHO_0.5T8 using SEM images 123

Figure 56. Particle size distribution for RHO_0.5T10 using SEM images 124

Figure 57. Particle size distribution for RHO_0.25T6 using SEM images 124

Figure 58. Particle size distribution for RHO_0T7 using SEM images. 125

Figure 59. Particle size distribution for MFI_25 using SEM images. 125

Figure 60. Particle size distribution for MFI_15 using SEM images. 126

Figure 61. Particle size distribution for KFI_1T3 using SEM images. 126

Figure 62. Particle size distribution for KFI_1T5 using SEM images. 127

Figure 63. Particle size distribution for KFI_1T7 using SEM images. 127

Figure 64. Particle size distribution for KFI_0.5T5 using SEM images. 128

Figure 65. Particle size distribution for KFI_0T5 using SEM images. 128

Figure 66. The methanol dehydration using prepared RHO_0.5T8 zeolites in two series at 130 – 220 °C with WHSV = 4 h^{-1}. 129

Figure 67. The methanol conversion over two different prepared KFI_1T5 samples at 130 – 220 °C with WHSV = 4 h^{-1}. 130

List of Symbols

Symbol	Definition
con	large crystal size in μm scale
DME	Dimethyl Ether
1-D	One Dimensional
2-D	Two Dimensional
3-D	Three Dimensional
CD3CN	Acetonitrile-d3
WHSV	Weight Hour Space Velocity
TPD	Temperature Programmed Desorption
FTIR	Fourier Transform Infrared
DRIFTS	Diffuse Reflectance Infrared Fourier Transform Spectroscopy
SAPO	Silico-alumino-phosphate
HPAs	Heteropoly Acids
SEM	Scanning Electron Microscopy
XRD	X-ray Diffraction
BET	Brunauer-Emmett-Teller
TGA	Thermo Gravimetric Analysis
EDS	Energy-Dispersive X-ray Spectroscopy
GC	Gas Chromatography
18-C-6	18-Crown-6 ($C_{12}H_{24}O_6$)
Syngas	$CO/CO_2/H_2$
quad Btu	quadrillion British thermal units
A/F	Air/Fuel Ratio
LPG	Liquefied Petroleum Gas
BN	Boron Nitride
W/S	Weak/Strong Acid Site Ratio
Alumina	Al_2O_3
DOE	Design of Experiments

AS/AC	Aluminum Content on/in Surface/Crystals Ratio
MFC	Mass Flow Controller
TOF	Turnover frequency

CHAPTER 1: INTRODUCTION

The escalating levels of environmental pollution in soil, air, and water have become a severe concern for humanity. The detrimental effects of pollution on ecosystems and human health are increasingly evident, making it imperative to address these issues with scientific rigor and urgency [1].

In addition to environmental pollution, ensuring a steady supply of sustainable energy sources is a crucial concern for societies today [2]. Although fossil fuels dominate energy consumption in a variety of industries, transportation, and households, their sustainability and renewability are in question. The heavy reliance on fossil fuels poses risks of resource exhaustion and unstable fuel prices, calling for more sustainable alternatives. Dimethyl Ether (DME) emerges as a viable solution to secure a stable and sustainable energy future for our societies [3]. By transitioning towards DME and other renewable energy sources, we can reduce our dependence on limited fossil fuels and foster a cleaner, more reliable energy landscape for future generations.

DME can be derived from syngas ($CO/CO_2/H_2$) through two distinct methods: direct and indirect [4]. In both methods, two catalysts are used, one for the synthesis of methanol from syngas and another for the subsequent dehydration of methanol into DME. In the indirect route (two steps), the catalysts are employed in separate reactors, while the direct route (one step) combines them in a single reactor. Each approach presents its own set of advantages and disadvantages, emphasizing the need for active and stable catalysts for each step. While this study does not delve into the method of combination or catalysts for methanol synthesis, it concentrates on the exploration of catalysts for the methanol dehydration reaction.

Initially, alumina served as the solid acid catalyst in industries [5]. However, its limitations, which will be addressed in the second chapter, prompted investigations into zeolite materials for the dehydration process. Zeolite compounds, classified as porous materials, exist in diverse types with varying physical and chemical properties. Their porous structure with high acidity and surface area makes them exceptionally valuable in environmental applications like water treatment and fuel production [6]. By employing different precursors and adjusting preparation factors, distinct types of zeolites with specific characteristics can be obtained [7]. Consequently, modifications in preparation parameters yield differences in pore size, acidity, crystal size, surface area, and more,

thereby influencing zeolites' catalytic activity for DME production and offering opportunities to enhance the overall process.

In this study, two promising zeolite framework types, KFI, and RHO, were synthesized and investigated for the methanol dehydration reaction. Multiple catalyst characterization techniques were employed to measure the acidity, surface area, crystallinity, crystal size, coke formation, and composition.

The primary objective of this thesis is to develop an optimal solid acid catalyst for methanol conversion to DME, ensuring thermodynamic conversion at low temperatures with 100% DME selectivity and an extended catalyst lifetime while minimizing the formation of by-products. Considering this objective, we prepared targeted catalysts using diverse preparation parameters to modify their physical and chemical properties, including acidity and surface area. Subsequently, their performance in methanol dehydration was evaluated through reactor experiments.

The contents of this thesis are divided into six chapters based on three manuscripts:

In the second chapter, recent developments in solid acid catalysts employed for DME production through methanol dehydration will be reviewed as well as a discussion of DME features that make it a promising alternative to current fossil fuels. A comprehensive review of direct and indirect DME synthesis pathways was recently published in the Journal of Environmental Chemical Engineering [8], for the purposes of this thesis the second chapter focuses mainly on the methanol dehydration reaction step.

In the third chapter, the research methodologies for zeolite synthesis, the chemical reactions and experimental conditions, and an overview of the catalyst characterization techniques used are provided.

The fourth chapter is a manuscript that will be submitted for publication, showing the results of RHO zeolite performance for methanol dehydration reaction. Synthesized RHO zeolites will be discussed in terms of their methanol conversion at different temperatures, the catalyst stability, and their physicochemical properties.

The fifth chapter is another manuscript that will be submitted for publication, which focuses on KFI zeolites' activity for DME production from methanol. The results of various characterization techniques as well as reactor experiments will be discussed in detail.

In the sixth chapter, conclusions from this work and recommendations for future work in the area of synthesizing zeolites for methanol dehydration.

CHAPTER 2: LITERATURE REVIEW

This chapter will give a review of how DME can be used as an alternative energy source, the pathways for dimethyl ether production, and examine various catalysts investigated for DME production. To gain insights into the catalyst activity in methanol dehydration, different catalysts for this reaction will be reviewed which will be compared to prepared catalysts in this study. Particular focus will be given to zeolites, as the primary focus of the work was to synthesis two types (KFI and RHO) to apply to DME production, particularly in the second step of the DME synthesis reaction of methanol dehydration.

2.1 DME as an alternative energy source

Human activities play a significant role in pollution generation, resulting in severe ecological imbalances. These activities encompass a wide range of industries, such as manufacturing, agriculture, transportation, and energy production. As these sectors expand to meet the demands of an ever-growing global population, the magnitude of pollution caused continues to intensify. Furthermore, the energy requirements of human activities contribute significantly to environmental pollution [9].

Figure 1 illustrates the alarming upward trajectory of total energy consumption over the past four decades [10]. From approximately 300 quad Btu (quadrillion British thermal units) in 1980, energy consumption has surpassed 600 quad Btu in 2021. This exponential increase is primarily driven by population growth, industrialization, and technological advancements, all of which demand higher energy inputs. Even though temporary reductions in energy production were observed during the COVID-19 pandemic (2020-2022) due to global lockdown measures, the overall trend of escalating energy consumption remains unchanged.

As shown in Figure 1, fossil fuels, such as coal, oil, and natural gas, have long been primary energy sources. This is due to their high energy density and ease of extraction. However, the extraction and use of fossil fuels release a multitude of pollutants into the environment. The extraction process can contaminate soil and water resources, causing significant environmental damage.

Moreover, fossil fuel combustion emits carbon dioxide (CO_2), sulfur dioxide (SO_2), nitrogen oxides (NOx), and particulates matter (PM), contributing to air pollution and climate change [11].

Fossil fuel use in industries, transportation, and households contributes significantly to increasing greenhouse gases in the atmosphere, worsening global warming and climate change. Recognizing these harmful effects, it is urgent to transition to cleaner energy sources. Despite advancements in renewable energy technologies, fossil fuel dependency remains deeply ingrained in global energy systems.

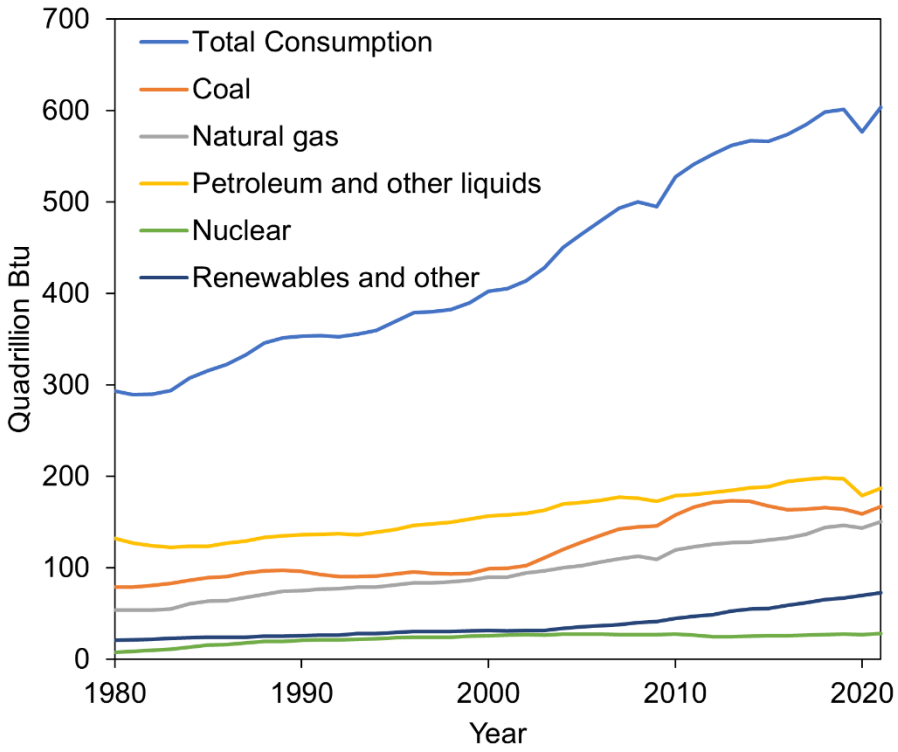

Figure 1. Energy consumption over 1980 – 2021 years including (–) total, (–) Petroleum and other liquids, (–) coal, (–) natural gas, (–) renewable and biomass, (–), nuclear sources. [10]

As the world seeks sustainable alternatives, renewable energy sources such as solar, hydro, and others offer promising solutions. However, it is imperative to acknowledge the fluctuating nature of these renewable sources, as they rely on specific conditions for optimal energy production [12]. In addition, hydrogen presents a potential source of energy in the future, but safe storage and transportation will be challenging.

Recognizing the urgent need to transition to cleaner energy sources, renewable energy technologies have gained momentum. Solar energy harnesses the abundant power of the sun to generate electricity through photovoltaic cells or concentrated solar power systems [13].

Hydroelectric power utilizes the force of flowing water, typically in the form of dams or turbines, to generate electricity [14]. Other renewable energy sources include wind power, which harnesses wind kinetic energy, and geothermal energy, which taps into heat from the Earth's core.

While renewable energy sources offer significant advantages, their intermittent nature poses challenges to maintaining a consistent energy supply. Solar energy production is dependent on sunlight availability, which is variable throughout the day and influenced by weather patterns. Similarly, wind power generation relies on wind current strength and consistency, which vary over time. These fluctuations in renewable energy availability require effective energy storage and grid integration systems to ensure a reliable and stable energy supply.

In recent years, hydrogen has emerged as a potential future energy source due to its high energy content and low emissions. Hydrogen can be produced through various methods, such as electrolysis, and used in fuel cells or combustion engines to generate electricity [15]. However, H_2 gas poses storage and transportation challenges. It is highly flammable and requires specialized infrastructure and safety measures for handling and distribution. To address hydrogen storage and transportation concerns, researchers have explored alternative methods. One promising solution involves storing hydrogen in other stable chemical forms, such as dimethyl ether (DME) [16].

DME is a clean-burning fuel that can serve as an energy source or carrier for hydrogen. It can be produced from various feedstocks, including natural gas, biomass, or waste, reducing reliance on fossil fuels and minimizing environmental impacts [16]. DME offers advantages such as high energy density, low toxicity, and compatibility with existing infrastructure for storage, distribution, and utilization.

DME has found versatile applications in various industries, serving as a propellant, coolant, alternative energy source, and intermediate for various chemicals. While DME is widely used as a propellant in aerosol products, its unique properties such as solvency power and water miscibility make it an excellent choice for this application [17]. As regulations restrict the use of hydrofluorocarbons (HFCs) in air-conditioning, heat pumps, and refrigeration systems due to their detrimental effects on global warming and the ozone layer, DME emerges as a promising alternative [18]. Although not commonly used as a refrigerant due to its flammability, DME exhibits favorable thermophysical properties such as high thermal conductivity, large latent heat, zero ozone depletion potential (ODP), and low global warming potential (GWP). The

incorporation of DME into CO_2/DME mixtures can reduce operating pressure in CO_2 heat pump/refrigeration systems, improving their coefficient of performance (COP), while CO_2 itself suppresses DME flammability.

In addition to its applications as a propellant and refrigerant, DME offers environmentally friendly features when used as a fuel. Compared to diesel, DME possesses greater latent heat of vaporization (467 kJ/kg vs. 300 kJ/kg), resulting in evaporative cooling upon injection into the engine cylinder [19]. This cooling effect leads to lower emissions of particulate matter and nitrogen oxides (NOx). Furthermore, DME's higher oxygen content promotes complete fuel combustion, while its substantially higher cetane number indicates improved ignition characteristics. These factors contribute to reduced emissions and enhanced combustion efficiency, making DME a promising fuel option with environmental advantages. Some of the remarkable and relevant properties of DME include [20–24]:

- high cetane index (ca. 55–60)
- lack of C─C bond
- producing no soot, no black smoke, or sulphur oxides (SOx)
- low emission of CO, nitrogen oxides (NOx)
- high oxygen content (34.8% by mass)
- auto-ignition temperature (350 °C) is quite close to the auto-ignition temperature of conventional diesel fuel
- low boiling point (−24.9 °C) → provides fast fuel/air mixing → reduction in the ignition delay
- non-carcinogenic, non-teratogenic, non-mutagenic, and non-toxic

Due to its similar characteristics to propane, butane, and liquefied petroleum gas (LPG), DME holds substantial promise as a fuel option for a wide range of applications including industries, households, and vehicles [25,26]. Its performance and pollutant emission levels have been found to be suitable for gas turbine applications, making it a viable fuel choice in this sector [27]. Moreover, with a cetane number (55 - 60) comparable to diesel (~ 45), DME serves as a feasible alternative to diesel [28–30]. The physical and chemical characteristics of DME, diesel and LPG have been provided in Table 1 from literature [31]. One of the notable advantages of DME over other suggested fuels is the minimal need for infrastructure modifications. This allows for its

immediate utilization in existing engines [32]. Furthermore, DME plays a crucial role in the production of various chemical compounds such as olefins, ethylidene diacetate, alkyl-aromatics, dimethyl sulfate, acetic acid, methyl acetate, gasoline, and other hydrocarbons, emphasizing its versatility and importance in the chemical industry [33–36].

Table 1. The physical and chemical properties of diesel, LPG, and DME for energy source applications [31]

Characteristic	Diesel	LPG		DME
		Butane	Propane	
Chemical formula	C_nH_{2n} or C_nH_{2n+2} (C_8 – C_{25})	C_4H_{10}	C_3H_8	CH_3OCH_3
Molecular weight	112 - 352	58.13	44.11	46.07
Cetane number	40 - 55	-	5	55 - 60
Stoichiometric A/F[a] ratio (kg/kg)	14.6	14.8	15.7	9.0
Liquid density (kg/m^3, 20 °C)	800 - 840	610	501	660
Vapor pressure (bar, 20 °C)	<0.01	8.4	2.1	5.1
Liquid viscosity (kg/ms, 25 °C)	2 - 4	0.2	0.2	0.12 – 0.15
Lower heating value (MJ/kg)	28.43	45.74	46.36	42.5

[a] A/F = air/fuel

The physical and chemical properties of DME make it a promising solution to addressing the challenges posed by climate change [37]. Additionally, DME can conveniently be converted to hydrogen (H_2) through a catalytic steam reforming process [38]. This is particularly valuable given the increasing demand for H_2 as a feed for fuel cells in electric vehicles and other applications. Using DME as a carrier becomes an appropriate method to ensure the safe transportation of hydrogen over long distances, as it mitigates the inherent risks associated with handling pure hydrogen [39,40]. This becomes even more significant when considering hydrogen production through water electrolysis or excess electricity from renewable sources like wind turbines, as CO/CO_2 conversion to DME offers environmental advantages [41,42].

2.2 DME production

DME production commonly involves the process of methanol dehydration, which is facilitated by employing a solid acid catalyst. This conversion process follows a series of steps, starting with

various resources and progressing through syngas, methanol synthesis, and ultimately DME production. Figure 2 shows this process visually from raw material to DME.

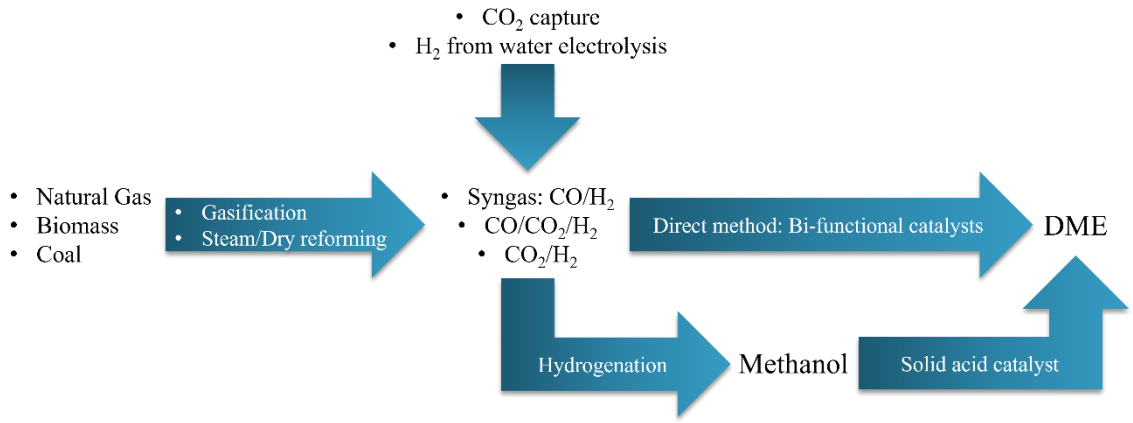

Figure 2. DME production from different feedstocks through direct and indirect methods [8]

The indirect approach (two-step) for DME production utilizes methanol as a starting material, whereas the direct method employs syngas [43]. Despite their differences, these routes share chemical similarities, with methanol serving as a crucial reaction intermediate in the two-step method. Consequently, the direct method can be viewed as process intensification where hydrogenation and methanol dehydration reactions are consolidated into a single step, eliminating the need for two separate steps, or chemical process units, as in the indirect approach. Specifically, it necessitates only one reactor instead of two reactors for two-step synthesis, resulting in reduced equipment and utility requirements. Furthermore, there is no purification step prior to the second reactor to eliminate unreacted CO_2 and syngas [44]. A study by Nakyai demonstrated that the equipment cost of the indirect route is 37% higher than that of direct production [44].

However, the indirect method can enhance production and economic efficiency through the recycling of unreacted feed. The separation between two established reactors can prevent negative effects associated with unreacted feed or unwanted species produced during hydrogenation. Additionally, in situations where syngas availability is limited, methanol can be obtained from alternative processes. As the indirect approach requires the use of two distinct catalysts, the catalysts employed are more affordable and easily separable. In contrast, the direct route necessitates higher technological expertise due to the particular optimal conditions required for the

first and second steps of DME production [45]. Consequently, comprehensive research into catalysts is essential for both methods.

Copper-based catalysts have traditionally been the primary catalysts for CO and CO_2 hydrogenation to methanol in the first step of the reaction sequence [46]. The syngas required for methanol production can be derived from different sources, including renewable resources such as biomass, as well as non-renewable sources like coal and natural gas. Biomass gasification, a thermochemical conversion method, offers a particularly promising approach to obtaining the necessary syngas for subsequent methanol synthesis. This gasification process can be accomplished through various techniques, including fixed bed, fluidized bed, entrained flow, and transport reactor gasifiers. By utilizing biomass gasification methods, the biomass conversion into syngas becomes feasible, paving the way for DME production [47–49].

After the syngas is produced, it must undergo a catalytic process based on the Eqs. 1-3 in order to convert into methanol. This process includes CO and CO_2 hydrogenation, and the water gas shift reaction (WGSR) [24]. The commonly used catalyst for this reaction is Cu/ZnO [50]. However, several challenges such as fast deactivation, low conversion, and low selectivity need to be addressed to enhance the overall efficiency of this process. One of the primary issues encountered is the agglomeration of Cu particles in the presence of water, leading to a decrease in the catalytic surface area available for CO/CO_2 hydrogenation [51,52].

$$CO + 2H_2 \rightarrow CH_3OH \quad \Delta H_{298} = -90.6\ kJ/mol \tag{1}$$

$$CO_2 + 3H_2 \rightarrow CH_3OH + H_2O \quad \Delta H_{298} = -49.5\ kJ/mol \tag{2}$$

$$H_2O + CO \rightarrow H_2 + CO_2 \quad \Delta H_{298} = -41.2\ kJ/mol \tag{3}$$

Various methods have been proposed and investigated to improve the stability and activity of the Cu/ZnO catalyst. For instance, one approach involves modifying Cu/ZnO with Ga to increase the Zn^0 content, which has shown promising results in enhancing catalytic performance [53]. Another strategy involves using TiO_2 as a support material and incorporating 1 wt% MgO to adjust the interaction between CuO and TiO_2, thereby improving dispersion and increasing the copper surface area [54]. Furthermore, supporting Cu/ZnO on γ-Al_2O_3 and incorporating additives such as ZnO, ZrO_2, and MgO have been explored to enhance dispersion and Cu^0 surface area, ultimately leading to improved catalytic properties [55]. Additionally, innovative methods like coating Cu nanoparticles modified by La into Cu phyllosilicate nanotubes have been proposed as a means of

enhancing catalytic performance [56]. Other modifications, such as incorporating Ce, Y, and WO_3, as well as tuning the distance between Cu particles supported on silica, have also shown potential in optimizing the catalytic activity [57–59].

In addition to Cu/ZnO, alternative catalysts have been investigated for CO/CO_2 hydrogenation. Cu/MgO [60], 0.5-1% Pd-modified CuO–ZnO–ZrO_2 [61], and CuCoAl/ZnO/ZrO_2 [62] have demonstrated their efficacy in facilitating this reaction. These catalysts offer potential advantages in terms of improved conversion rates and selectivity, presenting alternative options for methanol synthesis from syngas.

In the final step, a solid acid catalyst is required to obtain DME through Eq. 4. Traditionally, γ-Al_2O_3 is widely recognized catalysts known for this reaction in industrial scale. However, the low activity of this catalysts, which will be explained with detail in the next chapter, forced scientists to use other catalysts such as MFI (ZSM-5) zeolite for methanol dehydration. As a catalyst for industrial scale production, the conversion, selectivity, and stability are the critical factors to analyze a catalyst. Higher conversion and selectivity can reduce the cost of separation process which require different equipment. Also, the higher stability decreases the cost of shutting down the reactor for replacing the deactivated reactor.

$$2CH_3OH \rightarrow CH_3OCH_3 + H_2O \quad \Delta H_{298} = -23.4\, kJ/mol \tag{4}$$

In the past, industries exclusively employed the indirect route to produce DME. However, recent studies have revealed the potential benefits of direct methods, offering advantages in mitigating thermodynamic limitations and reducing investment costs [43]. However, both approaches rely on the same reactions (equations 1 - 4) and require distinct catalysts for methanol synthesis and dehydration. Hence, it is imperative to conduct thorough investigations into solid acid catalysts for utilization in both cases. Further, the widespread use of indirect methods by most industries underscores the importance of exploring solid acid catalysts.

2.3 Catalysts for methanol dehydration

To enhance methanol dehydration to DME, researchers have explored a range of catalysts. These include various types of zeolites such as MFI (ZSM-5), Linde W, Y, mordenite, ferrierite, beta, RHO, and KFI [63–65], as well as Pd/Cab-O-Sil (fumed silica) [66], AlPO (aluminophosphate)

and SAPO (silico-aluminophosphate) [67], heteropoly acids over TiO_2, BN (Boron Nitride), SiO_2, and ZrO_2 [68–71], modified-alumina with silica and phosphorus, and Al_2O_3–B_2O_3 [65]. As a result of their Lewis and Bronsted acid sites, these solid acid catalysts have the capability to convert methanol to DME. While Bronsted acid sites encompass weak, strong, and super acids, Lewis acid sites generally exhibit higher acidity than Bronsted acid sites in methanol dehydration reactions [72]. Bronsted acid sites, however, have been suggested to play an essential role in DME synthesis, as Lewis acid sites are more susceptible to water and product poisoning due to the strong adsorption of these compounds over the Lewis type [73].

Several critical factors, including acidity strength, hydrophobicity, and porosity, influence the activity of the catalyst, the spectrum of reaction products, and stability [23]. Each catalyst proposed for methanol dehydration has its advantages and drawbacks. The hydrophilic properties of Al_2O_3 cause deactivation of the catalytic role, for instance. It also requires high temperatures for catalytic activity due to its low acid strength. On the other hand, MFI zeolite was extensively studied and exhibited considerable potential for this reaction, possesses high acidity and lower hydrophilicity, enabling it to be active at lower temperatures and more tolerant to water exposure. However, its high acidity contributes to by-product formation, leading to coke deposition on active sites and subsequent catalyst deactivation [74].

In addition, HPAs possess strong Bronsted acidity which are beneficial to obtain high DME production yield. However, they have the serious limitation of a low surface area ($<1\ m^2.g^{-1}$) [75] . Therefore, investigating and evaluating various catalyst properties such as surface area, porosity, and acidity is crucial for optimizing catalyst performance in this process. These characteristics and the resulting catalyst performance in previous studies will be described and compared in detail in the following paragraphs.

The conversion of methanol to DME has been the subject of numerous studies, but several challenges persist. The major challenges in methanol dehydration include competitive water adsorption, by-product formation, and coke deposition [76]. Developing catalysts with less hydrophilic properties is crucial to mitigate the adverse effect of water produced in three reactions. By-products of methanol dehydration are typically olefinic/paraffinic C2–C4 hydrocarbons, which result in the formation of coke [77]. Methane and formaldehyde have also been observed as by-products in DME production reactions and Lewis acid sites showed a major role in promoting

methane production [78]. The performance of catalysts employed in this process should be assessed based on three criteria: 1) methanol conversion rate, 2) DME selectivity degree, and 3) catalyst stability (at high temperatures, resistance to coke deposition, and catalyst poisons). In addition to the nature of catalysts and their structural properties, operational conditions such as feed content, space velocity of flow, pressure, temperature, and reactor type can significantly impact the process. Therefore, the influence of these parameters on each catalyst will be explained while the effect of preparation methods, promoters, and post-treatment methods on three types of catalysts will be covered.

2.3.1 Alumina as a methanol dehydration catalyst

Aluminum oxide, or alumina (Al_2O_3), has gained widespread recognition and application as a catalyst for methanol dehydration for many years. Its efficacy stems from its ability to adopt various crystal structures, influenced by the pH during alumina hydrate precipitation and the calcination temperature. Alumina presents several crystal structures, including γ-, δ-, θ-, α-, and η-Al_2O_3. However, in methanol dehydration reactions, the γ- and η-Al_2O_3 structures are commonly preferred due to their elevated surface area and acidity.

Depending on the pH conditions, different hydrates are formed, leading to the precipitation of bayerite or boehmite, which are subsequently subjected to calcination. Increasing the calcination temperature for boehmite results in the formation of distinct phases in the following sequence: γ-Al_2O_3 < δ-Al_2O_3 < θ-Al_2O_3 < α-Al_2O_3 [79]. In contrast, bayerite follows this sequence with an increased calcination temperature: η-Al_2O_3 < θ-Al_2O_3 < α-Al_2O_3. These diverse crystal structures of alumina exhibit varying morphologies, crystallite sizes, and other physical and chemical properties. Among these crystalline phases, γ-Al_2O_3 has garnered significant attention as a catalyst for DME production due to its ability to minimize by-product formation [80].

The γ-Al_2O_3, the predominant phase of alumina, exhibits favorable characteristics as a support or active part of catalysts, including excellent catalytic activity and thermal stability. However, the presence of water generated during DME formation adversely affects γ-Al_2O_3 performance because of its highly hydrophilic nature. This leads to water adsorption and reduces the available surface area for methanol molecules, hindering the catalytic process. The study of activation energy demonstrated water's inhibitory effects on the alumina catalyst. Akarmazyan et al. reported

activation energy of 154.8 and 113 kJ/mol when using feed with 10% and 0% water, respectively [81]. Also, a 55 kJ/mol increase in activation energy was observed when Xu added 15% water to the feed gas, showing water's negative effect on γ-Al_2O_3 performance [82]. The negative effect of water on alumina activity for methanol dehydration is shown in Figure 3 from literature [81].

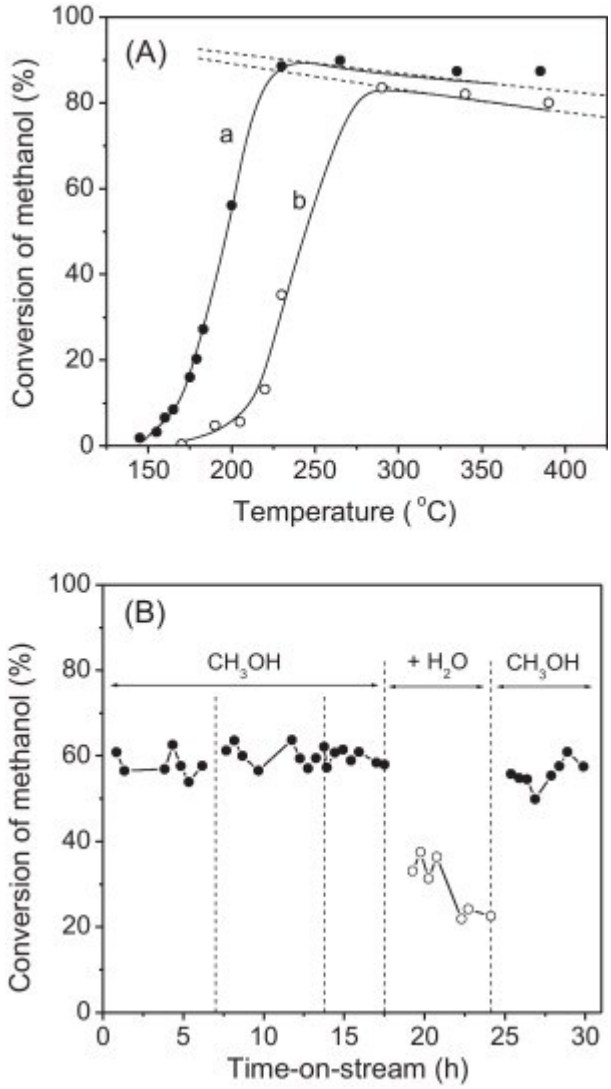

Figure 3. (A) Methanol Conversion vs. temperature over γ-Al_2O_3 catalyst: (a) without H_2O and (b) With 10% H_2O in the feed. (B) Impact of 10% H_2O addition in the feed on methanol conversion at T = 215 °C [81].

To address this issue, extensive research has been conducted to explore various preparation methods, promoters, and precursors. One proposed solution is the addition of silver to γ-Al_2O_3, which has been shown to mitigate water inhibition [83]. Yaripour et al. focused on optimizing DME yield by studying synthesis parameters such as precipitation/aging time, mixing rate, pH,

and precipitation/aging temperature using design of experiments (DOE) methodologies [84]. The results suggest that optimal catalyst synthesis involves a two-hour aging period, a mixing rate of 600 rpm, and a pH of 7.5 with precipitation at 50 ℃, which obtained 74.84 % methanol conversion at 300 ℃, 16 atm, and LHSV=15.6 mL/(h.g_{cat}).

In another study, Hosseini et al. employed four precipitants including sodium carbonate, sodium bicarbonate, ammonium carbonate, and ammonium bicarbonate to prepare nanosized γ-Al_2O_3 catalysts [85]. It was observed that using $(NH_4)_2CO_3$ as a precipitating agent resulted in the highest DME yield. Although 100% DME selectivity was maintained within a temperature range of 250 – 375 ℃, methane production increased at higher temperatures. Additionally, 375 ℃ was needed to achieve equilibrium conversion, resulting in high energy consumption and by-products. Yaripour et al also suggested that the formation of HCO_3^- and CO_3^{2-} in the structure leads to extra porosity and improved performance during calcination.

Since alumina possesses weak Lewis acid sites, high temperatures (> 300 ℃) are necessary to achieve significant conversion rates. On the other hand, high temperatures also promote the formation of undesirable by-products such as CO_2, CO, formic acid, and methane, which lead to catalyst deactivation due to the formation of coke on catalyst active sites [86]. To improve catalytic activity, researchers have investigated the employing of transition metals (e.g., Ni, Cu, Fe) as a promoter with γ-Al_2O_3. For instance, Armenta et al prepared the CuO-Fe_2O_3/γ-Al_2O_3 catalyst by impregnation method which increased the methanol conversion from 60% (using γ-Al_2O_3) to 70% at 290 ℃ [86]. These promoters enhanced the acidity around two times (16 → 34 μmol/g).

Other substances, including niobium, silica, phosphorous, titania, diboron trioxide (B_2O_3), and hematite, have been utilized to improve γ-Al_2O_3 catalytic performance. Promoters can be beneficial to improve the thermal stability of alumina catalysts since satisfying methanol conversion requires high temperatures and the catalysts should resist this condition for a long time. For example, the addition of TiO_2 has demonstrated an effective impact on γ-Al_2O_3 [82]. An optimal presence of 3-5% TiO_2 in the γ-Al_2O_3 structure has been observed to benefit the process with high conversion and selectivity [87,88]. The investigation of adsorption and conversion processes using diffuse reflectance infrared Fourier transform spectroscopy (DRIFTS) has revealed that Ti promotes the formation of higher acidic hydroxyl groups on the surface, thereby

enhancing methanol adsorption and conversion. Furthermore, incorporating silica into the γ-Al_2O_3 structure prevents alumina crystallite aggregation and reduces particle size [84].

In addition to γ-Al_2O_3, η-Al_2O_3 has also been investigated for methanol dehydration. Osman et al. conducted a study on a silver-promoted η-Al_2O_3 catalyst in the temperature range of 180-300 ℃ [89]. Only 18% conversion at 250 ℃ revealed that η-Al_2O_3 similar to the γ phase needed high temperatures (>300 ℃) to exhibit meaningful activity in the methanol dehydration process. However, by incorporating silver into η-Al_2O_3, the number of Lewis acidic sites increased, leading to greater catalytic activity at lower temperatures. The catalyst with 10 wt% Ag converted 39.5 % and 84.5% of methanol at 250 and 300 ℃, respectively, which grew 8-22 % compared to unmodified Al_2O_3. It should be noted that higher silver loadings had a negative impact on performance, which was attributed to the creation of giant clusters of Ag. Surface hydrophobicity is characterized by the water contact angle (CA, θ), where hydrophilic surfaces have $\theta < 10°$, hydrophobic surfaces have $90° < \theta < 150°$, and superhydrophobic surfaces have $\theta > 150°$ [90]. In the study of Ag-promoted η-Al_2O_3, the contact angle increased with increasing silver loading, measuring 1.69°, 20.7°, 50.7°, and 39° for pure η-Al_2O_3, 1%, 10%, and 15 wt% Ag, respectively [89]. The maximum yield was observed with 10% Ag, exhibiting the highest hydrophobicity. During methanol dehydration, surface hydrophobicity plays a crucial role in mitigating inhibition caused by water, which results in better performance at higher contact angles.

Furthermore, apart from γ-Al_2O_3 and η-Al_2O_3, γ-χ-Al_2O_3 can also be employed as a catalyst in this application. Achieving reasonable activity with γ-χ-Al_2O_3 requires high temperatures (>300 ℃) to attain approximately 80% conversion, prompting investigations into the use of promoters. Impregnation of CuO and Fe_3O_4 increases catalytic activity at moderate temperatures by altering pore diameter, volume, and surface area. For instance, Fe_3O_4/γ-χ-Al_2O_3 presented methanol conversions of 56% and 67% at 250 ℃ and 260 ℃, respectively [91].

In summary, γ-Al_2O_3 and η-Al_2O_3 have demonstrated superior methanol conversion to other alumina phases, as depicted in Figure 4 [92]. However, the competitive adsorption of water at reaction sites and the high-temperature requirement for catalytic activity continue to present challenges for alumina catalysts.

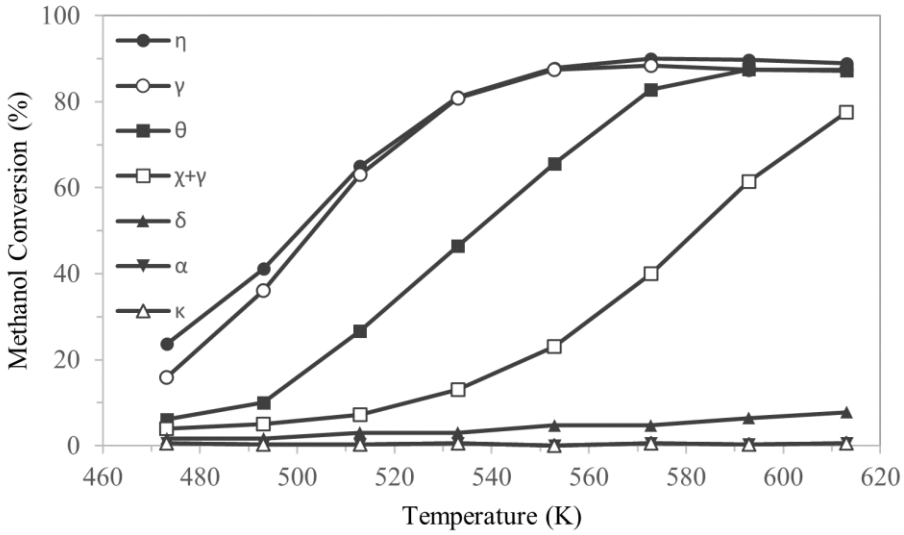

Figure 4. The activity of different phases of alumina including η-Al_2O_3 (●), γ- Al_2O_3 (○), θ- Al_2O_3 (■), (χ + γ)- Al_2O_3 (□), δ- Al_2O_3 (▲), κ- Al_2O_3 (△) and α- Al_2O_3 (▼) for methanol dehydration [92].

2.3.2 Heteropoly Acids as methanol dehydration catalysts

Heteropoly acids (HPAs), owing to their economic and environmental advantages, non-toxicity, reusability, and thermal stability have triggered tremendous research interest in catalysis applications in the past decades [93]. Also, because of their high acidity, they are another type of material explored for methanol to DME conversion. However, their low surface area has limited their application in various catalytic processes [94]. Keggin ions with a general formula of $[X^{n+}M_{12}O_{40}]^{(8-n)-}$ and Dawson ions with a general composition of $(X^{n+})_2M_{18}O_{62}^{(16-2n)-}$, discovered in 1934 and 1953, respectively, are two types of HPAs ions. Keggin-type HPAs with the general mentioned composition where X can be usually P or Si, with M being a transition metal such as Mo^{6+} or W^{6+} and have strong Bronsted acid sites, have been assessed for DME synthesis during recent years [95].

To address the challenge of low surface area, coating HPAs on suitable supports has been explored. The incorporation of supports, such as TiO_2, SiO_2, ZrO_2, and CeO_2, with HPAs, assists them in providing more appropriate catalytic activity for methanol to the DME process. For example, Peinado et al. studied these materials as support for tungstosilicic acid (HSiW) which is a type of HPA [71]. Figure 5 shows that HSiW supported on these materials exhibited higher rates of process

yield compared to using γ-Al_2O_3, primarily in response to the presence of Bronsted acid sites in the HSiW structure. The presence of Bronsted acid in HSiW was confirmed through H-NMR, NH3 adsorption isotherms, and NH_3-adsorbed DRIFTS experiments [70]. Among the studied supports, HSiW dispersed on TiO_2 and ZrO_2 demonstrated the highest activity, with DME formation rates of 50 mmol DME.h^{-1}.g_{HSiW}^{-1} at 180 °C.

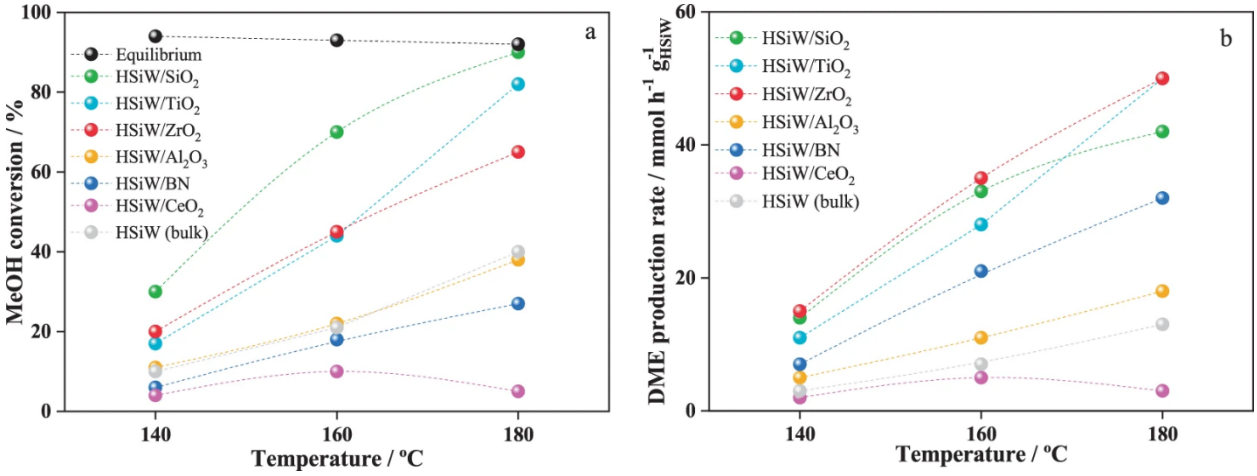

Figure 5. The a) methanol conversion (%) and b) DME production rate (mmol.h-1.gHSiW-1) using supported HSiW over SiO2, TiO_2, ZrO_2, Al_2O_3, BN, CeO_2 [71]

However, a rate of more than 200 mmol DME.h^{-1}.g_{cat}^{-1} can be achieved over FER zeolite which will be described in the next section [96]. This lower DME formation rate indicates that these materials may be less suitable for large-scale production. Despite the high thermal stability of HPAs, the catalytic activity rapidly decreased at temperatures above 200 °C for the methanol dehydration process. This decline in performance is attributed to the strong interaction between HSiW and the support, which limits proton mobility, as evidenced by reduced 1H-NMR peaks. The strong interaction also hinders methanol molecules' access to active sites.

However, optimizing the HPA loading can address this issue [70]. In another study, Ladera et al used DRIFT spectroscopy experiments and showed that employing a TiO_2 support with an appropriate amount of HPA can weaken the interaction between available protons and water, facilitating methanol adsorption on active sites [69]. However, HPAs, even when supported, typically have a surface area that does not exceed 250 $m^2.g^{-1}$ [97], and coke formation can cover active sites, leading to rapid deactivation during dehydration [95]. Notably, the decline in catalytic activity at higher temperatures and low pressure can be attributed to the absence of pseudo-liquid catalysis, which is crucial for the high performance of HPAs in methanol dehydration. Pseudo-

liquid catalysis resembles a gas-liquid system, where methanol is absorbed into the interpolyanion space between Keggin units.

Lower temperatures favor pseudo-liquid catalysis, as elevated temperatures generally reduce gas solubility in liquids [71]. XRD data revealed that when the reaction temperature exceeded 200 ℃, HSiW lost crystallization water and formed fully dehydrated phases, inhibiting the formation of the secondary structure necessary for pseudo-liquid catalysis, resulting in decreased catalytic activity. Josefine et al. studied Boron Nitride (BN) as an alternative to the typical mentioned support for HPAs [68]. They indicated $H_3PW_{12}O_{40}$ loading around 16 % on BN increased the activity 2 and 10 times compared to bulk sample and TiO_2-supported $H_3PW_{12}O_{40}$, respectively. Alharbi et al. conducted another study to investigate bulk $H_3PW_{12}O_{40}$ (HPW) (with and without Cs), and $H_4SiW_{12}O_{40}$ (HSiW) and compared the activity against MFI. Based on the correlation between acid strength and turnover reaction rate, they concluded that Bronsted acid plays an imperative role in methanol dehydration [95]. The characterization analysis indicated that the interaction between HPA and support resulted in decreasing acid strength in the order: HPW > HSiW > $Cs_{2.5}H_{0.5}PW$ ≈ $Cs_{2.25}H_{0.75}PW$ > HPW/SiO_2 ≈ $HSiW/SiO_2$ > HPW/TiO_2 > HPW/Nb_2O_5 > HPW/ZrO_2. Among the prepared catalysts, the best activity was observed over the 20% HSiW/SiO2 catalyst with 89% conversion (equilibrium) and 100 % DME selectivity at 150 ℃ which is shown in Figure 6. Also, the methanol conversion stability and DME selectivity were depicted in Figure 7 which shows the catalyst was stable for 4 h under low WHSV values. These results present that methanol conversion over supported/unsupported HPAs is not an appropriate option for large scale. At temperatures above 200 ℃, other hydrocarbons were detected and deactivation took place by coke production.

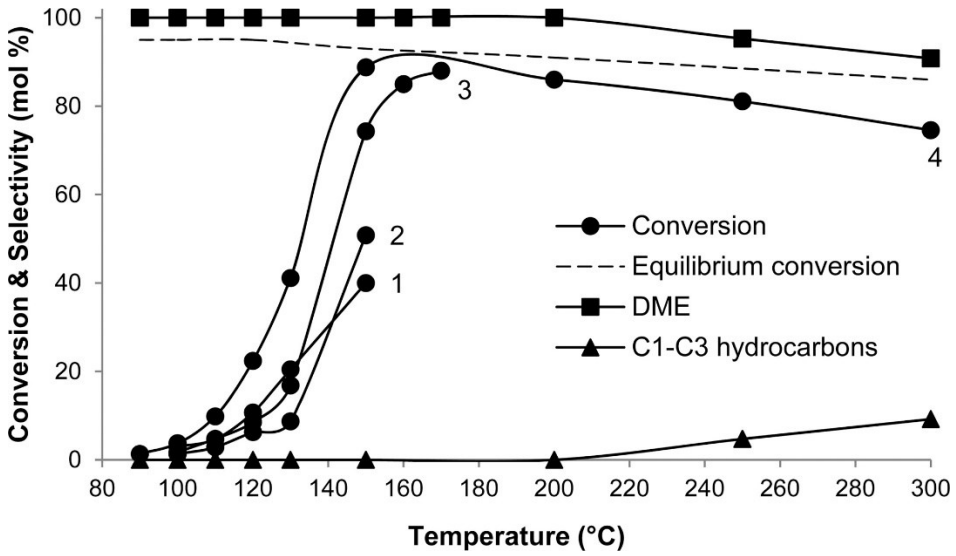

Figure 6. Methanol conversion at different temperatures over HPW (1), HSiW (2), and $Cs_{2.5}H_{0.5}PW$ (3) bulk catalysts, and the 20%HSiW/SiO_2 supported catalyst (4) under WHSV of 0.25 $g.g^{-1}.h^{-1}$ [95]

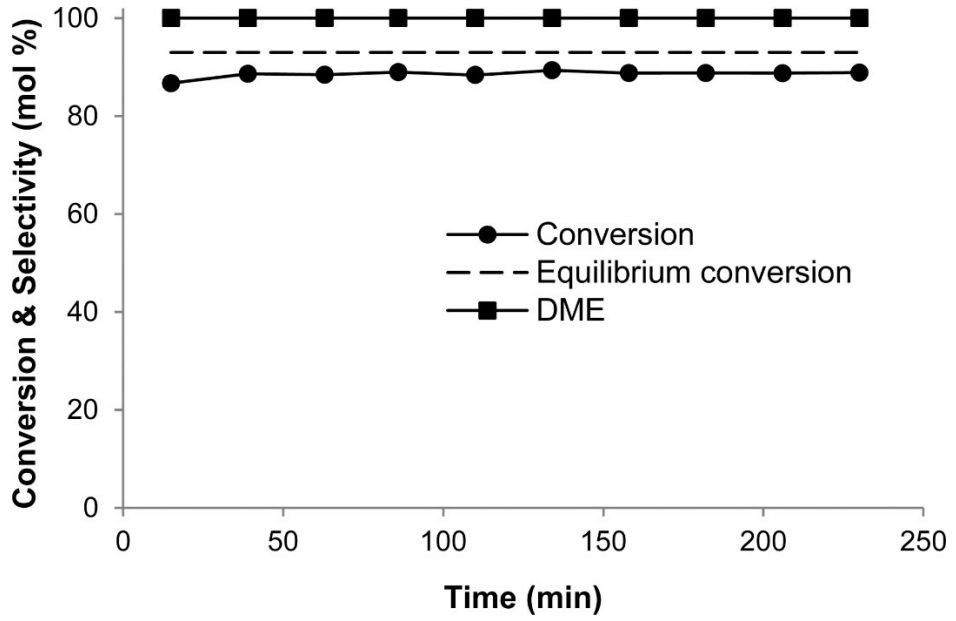

Figure 7. Methanol conversion and DME selectivity using 20%HSiW/SiO2 catalyst at 150 °C [95]

2.4 Zeolites properties and synthesis

2.4.1 Introduction to zeolite properties and synthesis

Zeolites are very versatile in terms of catalytic properties, selective adsorption, and chemical stability, which has made them widely employed in a variety of applications such as the petroleum and chemical industries [98]. They play a crucial role in the upgrading of crude oil, particularly role as heterogeneous catalysts for fluid catalytic cracking in the production of gasoline. They are extensively used in petrochemical processes that involve shape-selective reactions. In addition, zeolites are also highly effective in the synthesis of valuable chemicals and the protection of the environment [99]. Zeolites are also cost-effective, hydrothermally stable, and environmentally friendly, making them excellent catalysts, adsorbents, detergents, and ion exchangers [100].

Molecularly, zeolites are aluminum-silicate materials with open frameworks and well-organized pores. Various zeolite framework types can be developed from interconnected TO_4 tetrahedra (where "T" represents tetrahedrally coordinated elements like Si, Al, or P) [101]. Currently, the International Zeolite Association recognizes 235 zeolite framework types, which each have three-letter codes [102]. These frameworks can be further broken down into rings of different sizes, corresponding to the zeolites' pore openings. Some typical zeolites are depicted in Figure 8.

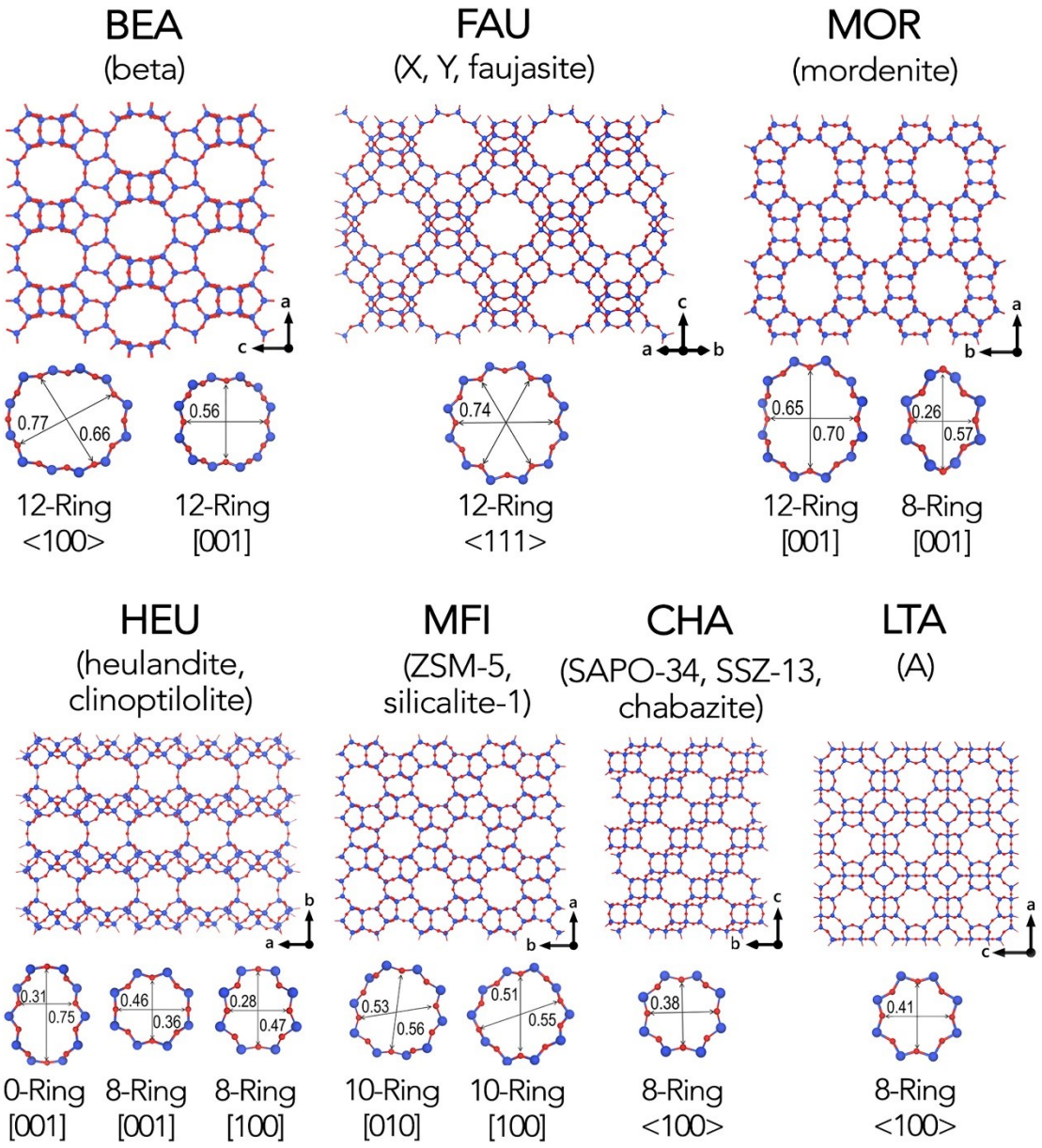

Figure 8. The framework structures and pore rings of frequently utilized zeolite types across diverse applications [102].

Zeolites can be categorized into different pore sizes based on the number of atoms forming the rings, either small (≤ 8 atoms), medium (10 atoms), large (12 atoms), and extra-large (>12 atoms) [103]. In zeolite frameworks, negative charges are typically balanced by extra-framework cations, which may be substituted with other cations. Additional species, such as water, can be eliminated from the pores of zeolite, allowing guest species to be adsorbed selectively according to their size, shape, and polarity. The shape-selective catalytic properties of zeolites can be attributed to their molecular sieving effect in combination with their spatial confinement of pores and catalytically active sites. Additionally, zeolites provide an excellent platform for stabilizing metal clusters and

nanoparticles, resulting in multifunctional compound materials with excellent physicochemical properties.

Zeolite synthesis takes place under hydrothermal conditions through the crystallization of a mixture including water, silica, alumina, and other elements [99]. In order to create the initial gels, basic agents, alkali cations, and organic compounds are combined with the mentioned mixture, and the process occurs under autogenous pressure (< 20 MPa) at high pH levels (> 11), and temperatures ranging from 60 to 200 ℃ [104]. The zeolite structure, crystallinity, and final properties can be affected by various parameters ranging from gel concentration to operational conditions.

The Si/Al ratio in the initial gel is a critical factor that modifies zeolite characteristics as well as the crystallization process kinetics [105]. Typically, this ratio decreases during the synthesis and the final product has a lower Si/Al ratio than the initial gel. Various sources of silica and alumina, including polymeric and monomeric reagents, can be used in the synthesis process. Sodium hydroxide (NaOH) or potassium hydroxide (KOH) are added to gels in order to improve the dissolving properties of precursors such as Si and Al [106]. Also, these agents enhance the Si-O-Si and Si-O-Al bonds creation. During the synthesis process, alkali cations (Na^+ and K^+) and their overall concentration play a vital role and need to be carefully controlled. Proper concentrations of alkali contribute to thermodynamically stable phases, and severe crystallization conditions, such as high temperatures and long crystallization times, can also influence phase stability. The stirring is crucial to zeolite crystallization to achieve a uniform structure, and different stirring methods will affect zeolite crystallization kinetics and size distribution. As a result of stirring, smaller crystals with narrower size distributions are formed, resulting in more favorable crystallization kinetics. Figure 9 shows methods to modify the chemical and textural properties of zeolites [99].

In zeolites, nucleation and crystallization are typically involved in the crystallization process. As the crystallization process advances, an amorphous solid phase known as hydrogel often forms initially. Several mechanisms have been proposed, including solution- and hydrogel-mediated mechanisms. Nucleation and crystal growth occur solely via soluble species in a solution-mediated mechanism, while the solid phase acts as a reservoir of nutrients. On the other hand, the hydrogel-mediated mechanism explains the zeolite crystallization by involving the restructuring of the amorphous solid phase which was formed in the initial stages. It is also possible to propose a

combination of solution-mediated and hydrogel-mediated mechanisms, whereby nucleation occurs within the hydrogel, while crystal growth proceeds via soluble species inclusion. Since there is such a wide range of gel compositions, zeolite structures, and synthesis conditions, it is difficult to establish a general model for zeolite crystallization [99].

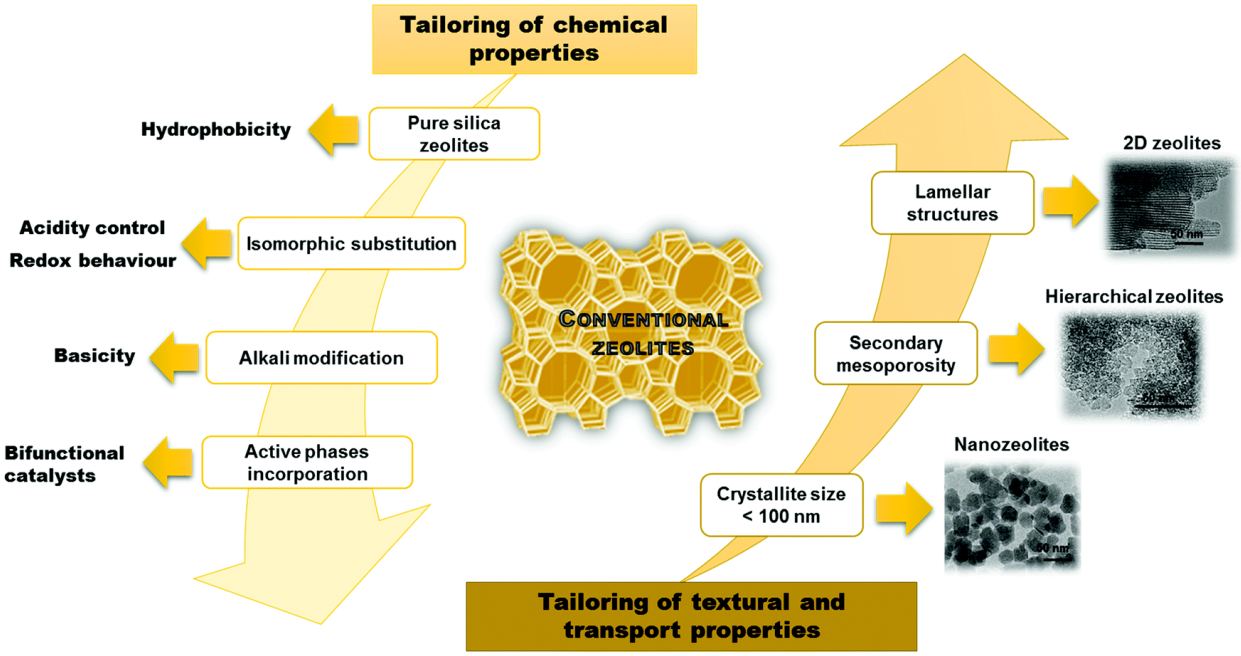

Figure 9. Common employed methods to reach a zeolite type with different chemical, textural, and transport properties [99].

Organic compounds have played a crucial role in the development of new zeolite structures, particularly ones with a high silica content [107]. In addition to modifying gel chemistry, these organic compounds can serve as pore-filling agents and templates. Zeolites have a highly specific chemical structure based on the organic templates used. Furthermore, seeding has been widely used in zeolite synthesis as a means of expediting the crystallization process by providing external nuclei, thereby reducing the induction period associated with nucleation [108]. In the template-free zeolite synthesis strategy, seeding is particularly effective, reducing reagent costs and eliminating the need for organic template removal through zeolite calcination. As well as enabling the solubilization of silicon and aluminum precursors, water plays a significant role in the chemistry of the initially formed gel. Too much water, however, can lead to undesirable effects, including less zeolite yield, aqueous waste streams, and high pressure [109]. To mitigate these issues, methods have been developed to minimize the water content during zeolite crystallization,

such as dry-gel conversion, vapor-phase transport, steam-assisted synthesis, and hydrothermal treatment of wetness-impregnated xerogels [99].

The presence of NaOH and KOH in the initial gel results in a zeolite with sodium or potassium as the cation (Na^+ or K^+). By ion exchanging the zeolite with ammonium salts, then calcining to remove ammonia, these forms can be converted to protonic forms (H^+), as shown in Figure 10. This method enables the preparation of acid-catalyzed zeolites that have a wide range of applications.

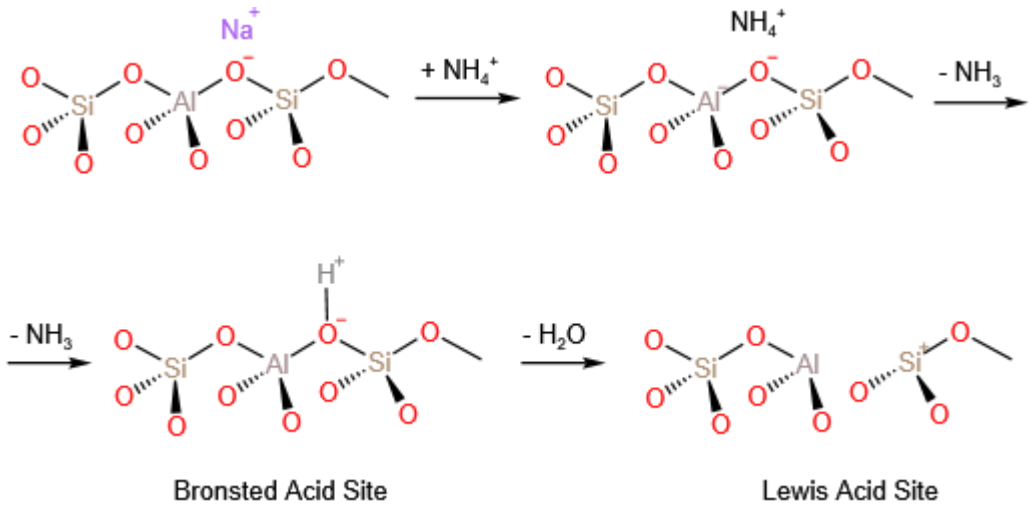

Figure 10. Bronsted and Lewis acid sites creation in a zeolite structure[110–113]

Zeolites are highly acidic due to their Bronsted acid types, which are linked to Al atoms in their framework. Zeolites may, however, possess Lewis acid type that result from dehydration process shown in Figure 10, or those that result from extra-framework aluminum species generated during synthesis or calcination. Bronsted and Lewis acid sites in zeolite structures are depicted in Figure 10 [110–113]. The ratio of Bronsted to Lewis acid sites usually increases with higher Si/Al ratios in the framework. A high silica zeolite will typically contain predominantly Bronsted acid sites, while a low silica zeolite will exhibit both Bronsted and Lewis acidity. Zeolites possess stronger and more uniform acid sites due to their crystalline nature compared to amorphous aluminosilicates [99]. To characterize zeolite acid sites, several theoretical and experimental methods have been used, including DRIFTs (diffuse reflectance infrared Fourier transform spectroscopy) and NH_3-TPD (temperature-programmed desorption).

2.4.2 Zeolites for Methanol Dehydration

Zeolites have attracted considerable attention in recent years as catalysts for methanol dehydration due to their unique properties. Extensive research has been conducted on various zeolite types to determine the most suitable catalysts, including mordenite (MOR), MFI (ZSM-5), ferrierite (FER), EU-1, ZSM-12, ZSM-22, SAPO-34, Beta (BEA), Y, RHO, and KFI. Based on their structure and dimensions, zeolites can be classified into 1-D, 2-D, and 3-D categories.

Among the examined zeolites, MOR, ZSM-22, EU-1, and ZSM-12 exhibit 1-D structures. Meanwhile, FER is characterized by a 2-dimensional structure, and MFI, Beta, KFI, RHO, and SAPO-34 possess 3-D structures [96]. The effectiveness and lifespan of these compounds depend on their dimensions, channel size (number of member rings), and the presence of side channels or cages, which affect coke rate deposition. While alumina catalysts did not suffer from losing active sites covered by heavy hydrocarbons, the strong acidity brought this problem to zeolite ones. Research suggests that 2-dimensional structures generally inhibit coke deposition due to their high surface area, accessibility to abundant active sites, and large channels, including a hierarchical porous structure [114,115].

A comparison between the zeolites reveals the quick deactivation of MOR and SAPO-34. MOR deactivates due to strong acid sites, while the deactivation of SAPO-34 can be attributed to large chabazite cages with narrow openings [116]. Although ZSM-12, ZSM-22, and EU-1 belong to the 1-D structure category and have similar acidity, they exhibit different deactivation rates. Their channel systems may explain this phenomenon. For instance, EU-1 zeolite with side pockets leads to higher hydrocarbon and coke accumulation, as shown by the channel system illustrated in Figure 11 [117]. Catizzone et al. have explained how cages and side pockets contribute to coke formation and loss of active area [96,118]. In a similar manner, Boronat et al. realized the presence of 8MR side pockets in MOR zeolite beside 12 MR channels favors hydrocarbon formation and catalyst deactivation [119].

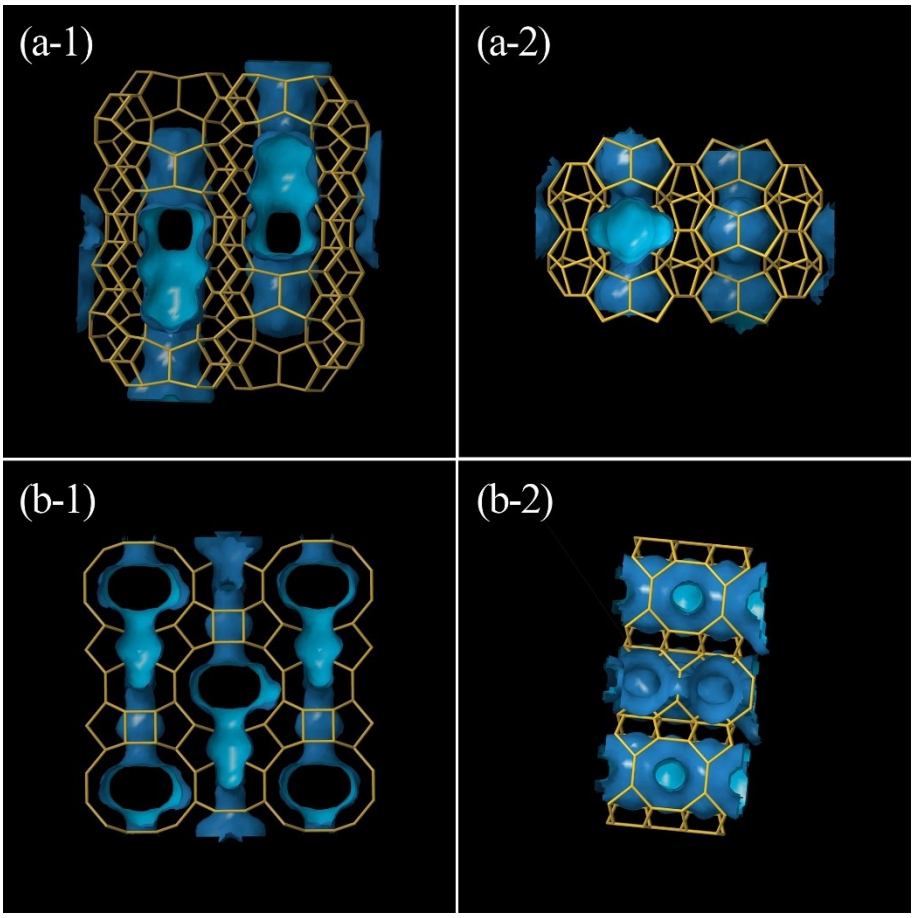

Figure 11. The channel structure of a) EU-1 and b)MOR 1-D zeolites [120]

In another study, partial deactivation was observed in the 3-dimensional large channel system of Beta, while FER-8 (Si/Al = 8) and MFI maintained relatively stable performance [112]. Quantifying the amount of coke deposited on zeolites with different structures after 60 h at 240 °C and WHSV = 4.5 h^{-1}, the following values were obtained: mordenite (72 $mg.g_{catalyst}$-1), ZSM-22 (31 $mg.g_{catalyst}^{-1}$), EU-1 (90 $mg.g_{catalyst}^{-1}$), ZSM-12 (72 $mg.g_{catalyst}^{-1}$), FER-8 (45 $mg.g_{catalyst}^{-1}$), MFI (60 $mg.g_{catalyst}^{-1}$), Beta (79 $mg.g_{catalyst}^{-1}$), and SAPO-34 (149 $mg.g_{catalyst}^{-1}$). It is evident that channel diameter, channel intersections, and side-pocket size significantly influence catalyst stability. Based on these results, FER zeolites' 2-D structure show promise to improve mass transfer and reduce coke deposition. Additionally, zeolites with uniform 3-D structures can provide highly active sites and stability. Besides the channel system of zeolites, several factors, including strength and type of acid sites, pores and crystal size, external or internal acid sites, and surface area, can affect the methanol conversion, DME selectivity, and coke formation rate.

Also, the pore structure of zeolites influences coke-type distribution, as different types of zeolites exhibit varying coke compositions. For example, MFI zeolites produce coke composed of tetra-methylbenzene (20%), penta-methylbenzene (30%), and hexa-methylbenzene (50%) [72]. FER zeolite yields mostly tetra-methylbenzene, while MOR zeolite, with its larger pores, produces mainly 1,4-ditertbutylbenzene [72]. Thus, controlling the pore structure can manage the deactivation mechanism caused by coking.

In addition to their high porosity, zeolites also have strong acid sites and a remarkable surface area which is listed in Table 2. While these features enable rapid methanol conversion, they also lead to the formation of undesirable byproducts. As explained earlier, these byproducts, called coke, can accumulate on both the external surface and within pores. It has been observed through characterization techniques that Bronsted acid sites account for the most zeolite acidity, which promotes coke deposition. Consequently, Lewis/Bronsted acid site ratio plays a crucial role in coke formation.

Table 2. The acidity and surface area of different catalysts used for methanol dehydration.

Catalyst	Si/Al	Total concentration of acid sites /µmol/g	Concentration of low temp. acid sites /µmol/g	Concentration of high temp. acid sites /µmol/g	Surface density of acid sites /µmol/m^2	BET (m^2/g)	Ref
Beta	21	529	-	-	0.809	654	[23]
Y	16	482	-	-	0.583	826	[23]
Al-SBA-15	-	229	-	-	0.475	482	[23]
Al-MCF	-	147	-	-	0.304	484	[23]
MFI	16.5	209	89	146	0.537	389	[23]
MFI/1h		256	86	144	0.642	399	[23]
MFI/2h		297	88	361	0.615	483	[23]
MFI/4h		316	138	241	0.591	535	[23]
MOR	7	1034	-	-	2.971	348	[72]
FER	7	813	-	-	2.903	280	[72]
MFI	34	439	-	-	1.137	386	[72]

RHO	3.5 (5)	2534	1173	1361	3.121	812	[121]
KFI	3.5 (5)	1655	841	814	4.332	382	[121]
M-FER	10	1087	-	-	3.274	332	[78]
NP-FER	10	1311	-	-	4.175	314	[78]
NC-FER	10	797	-	-	2.622	304	[78]
Nano-MFI	26	270	-	270	0.712	379	[122]
Meso-MFI	26	280	-	280	0.757	370	[122]
Con-MFI	26	250	80	170	0.718	348	[122]
Commercial MFI	23.3	1456	727	729	4.18	348	[121]
Commercial γ-Al_2O_3	-	346	74	272	3.09	112	[121]
MOR	25	714	186	528	2.051	348	[96]
ZSM-22	45	313	85	228	1.490	210	[96]
EU-1	30	431	181	250	1.122	384	[96]
ZSM-12	50	333	123	210	1.132	294	[96]
FER8	8	787	346	441	2.321	339	[96]
FER30	30	464	135	329	1.706	272	[96]
FER60	60	332	110	222	1.207	275	[96]
MFI	15	602	271	331	1.672	360	[96]
Beta	25	609	256	353	1.044	583	[96]
SAPO-34	0.4	1174	434	740	3.173	370	[96]
γ-Al_2O_3	-	283	74	209	1.422	199	[96]

Migliori conducted a comparative study of MOR, MFI, and FER zeolites to evaluate their stability under methanol dehydration [72]. The MOR zeolites with the highest acidity strength and L/B = 0.66 ratio indicated superior activity. However, this high acidity caused rapid coke formation and deactivation of the MOR zeolite which is depicted in Figure 12. It is noteworthy to mention that

MOR and FER catalysts achieve thermodynamic equilibrium at 220 ℃, while MFI catalysts reach thermodynamic equilibrium at 240 ℃. This result was in accordance with zeolites' acidity strength.

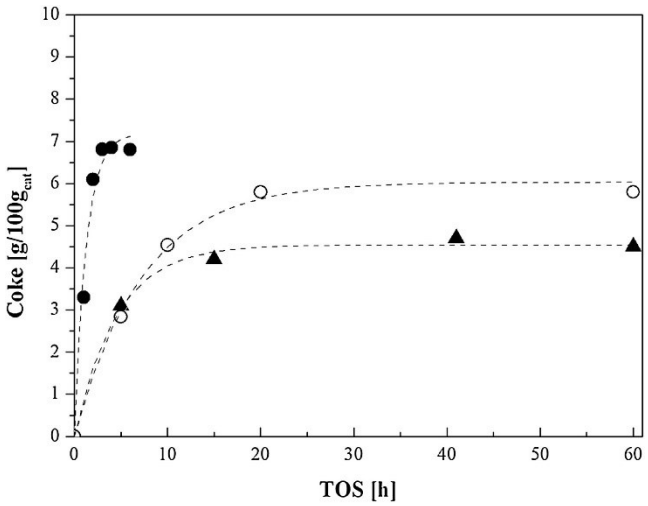

Figure 12. The amount of coke deposited over MOR (●), FER (○), and MFI (▲) under methanol dehydration reaction at 240 ℃ [72].

In another study, Rutkowska et al. employed zeolite Beta (Si/Al~21), Y (Si/Al~16), and mesoporous silicas (SBA-15 and MCF) to compare their performance to the H-MFI catalyst [23]. As shown in Figure 13, it can be seen that the highest methanol conversion can be achieved over Beta and Y zeolite, which is attributed to the highest acidity concentrations exhibited in Table 2. The catalytic activity of prepared samples was in the sequence of Beta > Y > MFI > Al-SBA-15 > Al-MCF, which generally corresponds to acidity strength. However, DME selectivity was reduced to lower values at temperatures above 250 ℃ in the case of zeolites Beta and Y while it was kept at 100% over other catalysts. Based on analysis of catalysts' structure and acidity, DME selectivity originates from a combination of acidity (higher acidity triggers by-product formation) and porosity (less microporosity). Mesoporous structure enhances diffusion limitations in the channel for reactants and products, which results in higher selectivity.

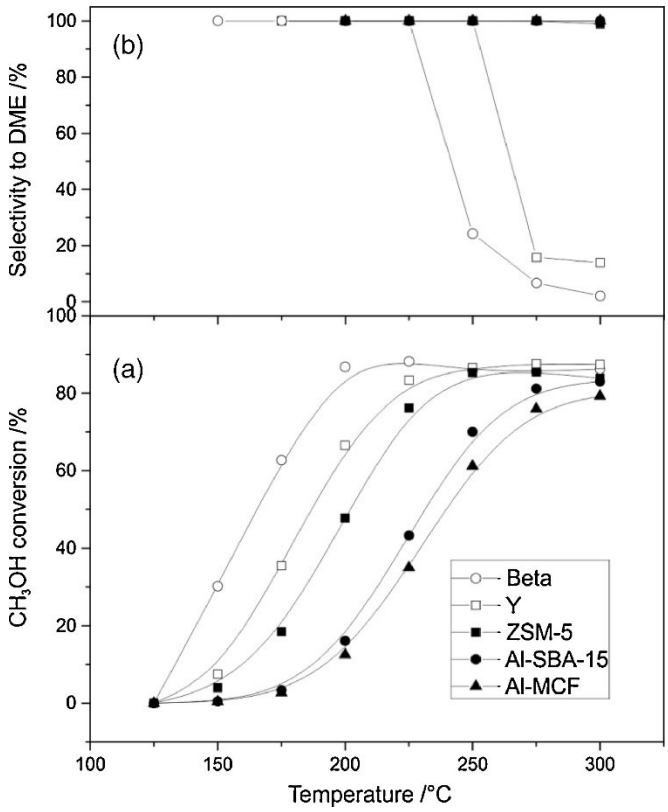

Figure 13. The activity of different catalysts in a) methanol conversion and b) DME selectivity at 125 – 300 °C under the flow of 20 ml/min containing 4% methanol (~ WHSV of 0.5) [23].

In a comprehensive project on various types of zeolites, activity at 220 °C was ranked as follows: MOR > FER-8 > Beta > SAPO-34 > MFI = FER-30 > EU-1 > FER-60 > ZSM-22 > γ-Al_2O_3 > ZSM-12 [107]. Methanol conversion followed the expected pattern based on acidity strength in Table 2. A confirmation of Migliori's results [72], MOR zeolite deactivated quickly, while FER-8 remained stable [96]. Masih et al. investigated two other zeolite types including RHO and KFI. They achieved equilibrium methanol conversion with 100 % DME selectivity at 200 °C over RHO zeolite [121]. However, the stability of this catalyst was reported for 25 h.

To improve catalytic activity, stability and reduce acid strength, various methods and additives have been employed to modify zeolites. The impact of particle size on the catalytic performance of zeolites has been investigated [123]. Nanosized (0.1 – 0.3 μm) and microsized (3 – 10 μm) FER and MFI catalysts were prepared. The results indicated that nanosized catalysts exhibited higher activity than microsized catalysts. This improvement was attributed to better control of residence time, enhanced diffusion rates, and increased efficiency of acid sites, despite microsized catalysts having a larger specific surface area and acidity. Additionally, the nanosized FER zeolite

demonstrated superior stability (99% DME selectivity after 20 h), higher methanol conversion, and lower activation energy (46 kJ/mol) compared to both MFI samples [123]. The smaller crystal size significantly improved accessibility to acid sites and diffusion rates.

In another investigation, three FER samples with different crystal sizes including 5-10 µm (M-FER), 300-500 nm (NP-FER), and 100 nm (NC-FER) were synthesized [78]. As shown in Figure 14, reducing the crystal size from micro to nanoscale resulted in higher methanol conversion due to enhanced accessibility to acid sites. Despite having a larger crystal size than NC-FER, NP-FER exhibited stronger acidity (1.308 $mmol.g^{-1}$) and achieved superior methanol conversion at 220. They also calculated the turnover frequency of 86 h^{-1} and 62 h^{-1} for NC-FER and NP-FER, respectively, which indicated improved mass transfer by reducing crystal size.

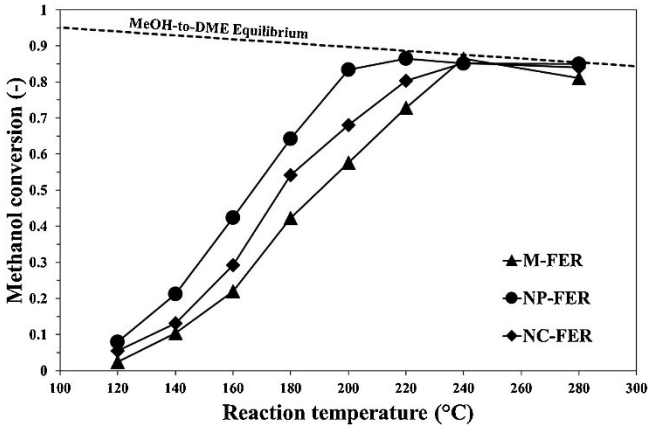

Figure 14. Methanol dehydration vs. temperature using FER zeolites with different crystal sizes (M-FER = 5-10 µm, NP-FER = 0.30-0.50 µm, and NC-FER = 0.10 µm) [78]

The effect of crystal size is not limited to FER-type zeolites. Rownaghi et. al investigated the DME production over nano, meso, con[1] MFI zeolites with 0.12, 0.30, and 1.20 µm crystal size to realize the relationship between methanol dehydration level, DME selectivity with the crystal size [122]. As shown in Figure 15, at the same experiment conditions at 225 °C, the nano-MFI delivered 19%, 15.7%, and 23% increase in methanol conversion, DME selectivity, and DME yield compared to the con-MFI zeolite. They also measured aluminum content in crystals (AC) and on the surface (AS) by ICP and XPS analyses, respectively, and showed that the AS/AC ratio is less in the case of nano-sized crystals. They also found a linear inverse correlation between DME selectivity and AS/AC ratios. FER and MFI zeolites showed different correlations between AS/AC ratios and

[1] "Con" represents the large crystal size in µm scale.

crystal size; however, external acidity was lower in nano-size in both cases, resulting in better activity.

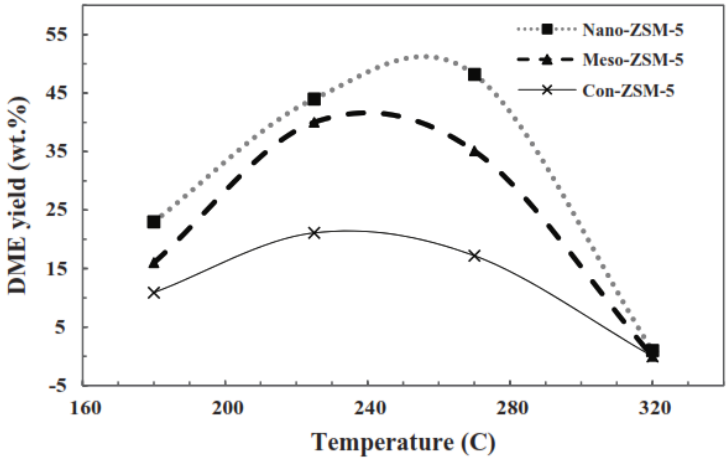

Figure 15. DME yield at 180 – 320 °C over three samples of ZSM-5 (MFI) zeolite with different crystal sizes (Con-ZSM-5 = 1.2 µm, Meso-ZSM-5 = 0.30 µm, and Nano-ZSM-5 = 0.12 µm) [122]

Zeolites with narrow channels create favorable conditions for coke formation, leading to pore blockage. However, the literature suggests that hierarchical mesoporosity can optimize the interaction time between reactants (or products) and active sites of the catalyst toward more stable catalysts [23,124,125]. Several methods have been studied to introduce mesoporosity into zeolites' structure, including soft and hard templating routes, steam leaching, acid leaching, and alkali treatment. Among these methods, the alkaline treatment also referred to as desilication, has demonstrated excellent efficiency to modify zeolites' structure [124]. Krim et al. employed a two-step treatment using NaOH and TPAOH which improved the external surface area, total acidity, and mesoporous volume, followed by methanol conversion [126]. The alkaline treatment of ZSM_5 zeolites was examined by Schmidt et al [125]. A solution composed of 0.5 M NaOH and 0.05 M N,N,N-trimethyl hexadecyl ammonium bromide (CTAB) was used for the process. The results showed that hierarchical structures prepared through desilication have the potential to exhibit increased activity and lifetime.

The duration of the alkaline treatment has been identified as a crucial factor influencing the structural modifications of MFI to improve its catalytic activity, as highlighted by Rutkowska et al. [23]. Modified zeolite was created by dissolving MFI in 0.1M NaOH solution and stirring at 80°C for different periods of time. The resulting samples were labeled MFI/1h, MFI /2h, and MFI /4h, corresponding to stirring times of 1, 2, and 4 h, respectively. Methanol dehydration was

enhanced with desilication treatment at temperatures below 250 °C, as shown in Figure 16. It was concluded that a one-hour treatment was insufficient to induce significant alterations in the zeolite structure. However, a four-hour stirring duration yielded substantial changes from a microporous to a mesoporous structure, as confirmed by XRD analysis. Consequently, a two-hour treatment resulted in the optimal development of porosity in MFI.

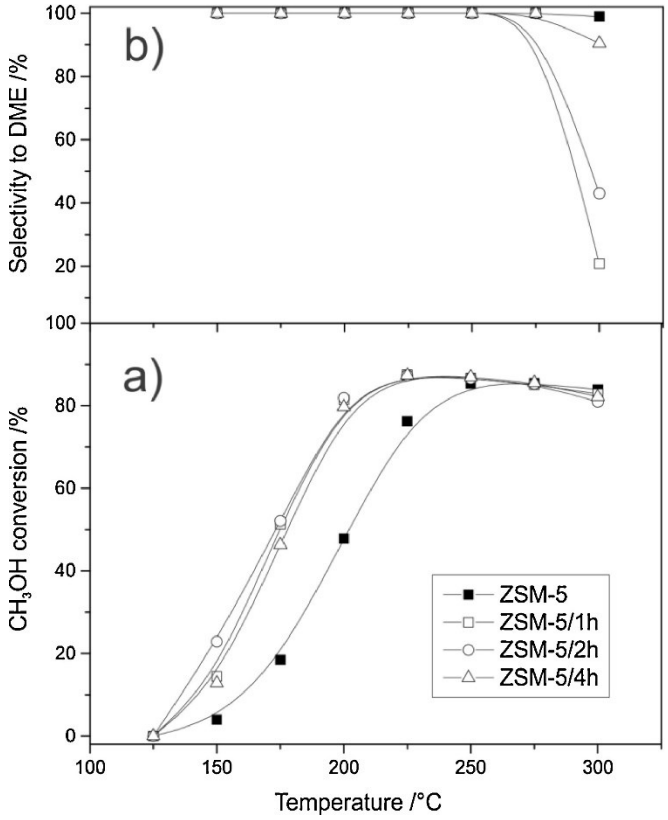

Figure 16. The influence of alkaline treatment with different duration (1, 2, and 4 h) on ZSM-5 (MFI) activity toward a) methanol conversion and b) DME selectivity [23]

Extensive characterization techniques such as Diffuse Reflectance Infrared Fourier Transform Spectroscopy (DRIFTS), NH_3-TPD, and N_2 adsorption/desorption tests have revealed the significant impact of the Si/Al ratio on zeolites' acid strength and properties [23]. Higher aluminum content or desilication leads to increased acidity. Sameh et al. synthesized HZSM-5 (MFI) zeolites with various Si/Al ratios ranging from 25 to 400 [127]. Their results indicated that a lower Si/Al ratio resulted in reduced crystallinity and increased surface area. Lowering the Si/Al ratio also boosted DME selectivity and methanol conversion, particularly at low temperatures. Similarly,

Migliori demonstrated that among Si/Al ratios ranging from 10 to 50, MFI zeolites with a Si/Al ratio of 10 exhibited the highest activity. This finding aligns with the observations made by Sabour for Al-HMS (hexagonal mesoporous silica) compounds, where a Si/Al ratio of 10 showed optimal activity for methanol dehydration in Si/Al ratios of 5 to 35 [128]. In another study conducted by Khandan et al., various zeolites including MFI, Y, MOR, FER, and Beta were assessed, supporting a reverse correlation between zeolites' Si/Al ratio and their activity [129].

Promoters are commonly introduced into the main catalyst to enhance performance and stability, particularly under high temperatures and in water. The acid strength of zeolites can be reduced by adding Zr, Zn, Mg, Na, or Al. This modification is typically achieved through an impregnation process. For instance, XRD, NH_3-TPD, and NH_3-FTIR analyses showed that modified H-MOR zeolites with these elements exhibited higher stability [129]. Notably, Al-H-MOR zeolites exhibited the highest activity compared to MFI, Y, FER, Beta, ZSM-12, ZSM-22, EU-1 zeolites, SiO_2, and γ-Al_2O_3 for liquid and gas methanol conversion. A further modification, however, is required to enhance long-term stability and selectivity towards DME. The incipient impregnation of magnesium oxide up to 5% into MFI zeolites increased DME selectivity from 49% to 64% while maintaining a methanol conversion of 96% [130]. As magnesium reacts with the bridging hydroxyls, $Mg(OH)^+$ species form, increasing Lewis acid sites and diminishing strong Bronsted acid sites.

In this section, we have explored various catalysts for the methanol dehydration reaction. The Al_2O_3 has demonstrated stable conversion over a prolonged period, but its high operating temperature makes it unsuitable for thermodynamically limited reactions in both direct and indirect DME production. Heteropoly acids (HPAs) exhibited activity at lower temperatures, even below 200°C, but they suffer from fast deactivation within a few hours and loss of activity at high temperatures, thereby limiting their use in large-scale production. In particular, hybrid catalysts (methanol synthesis and dehydration catalysts) should be employed for direct DME synthesis at temperatures of around 200 – 250 °C.

Zeolites, on the other hand, display different performance characteristics depending on their type and physicochemical features. However, the minimum temperature observed for zeolites was 200 °C for 25 h of stability or 220 °C for 60 h of stability. In this study, we specifically investigated two types of zeolites, RHO and KFI, for methanol dehydration. Several samples were synthesized

with varying preparation parameters, and their performance at different temperatures and long-term conversion will be discussed in the subsequent chapters.

CHAPTER 3: METHODOLOGY

3.1 Zeolite synthesis

As previously discussed, a comprehensive synthesis effort was undertaken to prepare a range of zeolite samples, comprising 5 KFI-type zeolites and 6 RHO-type zeolites, employing a hydrothermal crystallization method. In this preparation process, distinct precursors were employed, including precipitant agents such as NaOH for RHO-type zeolites and KOH for KFI-type zeolites. Additionally, cesium hydroxide was used for RHO-type zeolites, while strontium chloride was incorporated for KFI-type zeolites. These precursor materials were dissolved in deionized water to form a clear colourless solution. In cases with the structure directing agent or template, 18-crown-6 ($C_{12}H_{24}O_6$) was also added to the solution. In step the PTFE beaker containing the solution was put on a stir plate.

Once the clear colourless solution was obtained, the aluminum source was introduced into the solution. For KFI-type zeolites, aluminum hydroxide ($Al(OH)_3$) was utilized, while sodium aluminum oxide ($Al_2O_3 \cdot Na_2O$) was added for RHO-type zeolites. The mixture was stirred for a few minutes to ensure proper homogenization. Subsequently, the silicon source, colloidal silica (40%), was gradually added dropwise and stirred for a duration of 30 minutes for KFI zeolites and 24 h for RHO zeolites. The extended stirring period allowed the silica source to be fully mixed with the solution, initiating the nucleation process and promoting zeolite formation. As a result of this nucleation, a gel-like slurry was created.

The resulting gel was then transferred to a 45 ml Teflon-lined stainless-steel bomb reactor, as depicted in Figure 17. This specialized reactor facilitated the crystallization process under autogenous pressure conditions, ensuring optimal growth and structure development of zeolite crystals. The duration of the crystallization process varied for each sample, with specific details regarding the synthesis conditions outlined in the dedicated synthesis sections of the respective papers.

Figure 17. Teflon-lined stainless-steel bomb hydrothermal reactor

It is worth noting that the selection of different precursor materials, such as cesium hydroxide and strontium chloride, was employed to introduce specific cations into the zeolite framework, which can influence the catalytic properties and performance of the resulting zeolite samples. Furthermore, the hydrothermal crystallization method allowed for controlled and reproducible synthesis of KFI and RHO zeolites, enabling subsequent investigation and comparison of their respective performances in methanol dehydration. The gel composition and synthesis conditions including time and temperature for KFI and RHO preparation are listed in Table 3. For example, the 2.3 for K_2O and 10 for SiO_2 means the molar ratio of K_2O:SiO_2 is 2.3:10. The samples were labeled as KFI_XTY and RHO_XTY where X and Y represent the Al_2O_3:Template ratio and crystallization duration (days), respectively.

Table 3. The molar ratio of precursors in initial gel, hydrothermal synthesis temperature, and crystallization time for different samples

Sample	K_2O	Na_2O	$SrCl_2$	CsO	Al_2O_3	SiO_2	18-C-6	H_2O	Temperature (°C)	Time (days)
KFI_1T3	2.3	0	0.1	0	1	10	1	160	150	3
KFI_1T5	2.3	0	0.1	0	1	10	1	160	150	5
KFI_1T7	2.3	0	0.1	0	1	10	1	160	150	7
KFI_0.5T5	2.3	0	0.1	0	1	10	0.5	160	150	5

KFI_0T5	2.3	0	0.1	0	1	10	0	160	150	5
RHO_0.5T6	0	1.8	0	0.3	1	10	0.5	100	110	6
RHO_0.5T8	0	1.8	0	0.3	1	10	0.5	100	110	8
RHO_0.5T10	0	1.8	0	0.3	1	10	0.5	100	110	10
RHO_0.25T8	0	1.8	0	0.3	1	10	0.25	100	110	8
RHO_0T8	0	1.8	0	0.3	1	10	0	100	110	8
RHO_0T7	0	3.0	0	0.4	1	10.8	0	110	100	7

3.2 Methanol dehydration reactions

The methanol dehydration reaction was conducted in a laboratory-scale reactor, as illustrated in Figure 18. The reactor was equipped with mass flow controllers to precisely regulate the flow rate of argon (Ar) at 15.6 ml/min, ensuring a consistent gas environment during the experiment. To introduce liquid methanol into the reactor, a syringe pump was employed, allowing for controlled injection of methanol into the Ar stream at a rate of 0.5 ml/h, resulting in a gas feed mixture containing 30% methanol. The reaction testing was performed at ambient pressure.

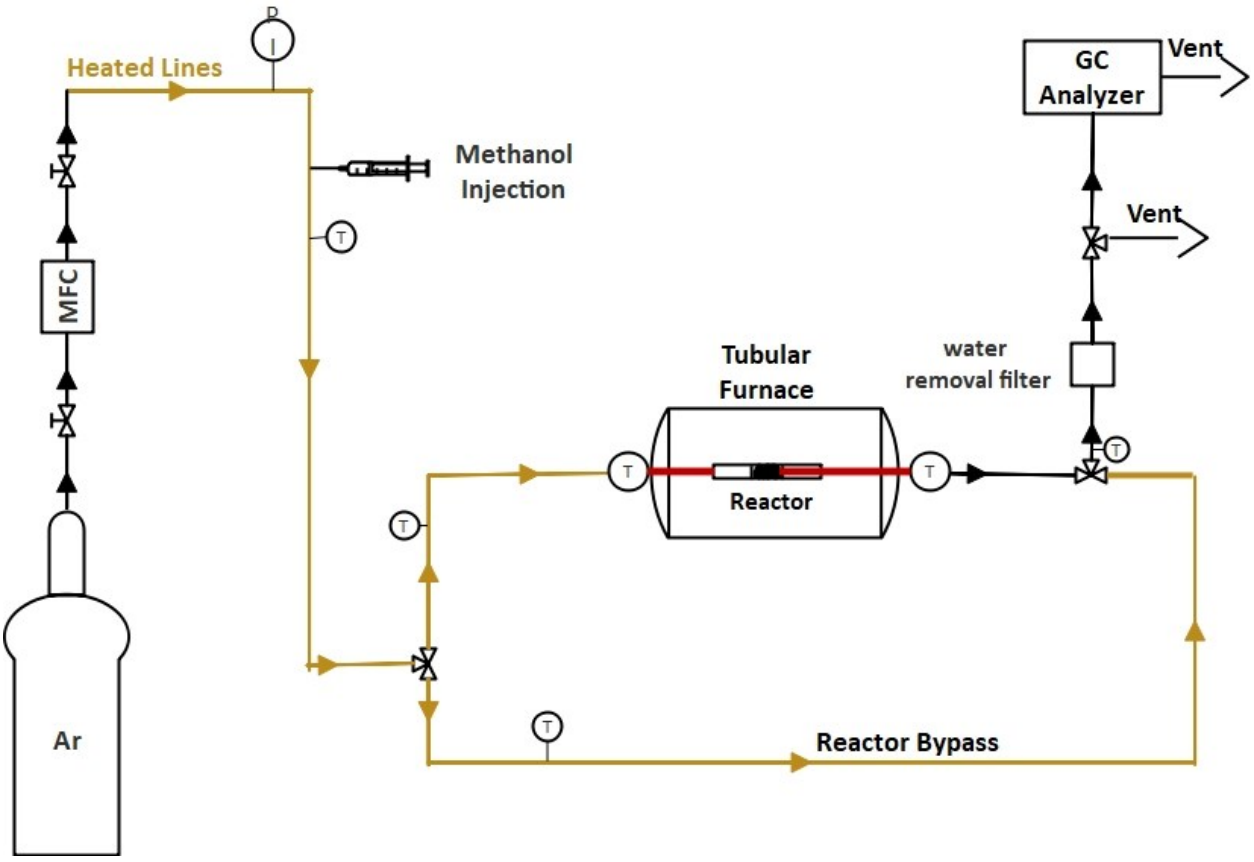

Figure 18. The schematic view of setup for DME production

To prevent methanol condensation within the experimental setup, the tubing connecting the mass flow controller to the tubular furnace was heated to 120°C, maintaining the gas-phase nature of the reactants throughout the system. On top of the catalyst bed, a K-type thermocouple was positioned to monitor the temperature during the reaction. This temperature measurement served as a crucial parameter for assessing the catalyst's reaction kinetics and performance.

After the reaction took place, the output gas from the reactor was analyzed using a Gas Chromatography (GC) apparatus equipped with a flame ionization detector (FID). The column used to separate analytes was HP plot Q with length of 30 m and diameter of 0.32 mm The GC analysis enabled the determination of the concentration of different components in the gas phase, providing valuable insights into the reaction products and byproducts.

To evaluate the performance of the catalyst, the conversion and selectivity were calculated using equations 5 and 6, respectively, where C_i indicates the concentration of *i* species. These equations

allowed for quantifying the extent of methanol conversion and the selectivity towards desired products, providing essential metrics for assessing the catalyst's efficiency and effectiveness in the methanol dehydration process.

$$Methanol\ Conversion\ (\%) = \frac{C_{CH4}+(2C_{C2H6O})+(2C_{C2H4})+(2C_{C2H6})+(3C_{C3H6})+(3C_{C3H8})+\cdots}{C_{CH3OH}+C_{CH4}+(2C_{C2H6O})+(2C_{C2H4})+(2C_{C2H6})+(3C_{C3H6})+(3C_{C3H8})+\cdots} \quad (5)$$

$$DME\ Selectivity\ (\%) = \frac{2C_{C2H6O}}{C_{CH4}+(2C_{C2H6O})+(2C_{C2H4})+(2C_{C2H6})+(3C_{C3H6})+(3C_{C3H8})+\cdots} \quad (6)$$

3.3 Catalyst characterization

3.3.1 XRD

X-ray diffraction (XRD) is a widely employed technique that provides valuable insights into the atomic and crystalline structures of materials. Researchers can analyze X-ray scattering patterns to determine the position of atoms, their arrangement within the unit cell, and the spacing between atomic planes by using XRD on a crystalline sample [131]. Various materials can be subjected to this technique, including ceramics, semiconductors, minerals, polymers, metals, and polymers. XRD has the advantage of being non-destructive, which means researchers can examine solid and powder samples without compromising their integrity. Similar to fingerprints, each crystallized sample has its own XRD pattern that can be used to identify the sample through XRD analysis. Figure 19 shows the difference in obtained patterns from an amorphous one sample and a crystal sample [132].

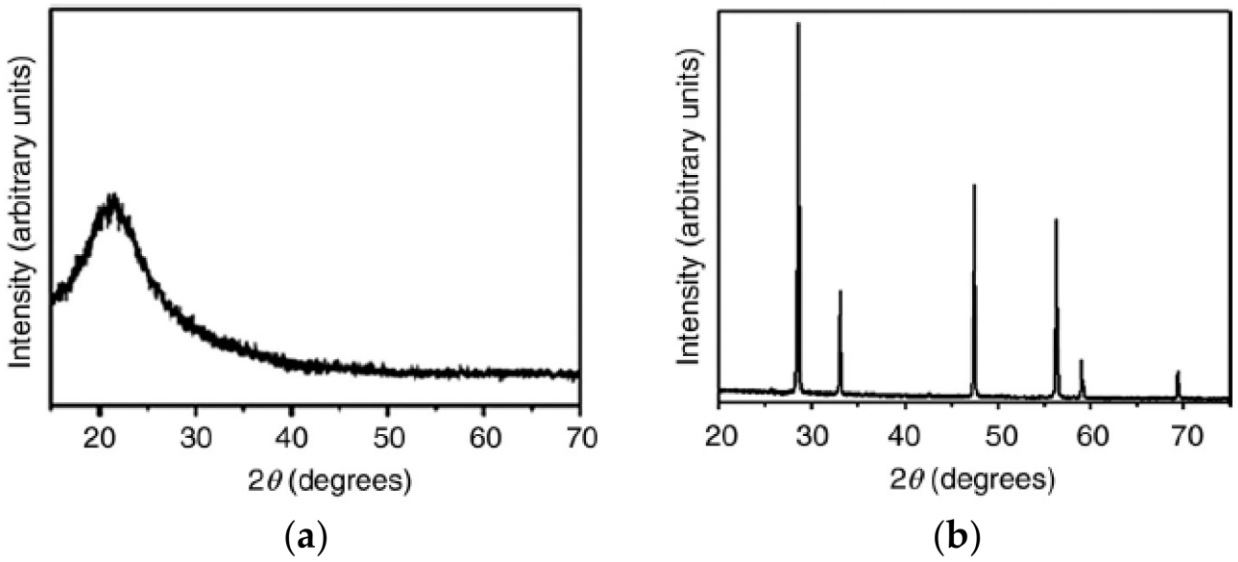

Figure 19. The XRD patterns from (a) an amorphous and (b) a crystallized sample [132]

At the core of XRD lies Bragg's law, a fundamental principle governing the scattering of X-rays by crystalline solids. X-rays interacting with crystal lattice planes produce constructive interference (Figure 20) when the path difference between scattering X-rays equals their wavelength. The path difference depends on the distance between the planes (d) and the angle of incidence (θ, 2θ) at which the X-rays strike the crystal. When Bragg's law is satisfied, diffraction peaks emerge in the XRD pattern, providing essential information about the material's crystal lattice and atomic arrangement. Through this powerful technique, researchers gain a profound understanding of crystallographic information, which forms the foundation of a material's physical and chemical properties [133].

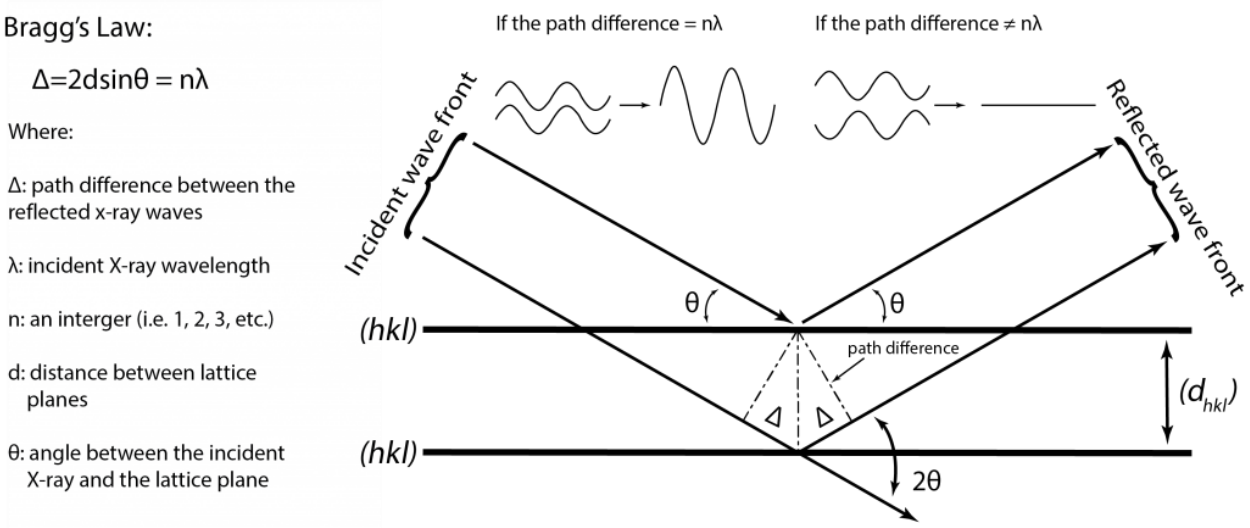

Figure 20. The theory of XRD and Bragg's law [134]

XRD can be used to study zeolite materials, as they are crystalline inorganic solids with unique porous structures. Zeolites exhibit pronounced diffraction peaks in the XRD pattern because of their periodic atom arrangement. Analyzing XRD data from zeolites allows researchers to identify and quantify the crystal phases present, determine lattice parameters, and assess the degree of crystallinity. This critical information supports the study of zeolite materials' catalytic properties, adsorption behavior, and selectivity, making XRD an indispensable tool in zeolite research. Here, the XRD technique was used to verity the proper formation of particular zeolite types and their crystallinity degrees.

3.3.2 NH_3-TPD

Ammonia temperature-programmed desorption (NH_3-TPD) characterization is a widely used technique in catalysis and surface science to study materials' acidic properties. It involves the desorption of ammonia molecules from a solid surface while increasing the temperature gradually. This method provides valuable insights into the nature and strength of acid sites on the surface of catalysts or adsorbents. NH_3-TPD is particularly useful for investigating zeolites, metal oxides, and other porous materials, as well as heterogeneous catalysts employed in various industrial processes [135]. Ammonia will adsorb physically and chemically on catalyst samples, called physisorption and chemisorption. Physisorbed ammonia will desorb at very low temperatures, at the very start of the temperature program, whereas chemisorbed ammonia will require higher

temperatures and the temperature of desorption is related to the strength of the chemical bonds between the ammonia and the acid sites.

In NH_3-TPD (Figure 21), a sample is first pretreated under specific conditions to remove any adsorbed or physisorbed species. For this purpose, the sample should be degassed under the flow of pure He at high temperature. Then, a stream of ammonia gas (for example 10 vol% NH_3 in He) is passed over the sample for a few hours in order to saturate sample. In the next step, sample is then degassed under He flow again and then as the temperature increases, ammonia molecules that had adsorbed on the surface are thermally desorbed, and their desorption is monitored using a detector. The desorption peaks are plotted as a function of temperature, creating a TPD profile, which indicates the different types of acidic sites present on the material's surface and their corresponding desorption temperatures.

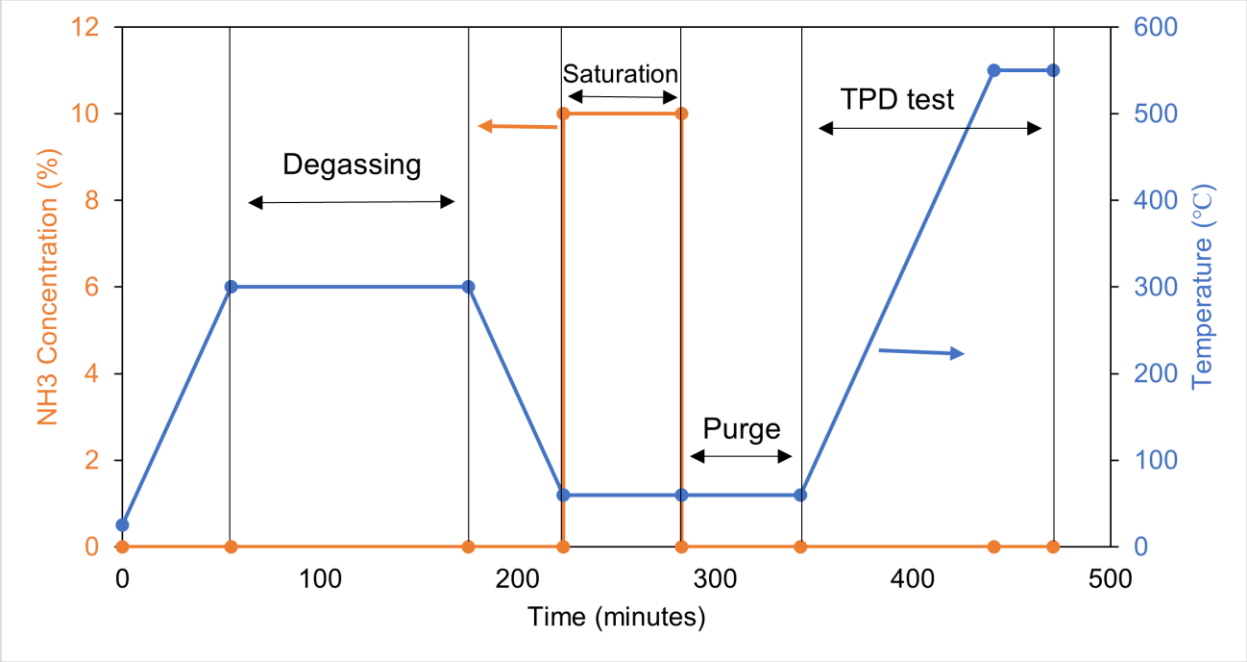

Figure 21. The common process of NH3-TPD test

The interpretation of NH_3-TPD results involves analyzing the desorption peaks in the TPD profile. NH_3-TPD profiles of Cu-CHA, for example, exhibit three desorption peaks, one at low temperatures below 200 °C corresponding to physically adsorbed ammonia, one at intermediate temperatures between 250 °C and 350 °C, and one at temperatures higher than 400 °C. Strongly acidic sites (Bronsted type) tend to desorb ammonia at higher temperatures, whereas weakly acidic sites (Lewis type) desorb at lower temperatures. By comparing NH_3-TPD profiles of different

samples or catalysts, the effect of various factors on surface acidity can be assessed. For instance, the impact of varying template amounts and crystallization time on acidity will be discussed. This information is crucial for optimizing catalysts' performance in various chemical processes, including catalytic cracking, hydrocracking, and selective catalytic reduction (SCR) in environmental applications [136]. In this study, the NH_3-TPD technique was used to measure the Lewis and Bronsted type acidity of the synthesized zeolite catalysts.

3.3.3 DRIFTS

DRIFTS (Diffuse Reflectance Infrared Fourier Transform Spectroscopy) characterization is a valuable and widely used method for investigating catalyst surface properties. It is one of the four common IR absorption spectroscopy methods (Figure 22) used in catalyst studies, offering valuable insights into functional groups of compounds. Figure 23 presents some functional groups wavenumber in a spectroscopy plot. As a result of its unique absorption spectrum pattern for different bonds and molecules, DRIFTS is suitable for both qualitative and quantitative analysis.

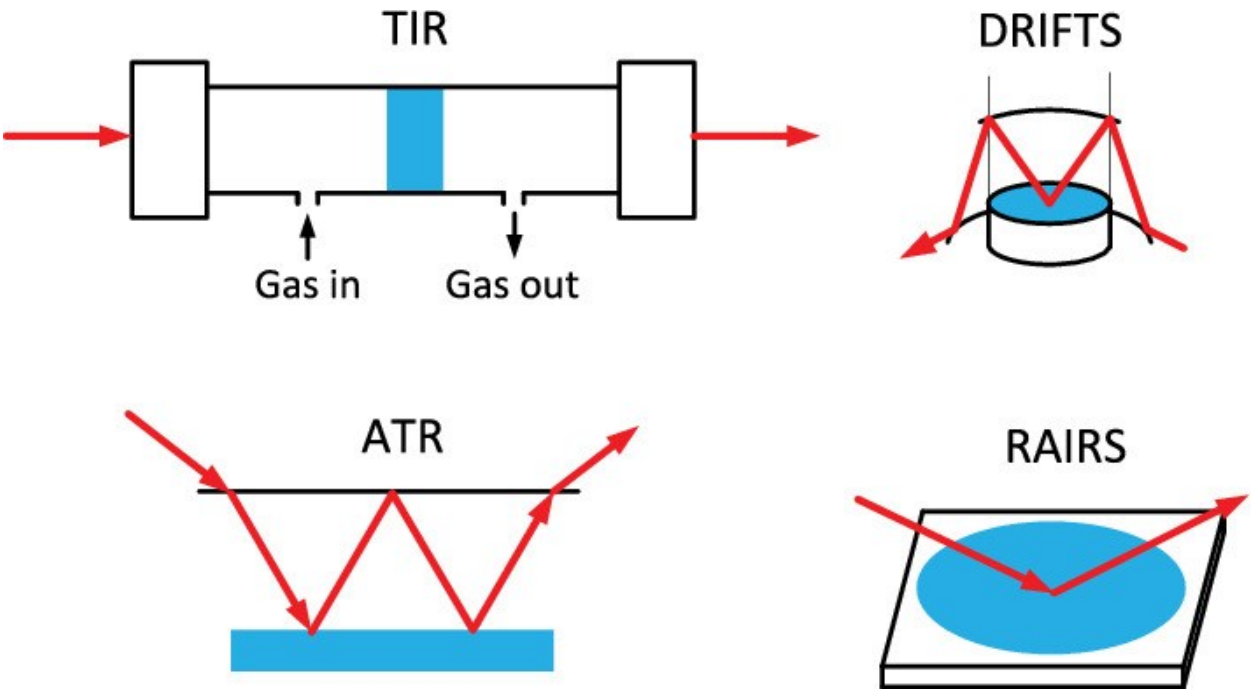

Figure 22. IR spectroscopy methods including transmission IR (TIR), diffuse reflectance Fourier transform (DRIFTS), attenuated total reflection (ATR), and reflection-absorption IR (RAIRS) [137]

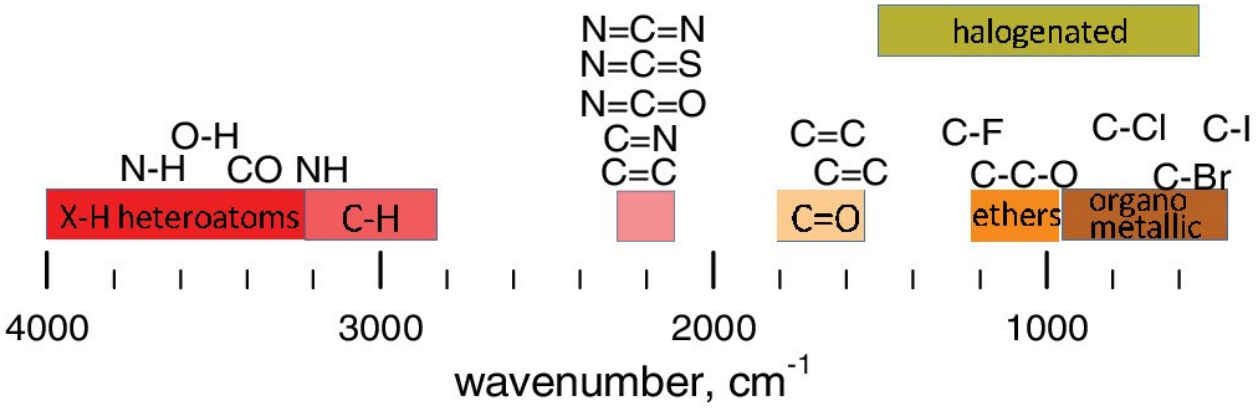

Figure 23. Hydroxyl, nitrile, and some other functional groups in a IR spectroscopy [137].

The DRIFTS technique finds particular application in exploring zeolite acidity. To assess acidity, the sample is dried, degassed, and then saturated with acetonitrile (CH_3CN). Acetonitrile is an excellent option for learning about Lewis and Bronsted acid sites since its interaction with acid sites on zeolites shifts the OH frequency. Due to the overlap of several frequencies, acetonitrile's spectral region can be complex, such as Fermi resonance between vibrations of ─CN, ─CH_3, and C─C bonds. To overcome this complexity, deuterated CD_3CN is used as a better probe molecule, as the CN stretching frequency in the case of CD_3CN more efficiently identifies acid sites in various catalytic materials.

Interpreting DRIFTS spectra by the surface area below peaks is useful for assessing the relative concentration or abundance of specific functional groups or chemical species in a sample. The peaks in the infrared absorbance spectrum correspond to the vibrational frequencies of various chemical bonds in the sample. The area below each peak is integrated or calculated, representing the total absorbance associated with that specific vibrational mode. In the context of analyzing Bronsted and Lewis acid contributions, the surface area below the peaks at 2297 – 2284 cm^{-1} and 2325 – 2310 cm^{-1} can be evaluated, respectively [138]. The interaction of CN group with Bronsted (donating H^+) and Lewis (accepting electron) acid sites are depicted in Figure 24 [139]. These interpretations provide crucial information for understanding the acidity and reactivity of catalysts and other solid materials, contributing to advancements in various scientific and industrial applications.

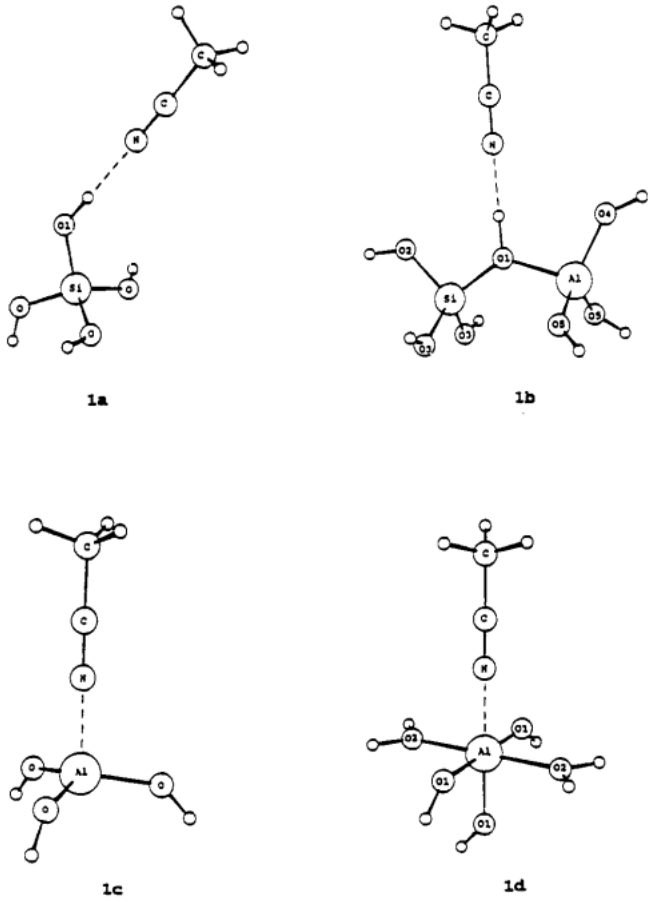

Figure 24. The interaction of CN group in acetonitrile with Bronsted (1a and 1b) and Lewis (1c and 1d) acid sites [139]

3.3.4 SEM

Scanning electron microscopy (SEM) is a powerful imaging technique used in materials science and various other fields to examine samples' surface morphology and microstructure at high resolution. SEM allows researchers to obtain detailed information about the shape, crystallography, size, and distribution of particles in a wide range of materials. It works by scanning a focused electron beam with energy between 0.1 and 30 keV over the specimen's surface. The interactions between the beam and the sample produce various signals, such as secondary electrons, backscattered electrons, and characteristic X-rays, which are detected and used to generate SEM images [140]. Figure 25 shows a schematic drawing of an SEM instrument [141].

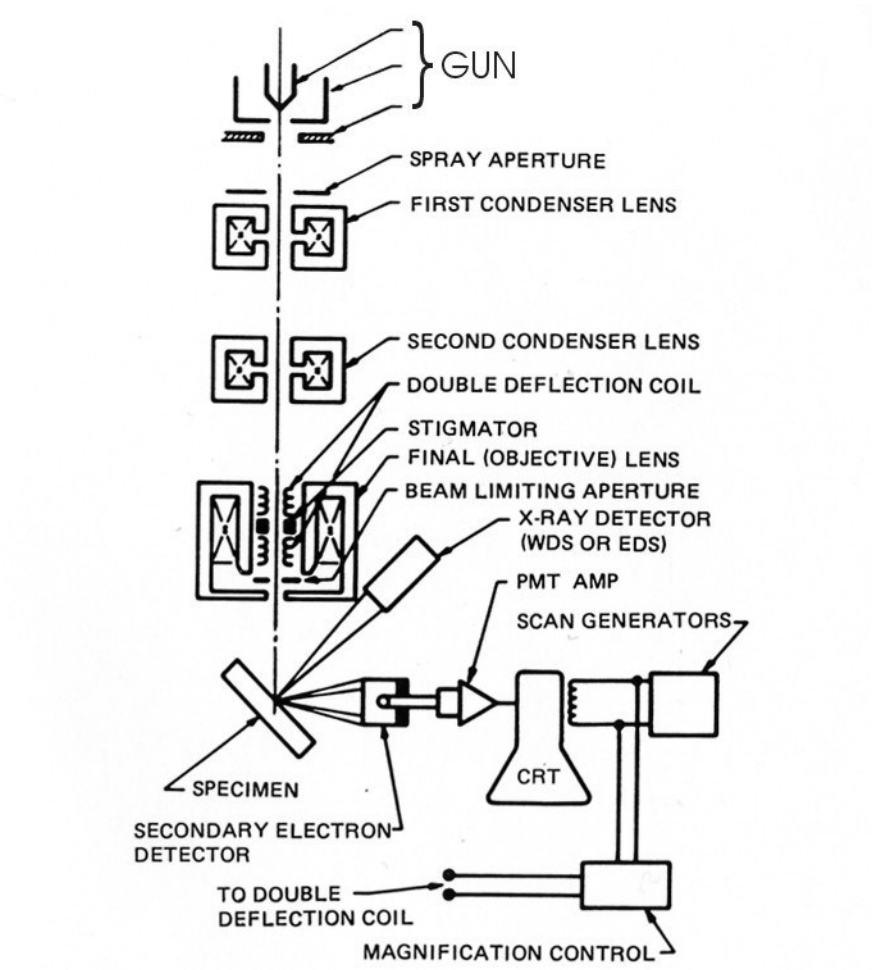

Figure 1.11. Schematic drawing of the electron and x-ray optics of a combined SEM–EPMA.

Figure 25. Schematic drawing of an SEM instrument [141]

In a conventional vacuum SEM, the electron-optical column and specimen chamber must maintain high vacuum conditions to minimize unwanted scattering. Coating insulating specimens with a conductive layer is essential to establish an electrical discharge path, preventing surface electrical charges resulting from beam electron impacts. In contrast, the variable pressure SEM (VPSEM) offers a pressure range from 1 Pa to 2000 Pa in the specimen chamber. In this case, ionized gas atoms automatically discharge uncoated insulating surfaces [140].

To perform SEM characterization of zeolite materials, the sample is first prepared by coating it with a thin layer of a conductive material, such as gold, to enhance its surface conductivity and prevent charging effects during imaging. The prepared sample is then placed in the SEM chamber,

and the electron beam is scanned across its surface. As the beam interacts with the sample, various signals are detected and used to construct detailed images of the sample's surface features.

Moreover, Energy-Dispersive X-ray Spectroscopy (EDS) is a powerful analytical technique commonly used in conjunction with Scanning Electron Microscopy (SEM) to determine the elemental composition of materials. EDS allows researchers to identify and quantify the different chemical elements present in a sample based on counting the X-rays emitted when the sample is bombarded with the electron beam from the SEM. These emitted X-rays are unique to each element and have specific energies, enabling EDS to generate a characteristic energy spectrum that corresponds to the elements present in the sample. By analyzing this spectrum, researchers can gain valuable insights into the material's composition and distribution of elements, making EDS an invaluable tool for a wide range of applications in materials science, such as zeolites [142].

In this study, SEM is used to examine the morphology of different synthesized zeolite samples and the EDS is used to measure the Si/Al ratio. It is noteworthy to mention that considering the electron penetration of 2 μm, EDS analysis is suitable for analyzing the Si/Al ratio in zeolite samples since it is larger than the particle size [143].

3.3.5 TGA

Thermogravimetric Analysis (TGA) is a versatile and widely used analytical technique in materials science and chemistry to study the thermal stability, decomposition, and weight changes of a sample as a function of temperature or time. TGA is especially valuable for characterizing the thermal behavior of materials, including polymers, composites, pharmaceuticals, and catalysts. The technique involves subjecting the sample to a controlled temperature ramp in a controlled atmosphere while continuously monitoring its weight changes. As the sample undergoes thermal events, such as evaporation, decomposition, or oxidation, its weight changes are recorded, providing valuable information about the sample's thermal properties, composition, and stability [144].

To perform TGA, a small amount of the sample (usually a 5 - 20 mg) is placed in a crucible or sample pan, which is then placed inside the TGA instrument. The instrument is equipped with a precise heating system and a highly sensitive balance to measure the sample's weight. The temperature is ramped up gradually, and the weight of the sample is continuously recorded as a

function of temperature or time. The choice of the atmosphere (e.g., air, nitrogen, or inert gas) depends on the specific application and the desired information. For example, an inert gas atmosphere is used when studying the thermal degradation of materials to avoid unwanted reactions with oxygen. Also, in the case of coke analysis, the TGA would be conducted under synthetic air flow for coke burning.

Interpreting TGA results involves analyzing the weight loss or gain patterns over a temperature or time range. The weight loss events observed in the TGA curve correspond to different thermal processes occurring in the sample, such as evaporation of volatile components, decomposition of organic materials, or oxidation of the sample. For example, in coke measurement, weight loss at low temperatures is associated with the water desorption and drying process. In contrast, weight loss at > 200 °C can be related to burning reactions [145]. TGA data are often complemented with other techniques such as Differential Scanning Calorimetry (DSC) to gain a more comprehensive understanding of the sample's thermal properties and behavior. Overall, TGA is a valuable tool for studying thermal processes and understanding materials' behavior under different temperature conditions. This makes it essential for research, development, and quality control in various industries.

In this study, the use of TGA is useful to determine the amount of coke formation on zeolite samples after the long-term (stability) reaction testing. Also, it was used to find the coke selectivity to in methanol conversion and the rate of coke generation for various zeolite types.

3.3.6 BET surface area and pore size distribution

Nitrogen adsorption/desorption profiles, along with BET analysis, pore size distribution, and T-plot characterization, are fundamental techniques used to investigate the porous properties of materials, such as adsorbents, catalysts, and porous solids. These methods provide valuable information about the specific surface area, pore size distribution, and porosity of materials, which are crucial factors in understanding their performance in various applications.

The N_2 adsorption/desorption profile is obtained by measuring the amount of nitrogen gas being absorbed onto a material's surface as a function of relative pressure at a specific temperature. During adsorption, gas molecules accumulate on the surface and fill the available pores, leading to an increase in the adsorbed amount. In the desorption process, the adsorbed gas is removed from

the surface as the relative pressure is decreased. The resulting isotherm, which represents the equilibrium between adsorption and desorption, provides valuable data for further characterization. Figure 26 illustrates various types of N_2 adsorption isotherms. Based on the IUPAC classification, the isotherm of type I is assigned to microporous materials, types II, III, and VI represent the nonporous or macroporous compounds, and types IV and V exhibit the mesoporous structure [146]. For clarification, the terms microporous, mesoporous, and macropores refer to pores <2 nm, 2-50 nm, and >50 nm, respectively [147].

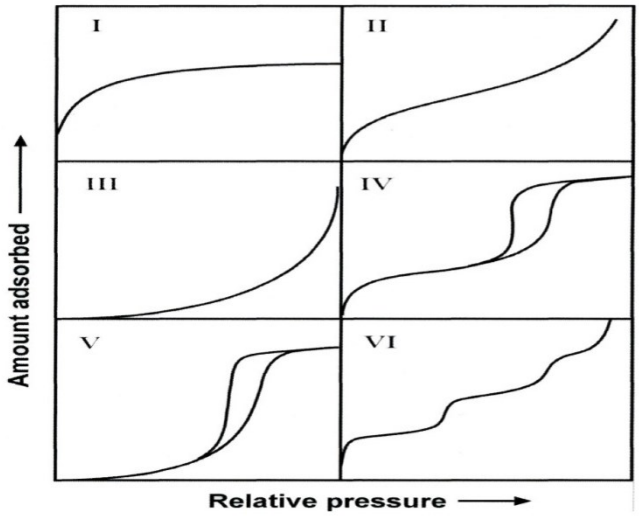

Figure 26. The 6 types of IUPAC classification for N_2 adsorption/desorption isotherms [146].

BET analysis is based on the N_2 adsorption isotherm and involves determining the specific surface area of the material. The BET method assumes that adsorption follows multilayer adsorption on a homogeneous surface, and it utilizes a mathematical model (eq. 7) to fit the experimental data. As defined in the BET model, V_t and V_m represent the volume of adsorbed N_2 on the surface at P/P_0 and the first monolayer. In this formula, P_0 indicates the condensation pressure, while C represents the BET constant. This information is vital in understanding the material's reactivity, adsorption capacity, and catalytic performance [148].

$$\frac{P}{V_t(P_0-P)} = \frac{1}{V_m C} + \frac{C-1}{V_m C}\left(\frac{P}{P_0}\right) \quad (7)$$

Pore size distribution is another analysis that can be performed through N_2 adsorption/desorption profiles. Various models, such as BJH or DFT methods, can be used to determine the distribution of pore sizes and understand how pore size impacts the material's performance in terms of

adsorption and diffusion processes. The pore size distribution data is beneficial for optimizing the selectivity of the catalytic process and gas adsorption and separation [149].

The T-plot method is a combination of BET and pore size distribution analyses, allowing for a more detailed characterization of materials with complex pore structures. By plotting the amount of adsorbed gas at a specific relative pressure against the thickness of the adsorbed gas layer, researchers can distinguish between micropores and mesopores and obtain information about the surface area and pore size distribution in different pore regimes. An example of a t-plot analysis is shown in Figure 27 [150]. This approach provides a deeper understanding of the material's porosity and allows for the tailored design of materials with specific pore structures to suit particular applications.

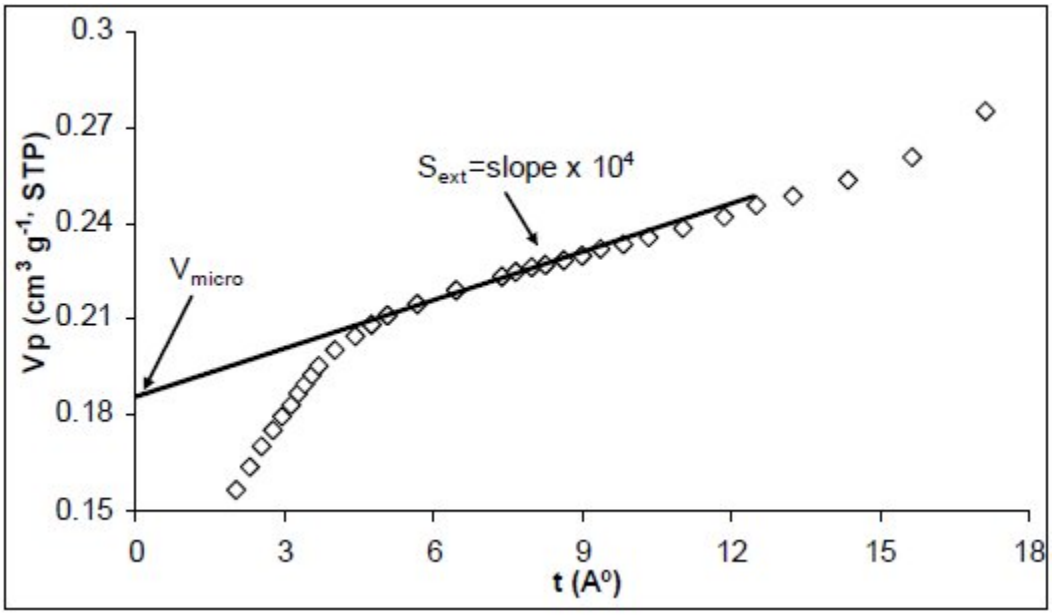

Figure 27. Calculating the $V_{micropores}$ and $S_{external}$ by t-plot method [150].

In this study, BET surface area measurement and T-plot analysis of the pore size distribution are used to understand the effect of the different synthesis methods on these properties and the resultant catalytic activity.

CHAPTER 4: DME PRODUCTION USING METHANOL OVER RHO-TYPE ZEOLITE WITH DIFFERENT PREPARATION METHODS

4.1 Abstract

Energy supply is a significant concern that can be addressed by developing sustainable energy sources. Dimethyl ether (DME) shows remarkable promise in this regard, as it finds applications in diesel fuel engines, LPG systems, and serves as an excellent carrier for H_2. In this study, various RHO samples were synthesized by modifying preparation parameters and evaluated for their performance in this reaction. Through characterization analyses such as XRD, BET, NH_3-TPD, SEM, EDS, and reactor experiments, it was determined that the optimized sample with the highest crystallization degree and optimum weak/strong acid sites ratio of 1.49 effectively addressed the limitations of previous catalysts such as high-temperature requirements and rapid deactivation. The RHO sample achieved the highest conversion rates at temperatures as low as 190°C, maintaining its efficacy for several days. It was observed that the RHO sample performed superior to common MFI (ZSM-5) zeolite for this reaction owing to its higher acidity (2561 μmol g^{-1} against 1942 μmol g^{-1}) and surface area (671 m^2 g^{-1} vs 233 m^2 g^{-1}). These findings highlight the potential of DME as a sustainable energy source and emphasize the importance of optimizing catalyst preparation to improve DME production efficiency and cost-effectiveness.

4.2 Introduction

The energy supply crisis will be one of the most severe problems that society will have to deal with in the future [151]. This is because most industries and transportation fuel consumption currently rely on fossil fuels, which are limited resources. According to the International Energy Agency (IEA), fossil fuels contribute more than 65% of world energy consumption, while biofuels account for 10% [152]. Additionally, governments have also passed strict laws regulating the gases released from fossil fuel combustion because of the adverse effect these emissions have on the climate [153]. In response to global warming and high energy demands, scientists are investigating renewable and sustainable energy sources to replace non-renewable fossil fuels and alleviate society's concerns. Dimethyl ether (DME) is a promising environmentally friendly chemical for hydrogen carrier and power generation since it can be derived from biomass, natural gas, waste,

and CO_2 capture [51,154]. Due to its low emissions of SO_2, CO, and nitrogen oxides (NOx) gases as well as PM (particulate matter), DME combustion is an effective method of reducing air pollution. In addition, the similar features of DME compared to diesel and liquefied petroleum gas (LPG) allow for the reuse of existing infrastructure with minimal changes, which makes it a cost-effective alternative to fossil fuels [37]. Another use of DME is as a source of hydrogen for fuel cell feed [155].

There are two routes through which DME can be produced: the direct method (one step) and the indirect method (two steps) [156]. In the direct method, methanol is synthesized and dehydrated simultaneously in a single reactor containing a bifunctional catalyst. On the other hand, the two-step route, which has been of primary interest to industries, is performed in two separate reactors, with a separation unit installed between reactors to separate methanol from other gases. A Cu-ZnO-Al_2O_3 catalyst with Zr, Mn, La, and Ce promoters is commonly used in CO/CO_2 hydrogenation reactions to reach methanol [157–160], whereas solid acid catalysts such as γ-Al_2O_3, zeolites, heteropoly acid catalysts (HPAs), aluminum phosphate, have been investigated for methanol dehydration [69,88,161].

γ-Al_2O_3 is the most frequently used catalyst for the industrial methanol dehydration reaction, however there are drawbacks such as their inactivity at low temperatures and super hydrophilicity. These drawbacks have led researchers to seek more active and stable catalysts [162]. Other types of alumina, such as η-, γ-χ-Al_2O_3, or modifications by incorporating CuO, Fe_2O_3, ZrO_2, Nb_2O_3, and TiO_2, have been studied for this reaction but results were not improved significantly. For example, Armenta et al. [163] examined γ-χ-Al_2O_3 modified by Fe_2O_3 nanoparticles and reported 46% methanol conversion at 250 °C while Hosseini et al. [85] achieved 20 % conversion over γ-χ-Al_2O_3 at same temperature. In another study, Osman et al. evaluated the performance of a η-Al_2O_3 catalyst with a 10% Ag promoter to enhance hydrophobicity and Lewis acidity strength, but it was unable to achieve equilibrium methanol conversion even at temperatures as high as 300 °C [89]. Due to thermodynamic limitations for methanol dehydration at high temperatures, catalysts with a high acidity are more suitable for achieving equilibrium conversion at temperatures below 250 °C.

Zeolites with different porous structures have demonstrated superior methanol dehydration activity due to their high acidity, adjustable porosity, and large specific surface area [164]. Despite zeolite

types exhibiting catalytic activity at lower temperatures and not being poisoned by water, coke formation and by-products are the major problems associated with their use. For example, Mordenite type zeolite presented equilibrium conversion at 220 °C, but it could not keep this activity for more than few hours [72]. FER and MFI (ZSM-5) zeolites have demonstrated highest activity and stability among other types for DME production. Catizzone et al. reached to 80-85 % methanol conversion at 240 °C with weight hour space velocity (WHSV) of 4 $g_{MeOH}\ g_{cat}^{-1} h^{-1}$ using mentioned catalysts [123]. Migliori et al. achieved same results over FER and MFI and also recorded 60 h stability at 200 °C [72]. In addition, Masih et al. developed RHO and KFI zeolites with high acidity (2.53 mmol g^{-1} and 1.65 mmol g^{-1}, respectively) and exhibited equilibrium conversion at 200 °C with low WHSV of 1 $g_{MeOH}\ g_{cat}^{-1} h^{-1}$ and 24 h stability [121]. The catalysts showed good activity at low temperatures, but the methanol flow and stability were not suitable for scaling up.

Furthermore, the physical and chemical properties of zeolites play a critical role in their activity and application. A catalytic application, for example, can be affected by physicochemical properties such as crystal size, morphology, surface area, and acidity. It is possible to modify these characteristics during preparation by adjusting parameters such as pH, the temperature and time of crystallization, template or structure directing agent, stirring speed, amount of water, Si/Al ratio, and concentration of alkali metal ions [165,166].

In this study, the effect of different precursor ratios and crystallization times on the performance of RHO zeolites for methanol dehydration is evaluated. Five RHO zeolites were synthesized with varying conditions to investigate their effects on physical-chemical properties and catalytic activity for methanol dehydration. Commercial catalysts including MFI, SAPO-34, and γ-Al_2O_3 have been used to compare the activity at the same operation condition. The reactor experiments have been carried out at temperatures ranging between 140 and 220 °C under 4 $g_{MeOH}\ g_{cat}^{-1}\ h^{-1}$ to assess the catalysts' activity and find the optimum temperature for highest conversion. Also, long term experiments have been perform using the optimum catalyst and commercial ones over 100 h to examine the stability for massive and long term production.

4.3 Experimental

4.3.1 Catalyst synthesis

Three commercial catalysts were used as reference materials for DME production, including MFI zeolites (Si/Al = 15 and 25, labeled MFI_15 and MFI_25, respectively) obtained from Clarient Co., and γ-Al_2O_3 catalyst purchased from Alfa Aesar. The synthesis procedure of the employed SAPO-34 catalyst has been explained elsewhere [167].

The materials employed in this study for the synthesis and activation of RHO zeolites included sodium hydroxide (NaOH, 97%, ACP chemicals), sodium aluminum oxide ($Al_2O_3.Na_2O$, Thermo Fisher Scientific), 18-Crown-6 ($[C_2H_4O]_6$, 99%, Thermo Scientific), cesium hydroxide monohydrate ($CsOH.H_2O$, 96%, Alfa Aesar), colloidal silica (SiO_2, 40 w% solutions in water, LUDOX AS-4O, Sigma Aldrich), and ammonium chloride (NH_4Cl, 99.5%, Sigma Aldrich).

RHO zeolites with a Si/Al ratio of 5 were synthesized using two hydrothermal crystallization methods, one with a template and one without, following the procedure reported in reference [168]. Initially, four catalysts were synthesized with varying Si:T (template) ratios: 10:0.5, 10:0.25, and 10:0, under hydrothermal reactor conditions for 7 and 8 days. Subsequently, the selected catalyst based on the results of activity tests was reproduced using hydrothermal processing times of 6, 8, and 10 days.

For the first method, a solution was prepared by mixing sodium hydroxide, deionized water, and cesium hydroxide under stirring in a 50 mL beaker. Once a clear solution was achieved, sodium aluminum oxide and 18-Crown-6 were added sequentially, followed by 10 minutes of stirring to obtain a clear solution. Finally, colloidal silica was added dropwise to the solution while stirring at 1000 RPMs. The resulting gel with a composition of $1.8K_2O{:}1Al_2O_3{:}0.3CsO{:}0.5$(18-C-6)$:10SiO_2:100H_2O$ (for Si:T = 10:0.5 case) was stirred for 24 h. The gel was then transferred into a Teflon vessel and surrounded with a steel bomb (Parr Instruments Acid Digestion Vessel 45 mL), and hydrothermal crystallization was performed under pressure at 110 ℃ for 6, 8, and 10 days (Thermo Scientific™ Heratherm™ General Protocol Oven). After completion, the mixture was then filtered and washed until the filtrate reached a neutral pH, and the resulting solid was dried overnight at 60°C for 10 h, followed by calcination at 550 ℃ for 3 h (Thermo Scientific™ Thermolyne™ Muffle Furnace). The zeolites obtained from this process were labeled as

RHO_XTY where X = 0.5, 0.25, 0 represents the amount of template (full, half, and zero) and Y = 6, 8, 10 indicates the duration of hydrothermal processing.

Due to the formation of an amorphous structure when the template was removed using the first method, one additional sample was synthesized using an alternative preparation procedure. This method followed a similar procedure to the previous one but with a different gel composition. The NaOH, $CsOH.H_2O$, and $Al_2O_3.Na_2O$ powder was added sequentially to deionized water, with 10 minutes of stirring between each step. The resulting gel had a composition of $3.0K_2O:1.0Al_2O_3:0.4CsO:10.8SiO_2:110H_2O$ and was stirred for 24 h. It was then transferred into a Teflon vessel to undergo hydrothermal crystallization under pressure at 100 ℃ for 7 days. After the hydrothermal treatment, the mixture was washed until the filtrate reached a neutral pH. The obtained solid was dried overnight at 60 ℃ for 10 h and calcined at 550 ℃ for 3 h. The prepared zeolite was designated as RHO_0T7.

To convert the zeolites into their active H-form for methanol dehydration, an ion-exchange process using an NH_4Cl solution was employed. The ion-exchange procedure consisted of three cycles while in each cycle, 1 gram of zeolites was dissolved in 100 ml of 1 M NH_4Cl solution and stirred for 1.5 h at 80 ℃. Subsequently, the solution was filtered, and the zeolite residue was thoroughly washed with deionized water. To complete the transformation from the NH_4-type to the H-type zeolites, the resulting material underwent a final step of calcination at 600 ℃ for 5 h.

4.3.2 Characterization

The characterization of the synthesized zeolites and catalysts was carried out using various techniques. Powder X-ray diffraction (XRD) analysis was conducted using a Rigaku SmartLab SE X-ray diffractometer with Cu Kα radiation operating at 40 kV and 44 mA. The analysis involved collecting patterns in the 2θ range of 5° to 80°, with a scanning rate of 0.08° s^{-1}. This analysis aimed to confirm the completion of the crystallization process during zeolite preparation.

The textural properties, such as specific surface area and pores volume, were evaluated using N_2 adsorption. The adsorption measurements were carried out using a 3FLEX Surface Characterization (ATS Scientific Inc.) automated gas adsorption system at a temperature of liquid nitrogen (−196 ℃). Before the analysis, the degassing process was conducted for a 12 h at 150 ℃. The micropore volumes and mesopore volumes were determined by applying the Harkins and Jura

(T-plot analysis) and BJH model (Kruk–Jaroniec–Sayari empirical procedure) models, respectively, and the specific surface area was measured using BET (Brunauer–Emmett–Teller) theory.

The acidity of the samples was determined using temperature-programmed desorption of ammonia (NH_3-TPD). The NH_3-TPD analysis was performed on Altamira AMI-300 equipment, measuring the NH_3 concentration with a thermal conductivity detector (TCD). Prior to the analysis, the samples were degassed for 2 h at 300 ℃ with a flow of pure helium. The desorption process involved cooling the sample to 60 ℃ and exposing it to a mixture of 10 vol.% NH_3 and balanced in helium gas. After an hour, unstable adsorbed NH_3 was removed by purging under helium flow, and then the desorption was carried out by gradually elevating the temperature. The ammonia desorption profile was measured between 60 – 550 ℃ under a constant flow of helium (10 mL/min).

Scanning electron microscopy (SEM) was employed to study the surface morphology and particle size distribution of the catalysts. SEM analysis was performed employing a S-3400N HITACHI equipment at 15 kV. The samples were prepared on aluminum slabs by sputter-coating with gold layer, for clear imaging. Additionally, the attached Link Pentafet OXFORD instrument was employed to carry out energy-dispersive spectroscopy (EDS) to calculate the Si/Al ratio in both the synthesized and commercial zeolites. A sample size containing 45-55 particles was measured to determine the average particle size.

Thermogravimetric analysis (TGA/DTA) was conducted using a Netzsch TG 209 F1 instrument to quantify the amount of coke formed on the catalysts after running the methanol dehydration reaction for 100 h. The loaded sample holder (alumina crucible) with ~ 20 mg catalyst was heated at temperatures between 25 ℃ and 900 ℃ at a ramp rate of 5 ℃ min^{-1} under an air atmosphere (30 mL min^{-1} flow). Also, the process was kept at 200 ℃ and 600 ℃ for 30 min to remove water content and coke deposited entirely. The water desorption quantity measured at temperatures below 200 ℃ was utilized to create the TGA figure and determine the coke content based on the weight of the dried catalysts. Furthermore, the investigation of the used catalysts aimed to explore the characteristics of coke generated during methanol dehydration. To accomplish this, the zeolite structure was digested using a 4 M KOH solution, followed by extraction of the coke utilizing CH_2Cl_2 as the solvent. The solvent containing the coke was then injected into a GC-MS apparatus,

with a solvent delay of 3 minutes. The coke analysis was performed at temperatures ranging from 50 ℃ to 300 ℃.

To assess the Bronsted and Lewis acid sites in the employed catalysts, DRIFTS (Diffuse Reflectance Infrared Fourier Transform Spectroscopy) analysis was conducted using Nicolet™ iS50 FTIR Spectrometer. The analysis was performed at 4 cm^{-1} optical resolution with a Mercury Cadmium Telluride (MCT) detector. For this purpose, saturated zeolite samples were prepared by drying at 300 ℃ for 2 h under N_2 flow. Subsequently, the samples were exposed to deuterated acetonitrile (CD_3CN) vapor in an N_2 gas atmosphere at room temperature for 2 h. To ensure the removal of physically adsorbed acetonitrile, samples were purged by nitrogen flow for 2 h at 50 ℃ prior to conducting the DRIFTS analysis.

4.3.3 Activity experiments

The methanol dehydration process was studied in a fixed-bed quartz reactor within an electric furnace. Two sets of experiments were conducted to examine the effects of temperature on DME synthesis. For the zeolite samples, temperatures ranging from 130 ℃ to 220 ℃ were employed, while for the γ-Al_2O_3 samples, temperatures ranging from 130 ℃ to 310 ℃ were utilized under atmospheric pressure. To analyze the input and output gas composition, a gas chromatograph (GC) equipped with an FID detector used, employing a HP plot Q column. The catalyst temperature at the top of the bed was monitored using a K-type thermocouple. Methanol condensation was prevented by heating the feed gas line to 120 ℃ before it entered the reactor. Each experiment involved the use of 100 mg of catalyst, which underwent pretreatment at 500 ℃ for zeolites and 400 ℃ for γ- Al_2O_3. The pretreatment was conducted under a flow of pure argon at a rate of 20 mL min^{-1} for 1 hour. Subsequently, the temperature was reduced to 125 ℃ and a mixture of methanol and argon gas flowed. The liquid methanol was fed into the heated lines, where it was combined with the argon flow to yield a gas mixture including 30 vol.% methanol in balance Ar. The weight hour space velocity (WHSV) was set to 4 $g_{MeOH}\ g_{Catalyst}^{-1}\ h^{-1}$, and the total flow rate was set to 22 mL min^{-1}. To ensure data collection under steady-state conditions, product analysis was performed every 30 minutes over a period of 3 h at each temperature point.

A replicate activity test was performed with the RHO zeolite sample (RHO_0.5T8) prepared with Si:Template = 10:0.5 and 8 days of crystallization (Figure 66). The reproducibility of results was

also confirmed by comparing methanol dehydration over RHO_0.5T10, MFI_15, and MFI_25 catalysts at a specific temperature in two different experiments.

4.4 Results and discussion

4.4.1 Characterization

Figure 28 depict the recorded XRD profile of prepared RHO zeolites. Several peaks at 8.36, 14.4, 25.1, 26.42, 28.2, 30.32, 32.56, and 35.74° were recorded which are attributed to RHO crystal phases and are in line with previous papers [169,170]. The comparison between XRD patterns of the RHO_0T8 and RHO_0.25T8 evidently indicates the significant effect of the presence of the template in the initial gel on the crystallization process. The sample without the template showed an amorphous structure while employing the template resulted in a highly crystallized zeolite. The crystallization process was initiated by incorporating an alternative method for removing the template; however, not all phases were observed. The crystallization degree is an important factor in the catalytic activity of zeolites which will be discussed later. The space between drawn baselines and XRD patterns reveals the amorphous degree of synthesized samples. Therefore, the best-crystalized sample was obtained by using Si:T ratio of 10:0.5 and 10:0.25 in the prepared solution followed by 8 and 10 days of crystallization. Also, the peak at 14.4 (2θ) had more intensity for zeolites with a template compared to the reference pattern and the sample without a template. A similar peak was observed in the XRD pattern of zeolites after activation (Appendix A, Figure 53), which reveals the importance of this phase on catalyst activity. Moreover, the crystallinity of RHO_0.5T10 was more than RHO_0.5T8 and RHO_0.25T8 in Figure 53.

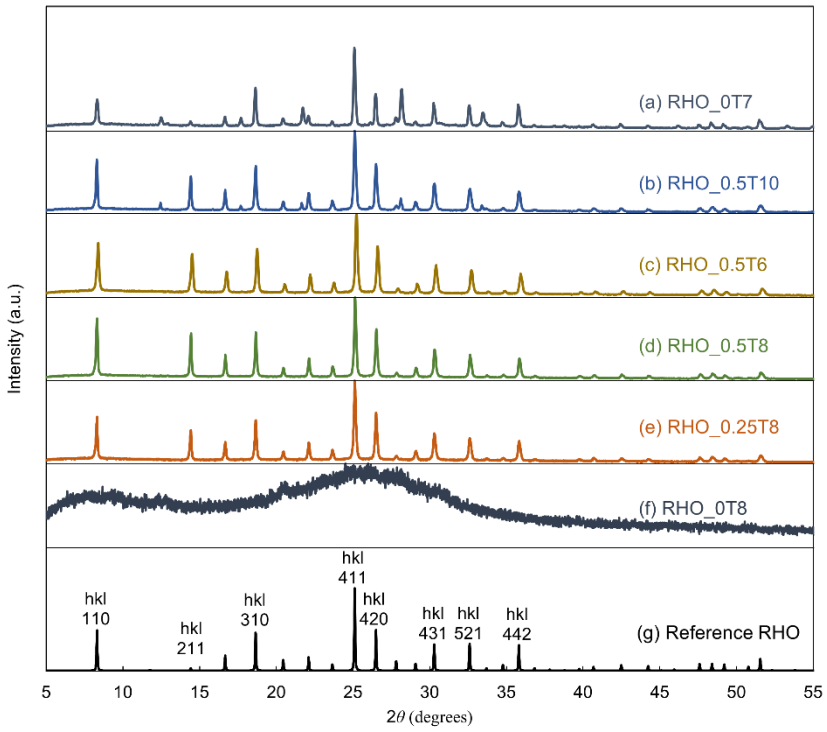

Figure 28. XRD analysis of synthesized RHO zeolites using different conditions including (a) RHO_0T7, (b) RHO_0.5T10, (c) RHO_0.5T6, (d) RHO_0.5T8, (e) RHO_0.25T8, (f) RHO_0T8, (g) reference RHO [120].

A spherical shape morphology was observed in the SEM images of synthesized RHO zeolites and commercial MFI zeolites, as shown in Figure 29. These results are consistent with XRD analysis, demonstrating that template-assisted crystallization is a more suitable method for producing uniform, well-structured RHO zeolites. SEM images showed that RHO zeolites have an average particle size of 1.17 – 1.20 μm when the template was added to the initial solution. Although the alternative method for removing the template successfully achieved a crystalized structure, the particle size of the produced zeolite was around 0.83 μm which may affect adversely catalytic activity. As a result, particle sizes can be reasonably controlled when 18-Crown-6 is present. Additionally, MFI_15 and MFI_25 were measured to have crystal sizes of 7.70 ± 0.24 μm and 0.38 ± 0.01μm.

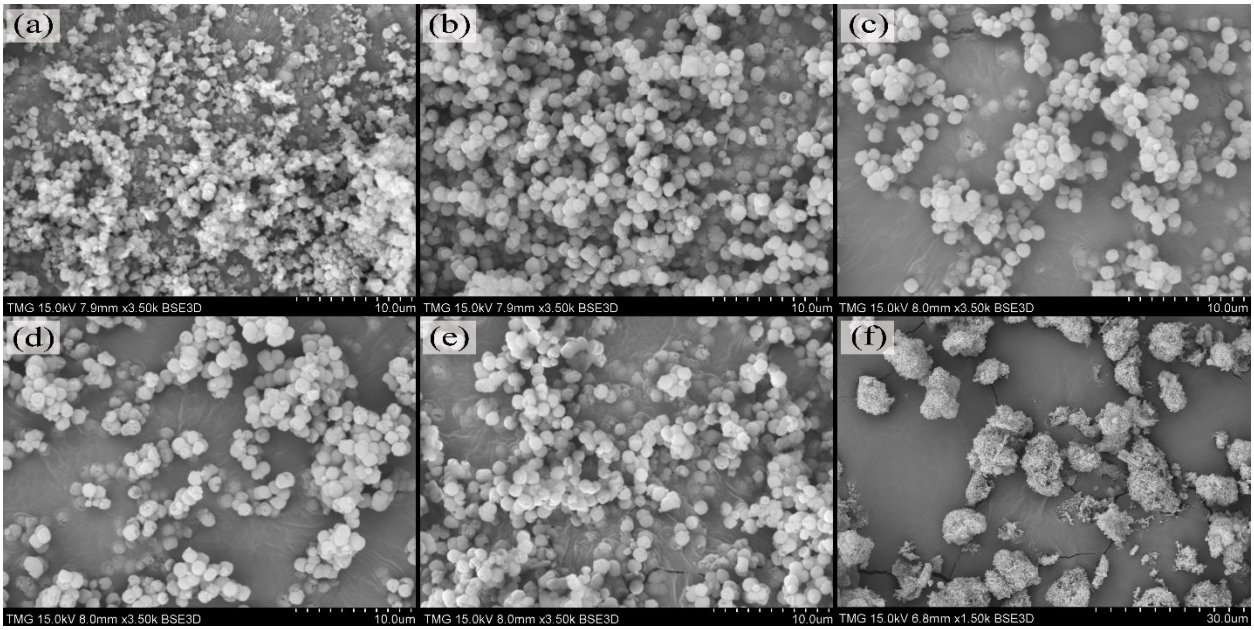

Figure 29. SEM results of crystallized RHO zeolites including (a) RHO_0T7, (b) RHO_0.5T10, (c) RHO_0.5T6, (d) RHO_0.5T8, (e) RHO_0.25T8, and (f) MFI_15.

The N_2 adsorption/desorption patterns for synthesized zeolites are shown in Figure 30. At low relative pressure (P/Po), the isotherms showed sharp increases in adsorbed volume without hysteresis in the adsorption/desorption loop. This can be assigned to a microporous structure based on the IUPAC classification [171]. Table 4 presents the chemical and physical properties of commercial and prepared catalysts derived from different analyses. Based on the EDS analysis, the obtained zeolites had a Si/Al ratio of 4.2 when the template was incorporated into the synthesis. RHO_0T7, on the other hand, had a Si/Al ratio of 3.1, which is in agreement with the reported result [121]. From this it can be observed that the template plays a significant role in retaining the Si/Al ratio around the initial gel. Based on the BET surface area calculation, samples incorporating the template had a surface area of more than 671 $m^2\ g^{-1}$. As shown by the lower surface area of 462 $m^2\ g^{-1}$ for RHO_0T7, a template is crucial for obtaining the maximum surface area for catalytic activity. The nanosized particle size of MFI_25 as well as the different preparation procedures led to a higher BET for MFI_25 than for MFI_15. A T-plot analysis for RHO_0.5T6, RHO_0.5T8, and RHO_0.5T10 indicated that higher processing time contributed to the development of pores with greater micro-distribution.

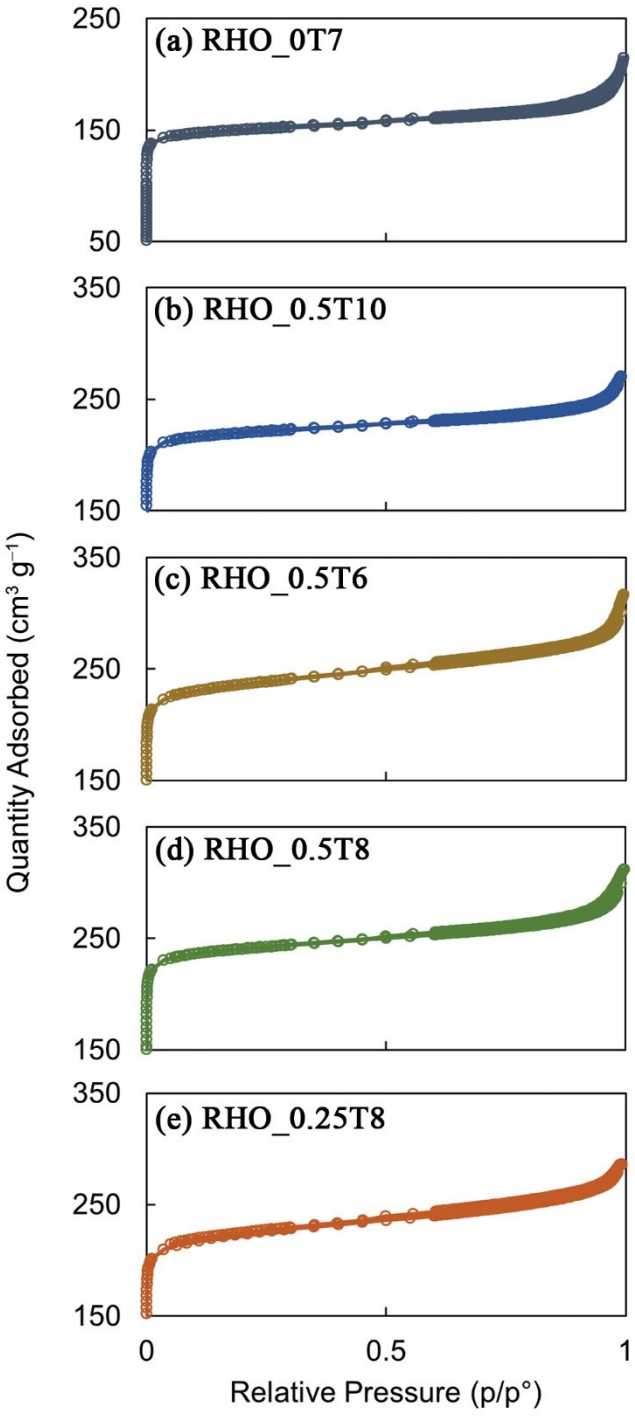

Figure 30. The path of N_2 adsorption–desorption isotherms of synthesized zeolites: (a) RHO_0T7, (b) RHO_0.5T10, (c) RHO_0.5T6, (d) RHO_0.5T8, (e) RHO_0.25T8.

Table 4. PhysicoChemical features of synthesized and commercial catalysts.

Sample	Si/Al ratio [a] of crystal (gel)	S_{BET} [b] (m^2 g^{-1})	Micropore distribution [c] (%)	$V_{micropore}$ [d] (cm^3 g^{-1})	Pore diameter (Å)	Crystal size [e] (μm)
RHO_0.5T8	4.2 (5)	735	86.6	0.330	26.1	1.19 ± 0.03
RHO_0.5T10	4.1 (5)	671	87.6	0.305	25.0	1.20 ± 0.03
RHO_0T7	3.1 (5)	462	84.2	0.201	28.2	0.80 ± 0.03
RHO_0.5T6	4.2 (5)	726	81.8	0.308	26.7	1.17 ± 0.02
RHO_0.25T8	4.2 (5)	689	80.5	0.287	25.7	1.18 ± 0.02
MFI_15	14.0 (15)	233	76.4	0.184	31.5	7.70 ± 0.24
MFI_25	31.6 (25)	360	58.1	0.268	29.8	0.38 ± 0.01
γ-Al_2O_3	-	142	1.5	0.000	106	-

[a] Determined from EDS.
[b] Surface areas were calculated using the BET method, with a standard error of ± 2
[c] Calculated by the t-plot method.
[d] Volume obtained from N_2 adsorption-desorption isotherms.
[e] Estimated by SEM images, with standard error

Figure 31 displays the temperature-programmed desorption (TPD) profile of NH_3, while Table 5 presents the quantitative results for weak, moderate, and strong acid sites. The analysis of Figure 31 reveals prominent peaks for different samples (except MFI_25) within the temperature range of 187 – 201 ℃ and 425 – 528 ℃, indicating the presence of weak and medium/strong acid sites, respectively [86]. Comparing the measured total acid sites reveals that the RHO zeolites, prepared using a template, possess at least 466 μmol g^{-1} more active sites than the MFI type. This property makes them highly desirable as solid acid catalysts. Furthermore, among the RHO zeolites, namely RHO_0.25T8, RHO_0.5T8, and RHO_0.5T10, those exhibiting a higher level of crystallization in XRD analysis demonstrated a greater capacity for NH_3 adsorption. Additionally, the RHO_0.5T10 sample displayed the highest amount of strong acidity, which is crucial for low-temperature methanol conversion. As the amount of template used in synthesis increases, the acidity slightly increases.

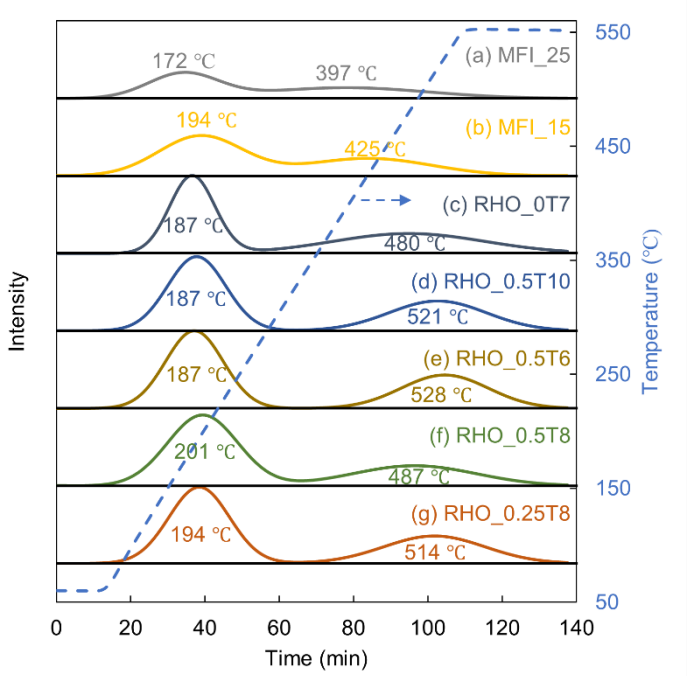

Figure 31. The NH_3-TPD profile of activated zeolites including (a) MFI_25, (b) MFI_15, (c) RHO_0T7, (d) RHO_0.5T10, (e) RHO_0.5T6, (f) RHO_0.5T8, (g) RHO_0.25T8.

Table 5. Numerical result of NH_3-TPD analysis for acidity measurement

Sample	Weak (μmol g^{-1})	T^a_{weak} (°C)	Strong (μmol g^{-1})	T^a_{strong} (°C)	Total (μmol g^{-1})	Weak/Strong (WS ratio)
RHO_0T7	1237.5	187	1048.2	480	2285.7	1.18
RHO_0.25T8	1596.2	194	957.2	514	2553.4	1.67
RHO_0.5T8	1779.9	201	883.5	487	2663.4	2.01
RHO_0.5T6	1460.0	187	948.6	528	2408.6	1.54
RHO_0.5T10	1533.1	187	1028.3	521	2561.4	1.49
MFI_15	1167.7	194	774.7	425	1942.4	1.51
MFI_25	643.8	172	663.9	397	1307.7	0.97

a Temperature of maximum recorded desorption of NH_3.

4.4.2 Catalytic activity

4.4.2.1 RHO zeolites with different amounts of template

RHO zeolite activity will be discussed in this section as a function of template amount. The methanol conversion rate as a function of temperature is shown in Figure 32, for RHO zeolites with different template quantities, γ-Al_2O_3 (a widely used industrial catalyst), and SAPO-34. A

temperature range of 130 °C to 220 °C was chosen to provide insight into methanol dehydration catalysis at low temperatures.

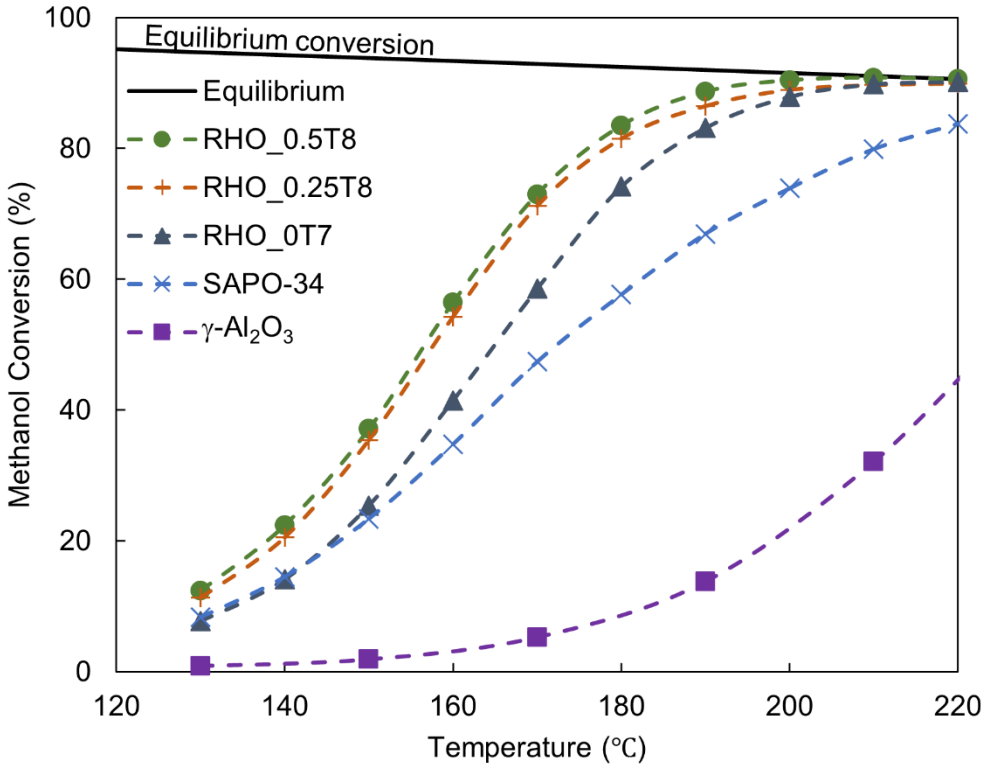

Figure 32. Methanol dehydration at various temperatures using (●) RHO_0.5T8, (+) RHO_0.25T8, (▲) RHO_0T7, (×) SAPO-34, and (■) γ-Al_2O_3 catalysts with WHSV = 4 h^{-1}.

At the lowest temperature of 130 °C, conversions below 10% were recorded for RHO_0T7, γ-Al_2O_3, and SAPO-34, while the RHO zeolites with templates exhibited approximately 13% conversion under the same conditions. Generally, the methanol conversion increased with increasing temperature until thermodynamic equilibrium was reached. The equilibrium conversion of 87% for alumina required a minimum temperature of 290 °C. The structure of γ-Al_2O_3 enabled the presence of Lewis acid sites, which involve the capability of Al^+ to accept electrons. Additionally, the Si-O-Al correlation in zeolites contributed to the creation of Bronsted acid sites (OH^+) as well as Lewis acid sites [172,173]. Notably, water molecules displayed stronger adsorption on Lewis acid sites than Bronsted ones, resulting in catalyst poisoning by reducing the active surface area [73]. The combination of this phenomenon with the super hydrophilic properties of γ-Al_2O_3 hinders its activity at low temperatures below 220 °C.

While SAPO-34 initially exhibited high activity (8.3% at 130 ℃), the conversion rate slope was not as steep as for the RHO zeolites. This can be attributed to the rapid initial deactivation of SAPO-34, leading to the loss of active sites and inhibiting a sharp increase in conversion at rising temperatures. In contrast, a noticeable improvement in conversion curves was observed when employing RHO zeolites. Particularly noteworthy is the fact that the template-free RHO sample began with a 7.7% conversion at 130 ℃, but eventually achieved a high conversion rate (equilibrium) of 90.1% at 220 ℃.

According to Figure 32, the catalytic activity of these zeolite samples was in the following order: RHO_0.5T8 > RHO_0.25T8 > RHO_0T8. A similar order was observed for surface area values, which is significant in catalysis. The more considerable differences in surface area resulted in more significant activity variations. In addition, comparing the acidity reported in Table 5 reveals a direct correlation between acid sites and catalytic activity. Utilizing the XRD results depicted in Figure 28 emphasizes the importance of employing templates to attain more highly crystallized zeolites with improved activity.

Moreover, the RHO zeolites investigated in this section showed 100% DME selectivity based on the concentration of compounds detected by the GC analyzer. Offering the thermodynamic conversion at low temperatures without generating by-products highlights RHO-type zeolite as a highly effective catalyst for methanol dehydration. These findings contribute significantly to the advancement of sustainable energy solutions by promoting the utilization of efficient catalysts in DME production from renewable sources.

The inclusion of templates in RHO synthesis positively impacts the reaction performance. It enhanced accessible acid sites, the degree of crystallization, and specific surface area, and consequently optimized DME production efficiency. The influence of crystallization duration on the selected sample (RHO_0.5T8) will be addressed in the next section.

4.4.2.2 RHO zeolites with varying hydrothermal processing time

This section discusses the influence of crystallization time on the activity of RHO zeolites for methanol dehydration. The zeolite with a complete template exhibited superior activity compared to other samples and was prepared by varying the hydrothermal processing time. Additionally, the results will be compared to the two reference MFI zeolites (MFI_15 and MFI_25).

Figure 33 illustrates the conversion curves for the RHO and MFI samples. For the MFI samples, MFI_25 and MFI_15 reached equilibrium at 220 ℃ and 210 ℃, respectively. The enhanced performance of MFI_15 can be attributed to its lower Si/Al ratio, resulting in higher acidity as presented in Table 5 [145].

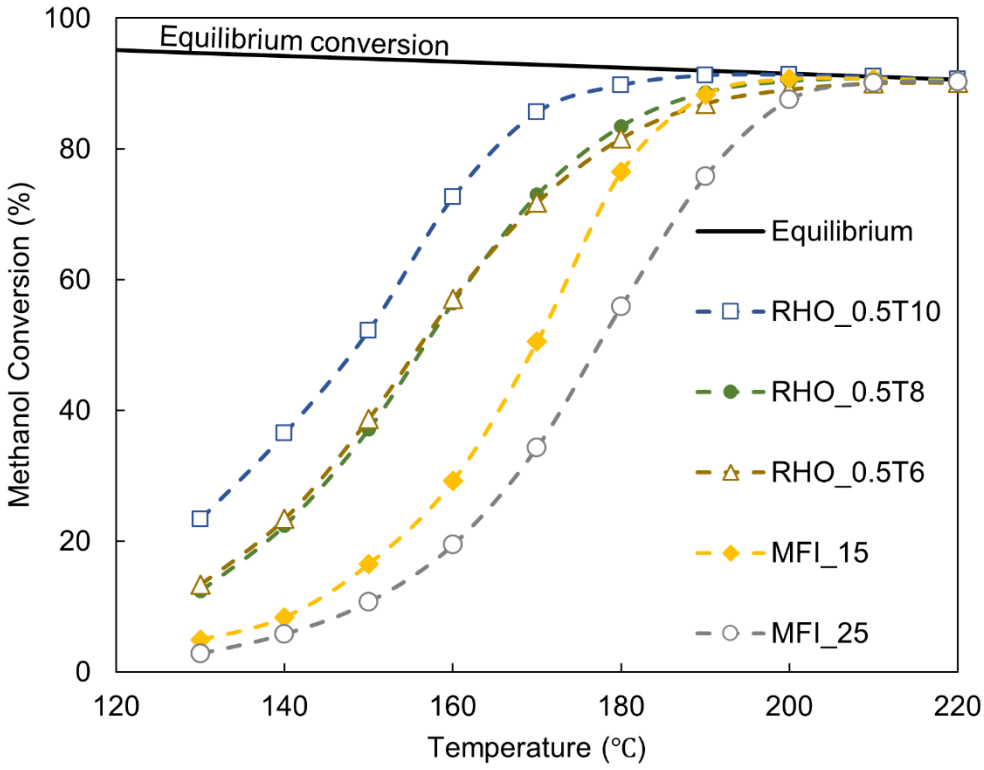

Figure 33. The activity of (□) RHO_0.5T10, (●) RHO_0.5T8, (△) RHO_0.5T6, (◆) MFI_15, and (○) MFI_25 zeolites in methanol dehydration reaction versus temperature with WHSV = 4 h^{-1}.

On the other hand, the activity for methanol dehydration was improved by using RHO zeolites, particularly at low temperatures (≤ 170 ℃). This improvement was accompanied by 100% selectivity towards dimethyl ether (DME), highlighting the effectiveness of different zeolite types in methanol conversion and the resulting product. It is noteworthy that the DME selectivity was 100% for all zeolite samples at 130 – 220 ℃. While the slope for RHO samples was steeper than that of MFI_15 between 130 ℃ and 160 ℃, the opposite trend was observed between 160 ℃ and 190 ℃, with faster conversion growth for MFI_15. A similar trend was observed for SAPO-34, which can be attributed to rapid coke deposition during the initial hours, resulting in active site loss. The amount of coke deposited on the catalyst follows equation 8, where C, C_∞, and τ represent

the coke amount at time t, maximum coke formation, and characteristic time, respectively [72]. A potential cause of the smaller slope between 160 ℃ and 190 ℃ could be the deposition of coke due to the higher acidity of RHO zeolites. However, due to the presence of a high amount of weak and moderate acid sites, the catalysts continued to exhibit activity even after coke formation.

$$C = C_{\infty} \times (1 - e^{-\frac{t}{\tau}}) \quad (8)$$

The methanol conversion over samples with different processing times followed the order of RHO_0.5T10 > RHO_0.5T8 > RHO_0.5T6, demonstrating a direct correlation between synthesis time and catalytic activity. Conversion rates of 91.2% and 91.3% were achieved using a sample prepared with a full template and 10 days of crystallization at 190 ℃ and 200 ℃, respectively. These results indicate that equilibrium conversion was attained at approximately 195 ℃, which is highly desirable for methanol dehydration. The significant increase in conversion over MFI_15 resulted in higher activity compared to RHO_0.5T6 at temperatures above 190 ℃. However, RHO_0.5T10 consistently exhibited superior activity to MFI_15 across all temperature ranges. This suggests that although a longer crystallization time reduced the surface area, it resulted in a more suitable moderate W/S ratio, higher level of crystallinity (Figure 53), and a more stable structure with improved accessibility to active sites for the methanol-to-DME reaction.

Furthermore, the turnover frequency (TOF) was determined for RHO and MFI zeolites using equation 9, which takes into account various factors. In this equation, 'n', 'x', 'AS', and 'm' denote the methanol flow rate (mol h^{-1}), methanol conversion ([]), total acid sites (mol g^{-1}) measured by NH_3-TPD, and the weight of the catalyst loaded in the reactor, respectively. The TOF values were depicted in Figure 34 at 130 – 170 ℃ for different catalysts. Since the methanol dehydration is a thermodynamic limited reaction, providing the TOF at higher temperatures is not useful for comparison. Based on the calculated TOF values at 170 ℃, the catalysts were ranked as follows: RHO_0.5T10 (45.3 h^{-1}) > RHO_0.5T6 (40.3 h^{-1}) ~ RHO_0.5T8 (39.4 h^{-1}) > MFI_25 (32.8 h^{-1}) ~ MFI_15 (32.5 h^{-1}). These results clearly demonstrate that the optimum catalyst (RHO_0.5T10) exhibited significantly higher acid site activity than the other prepared samples, which confirm: (1) RHO zeolites is a more suitable catalyst for this reaction, (2) increasing crystallization time to 10 days has a beneficial effect on catalytic activity.

$$TOF = \frac{n_{methanol} \times x_{methanol}}{AS_{totsl} m_{cat}} \quad (9)$$

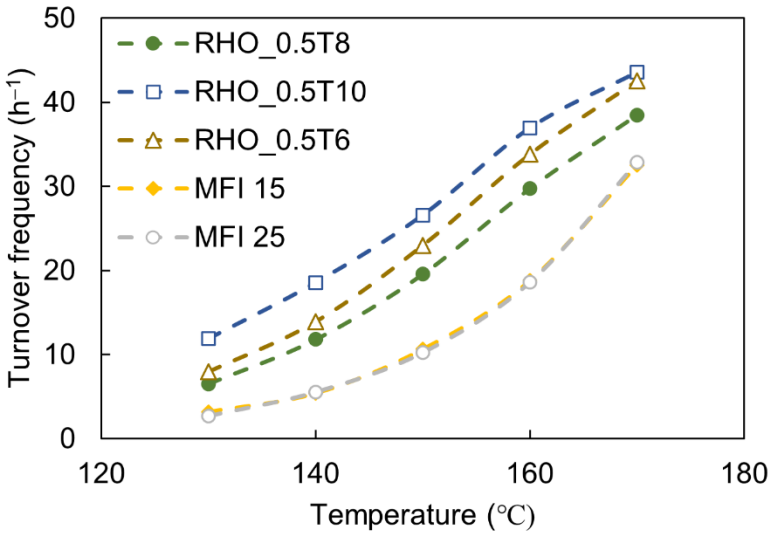

Figure 34. Turnover frequency (h^{-1}) for RHO-type zeolites with different crystallization times and reference MFI zeolites

In summary, the characterization analyses demonstrated the impact of crystallization time on surface area, crystallinity, acid sites, and W/S ratio. The longer duration of crystallization had a positive effect on the methanol conversion to DME process.

4.4.2.3 Stability Tests

This section aims to compare the stability of the optimized RHO zeolite (RHO_0.5T10) with that of the MFI zeolites during a continuous 100 h methanol conversion reaction. It involves analyzing spent catalysts through SEM and TGA techniques. The long-term stability of a catalyst is a crucial factor in assessing its viability for large-scale production.

Zeolites, due to the presence of strong acid sites, are prone to rapid deactivation caused by coke deposition [128]. However, different zeolite types exhibit varying rates of coke formation, which ultimately affect the catalyst's lifetime. Figure 35 demonstrates the long-term DME production over RHO and MFI zeolites. Based on the conversion in the first 10 h of reaction, a straight line was drawn to assess the reduction in activity. Among them, MFI_25 exhibited the least stability, lasting only 20 h. This highlights the significance of preparation methods in process yield. Conversely, MFI_15 maintained its conversion for approximately 60 h, similar to its initial conversion. The abundance of weak acid sites, which are not active in heavy hydrocarbon production, likely enabled MFI_15 to sustain methanol conversion roughly three times longer than

MFI_25. In the case of MFI_25, particle agglomeration was observed in Figure 36, significantly contributing to the loss of activity. However, fresh and spent RHO_0.5T10 exhibited the same morphology and particle size.

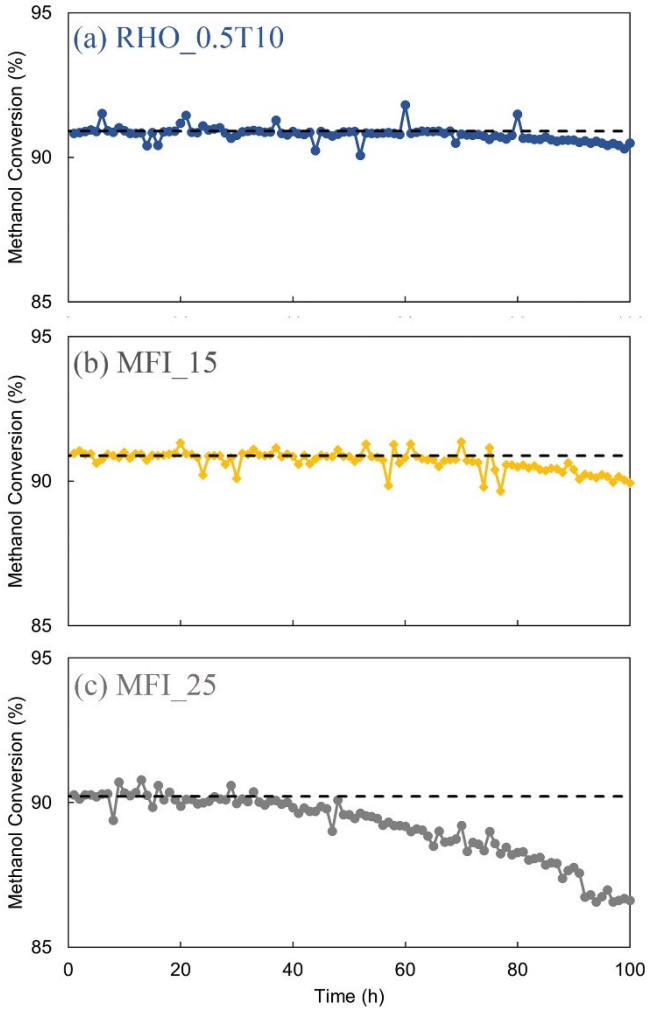

Figure 35. The conversion of methanol using (a) RHO_0.5T10, (b) MFI_15, (c) MFI_25, at their optimum temperatures for 100 h continuous reaction with WHSV = 4 h^{-1} (dash lines = conversion average over first 10 h)

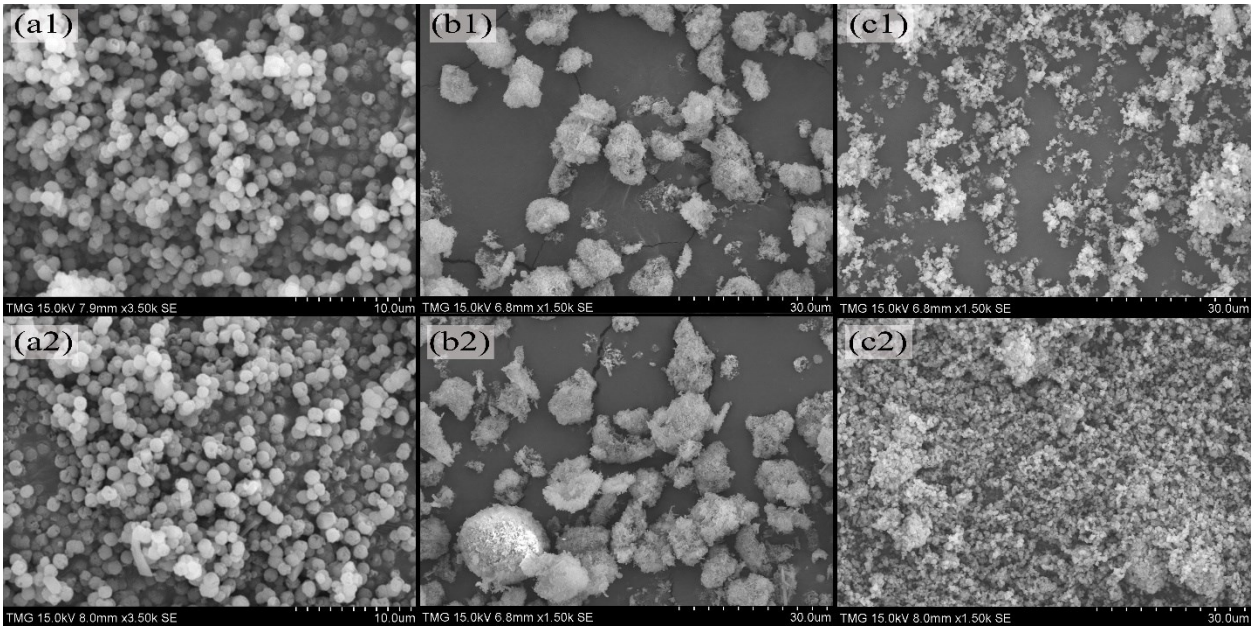

Figure 36. SEM images of used catalysts before and after 100 h reaction including (a1) fresh KFI_1T7, (a2) used KFI_1T7, (b1) fresh MFI_15, (b2) used MFI_15, (c1) fresh MFI_25, (c2) used MFI_25.

RHO_0.5T10 displayed excellent performance in long-term DME production, with less than 0.5% activity loss over 100 h. Based on the TGA/DTA tests illustrated in Figure 37, the rate of coke deposition on the surface was estimated at 0.33 $mg_{coke}\ g_{dry\_cat}^{-1}\ h^{-1}$, 0.25 $mg_{coke}\ g_{dry\_cat}^{-1}\ h^{-1}$, and 0.76 $mg_{coke}\ g_{dry\_cat}^{-1}\ h^{-1}$ for MFI_15, MFI_25, and RHO_0.5T10, respectively. Weight loss below 200 ℃ was attributed to the desorption of methanol and water from the surface. The weight loss between 200 ℃ and 600 ℃ was assumed to be caused by coke desorption or burning. The pause of the temperature programmed ramp to maintain temperatures at 200 ℃ and 600 ℃ ensured complete drying and prevented catalyst structure deformation before burning off the coke.

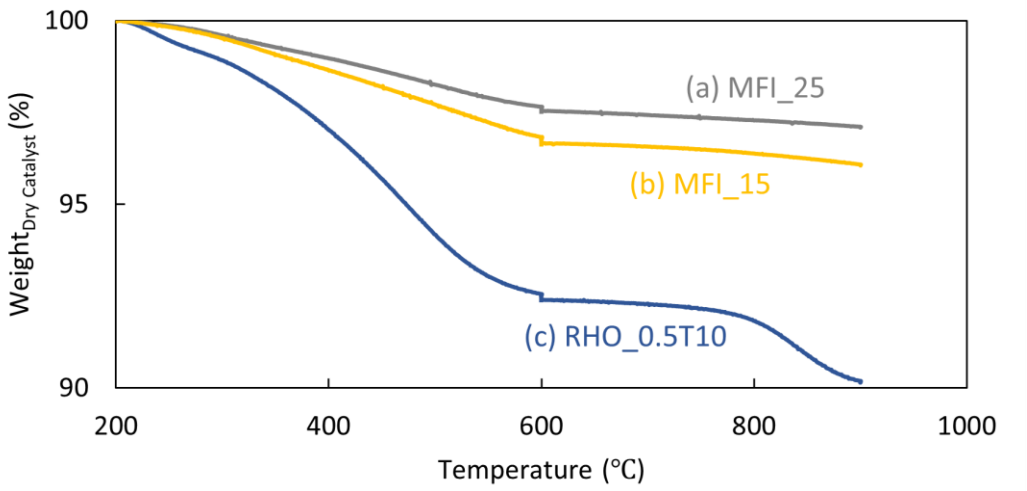

Figure 37. TGA pattern recorded using (a) MFI_25, (b) MFI_15, (c) RHO_0.5T10 catalyst after 100 h reaction.

Figure 38 illustrates Bronsted and Lewis acid sites investigated using DRIFTS analysis. Upon saturating the samples with acetonitrile, three distinct peaks appeared in the IR spectra at wavenumbers 2240 cm^{-1} and 2340 cm^{-1}. The peak at approximately 2298 cm^{-1} can be attributed to the acetonitrile CN group bonded to OH groups (indicative of strong Bronsted acid sites) [174]. Another peak at a higher wavenumber (~2316 cm^{-1}) corresponds to Lewis acid sites. The intensity recorded at 2275 – 2280 cm^{-1} is associated with terminal SiOH groups can be considered as weak Bronsted acid sites. The estimated ratio of Lewis to strong Bronsted acid sites based on the surface area under the mentioned peaks was in the following order: RHO (1.69) > MFI_15 (1.29) > MFI_25 (1.18).

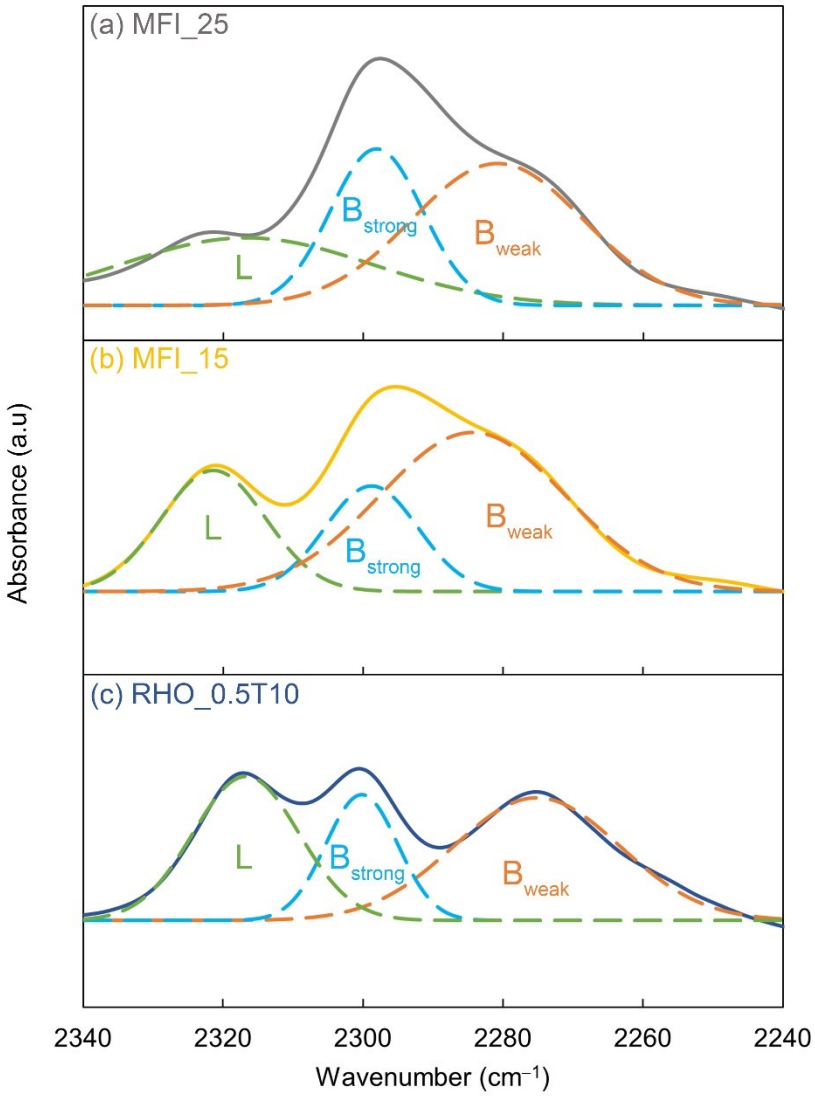

Figure 38. The assessment of Bronsted and Lewis types acidity of saturated samples with acetonitrile by FT-IR spectra (recorded spectra = black lines, peaks deconvolution: colorful lines): (a) MFI_25, (b) MFI_15, (c) RHO_0.5T10.

Furthermore, Figure 39 presents an analysis of coke deposition on samples after a long-term reaction. The presence of pentamethyl benzene ($C_{11}H_{16}$) and hexamethyl benzene ($C_{12}H_{18}$) was detected for MFI zeolites, whereas RHO_0.5T10 showed selectivity only for $C_{12}H_{18}$. The higher coke formation rate and selectivity to heavier hydrocarbons in RHO zeolite can be attributed to the presence of some strong acid sites. The temperature of the NH_3-TPD test for strong acid sites was 521 °C, 425 °C, and 397 °C for RHO_0.5T10, MFI_15, and MFI_25, respectively, which correlates well with the coke analysis results.

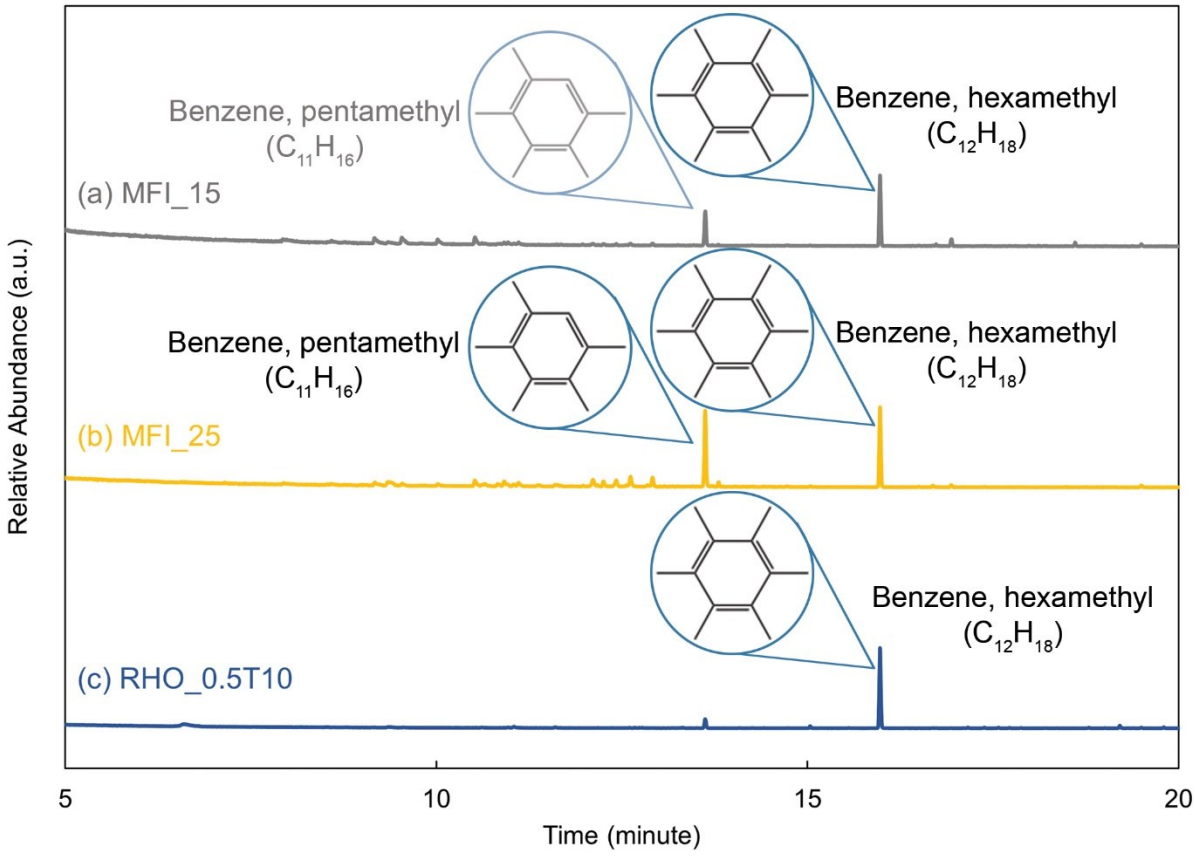

Figure 39. The composition of coke deposited on different zeolite types including (a) MFI_25, (b) MFI_25, (c) RHO_0.5T10 after 100 h reaction using dichloromethane.

The higher activity and stability of the RHO zeolite was expected since its structure possesses a substantial number of strong acid sites. Nonetheless, due to its high W/S ratio, large surface area, high L/B ratio. and excellent crystallization, RHO catalysts demonstrated favorable DME production and selectivity throughout the 100 h process. The significance of this study's findings on DME production becomes evident when taking into account the maximum stability of 60 h observed in other zeolite types with less activity [72,175].

The noteworthy results obtained from the activity and stability tests underscore the significant potential of the synthesized RHO zeolite, prepared using the provided method, for cost-effective and sustainable DME production. In the synthesis of DME, this zeolite has the potential to reduce catalyst costs by enabling long processes without sacrificing activity or selectivity.

4.5 Conclusions

In the pursuit of a sustainable energy source, DME emerges as a significant candidate. This study investigated the potential of nine distinct solid acid catalysts for efficient DME production at a WHSV (Weight Hourly Space Velocity) of 4 h^{-1}. The catalysts examined included a commercial γ-Al_2O_3, two MFI (ZSM-5) zeolites with Si/Al ratios of 15 and 25, and six synthesized RHO zeolites.

The RHO zeolites were prepared using three different templates, with T/Al_2 ratios of 0, 0.25, and 0.5 under various crystallization times of 6, 8, and 10 days. Characterization analyses, such as SEM and XRD, highlighted the significance of the template's presence in achieving well-crystallized and uniform zeolites. Moreover, N_2 adsorption/desorption and BET analyses estimated the surface area to be greater than 671 m^2 g^{-1} for samples with templates. NH_3-TPD and DRIFTS tests revealed that RHO-type zeolites exhibited higher acidity strength and L/B ratio than MFI-type zeolites. Additionally, preparation parameters affected weak to strong acid content ratios.

The activity experiments, focusing on methanol to DME conversion, demonstrated that RHO zeolites exhibited superior performance to MFI and γ-Al_2O_3. Among the RHO zeolites, RHO_0.5T10, with a total acidity of 2561 μmol g^{-1}, a weak/strong acid ratio of 1.49, and the highest degree of crystallization, achieved equilibrium conversion at approximately 190 °C with 100% selectivity and remarkable stability for over 70 h. The synthesized RHO zeolite reduced equilibrium conversion temperature and increased continuous reaction duration, demonstrating significant progress in DME production by saving process costs.

CHAPTER 5: THE EFFECT OF TEMPLATE AND CRYSTALLIZATION TIME ON KFI-TYPE ZEOLITE ACTIVITY FOR METHANOL DEHYDRATION TO DME

5.1 Abstract

Renewable energy plays a crucial role in addressing air pollution, particularly due to the substantial contribution of fossil fuels to transportation. DME as a renewable energy source showed the capability to reduce CO, SOx, and NOx emissions when used in vehicles, fuel cells, and households. This study assessed the catalytic effectiveness of KFI-type zeolites for methanol dehydration to DME, compared with (MFI) ZSM-5 and γ-Al_2O_3 catalysts. The template molar concentration and crystallization time were varied to examine their influence on zeolites' properties. Structural characterization techniques including XRD, SEM, BET, DRIFTS, NH3-TPD, and TGA were employed to assess the impact of preparation parameters. Activity and stability tests revealed the superior performance of KFI zeolites synthesized with a Si:template ratio of 10:1 and 7 days of hydrothermal crystallization. As a result of its high acidity of 2466 μmol g^{-1}, the catalyst exhibited thermodynamic conversion at 180 ℃ and maintained activity for > 100 h due to its mesoporous structure. These findings underscore the potential of KFI-type zeolites as efficient DME production catalysts.

5.2 Introduction

In response to growing air pollution, global warming, and other environmental issues, scientists are exploring effective solutions for society to maintain their standards of modern living without harming the environment. Substituting fossil fuels that contribute substantially to air pollution problems with renewable energy sources is an effective way to alleviate air pollution problems [176]. Over the last decades, dimethyl ether (DME) has gained considerable attention for its potential energy applications [177]. The physical and chemical characteristics of DME make it an attractive candidate for a future energy source. This is due to the high cetane number (55-60), the high oxygen content (34.8% by mass), the absence of a C–C bond, and the low emissions of carbon monoxide (CO) and nitrogen oxides (NO_x) during combustion [178,179]. Furthermore, DME fuel is compatible with current infrastructures for LPG and diesel fuels, which is another advantage over other renewable energy sources. DME can be produced from the CO/CO_2 mixture obtained

through biomass gasification, CO_2 capture, and waste, making it an environmentally friendly and sustainable fuel. [180,181].

The production of DME can be accomplished via a direct process with $CO/CO_2/H_2$ as input or through an indirect process with methanol as input, both of which require a solid acid catalyst to facilitate the methanol dehydration reaction. Although γ-Al_2O_3 has been the conventional solid acid catalyst for methanol dehydration in industrial scales, it has two major drawbacks: 1) it requires high temperatures to reach equilibrium thermodynamic conversion, and 2) poisoning due to strong water molecules adsorption due to its hydrophilic properties [80,182]. Huber et al. demonstrated that Lewis acid sites adsorb water stronger than Bronsted acid sites by 57 kJ $mole^{-1}$, which helps explain why alumina composed of Lewis acid sites is susceptible to water poisoning. [73].

As a result, certain compounds such as heteropoly acids (HPA) and zeolites have found their way into this process during the last two decades since they possess higher acidity strength and are made up of both Lewis and Bronsted acid sites. Even though HPAs have high acidity strength (strong Bronsted acid sites) which is desirable for methanol dehydration, their low surface area (<10 m^2 g^{-1}) is a critical barrier to high activity and stability [183].

In addition to having a wide range of structures and porosities, high surface area, Bronsted and Lewis acid sites, and chemical and thermal resistance allow zeolites to be widely used in a wide range of applications, specifically in catalytic activity for fuel production [184,185]. The MFI (ZSM-5) zeolite is the most common zeolite type used for DME production and showed superior activity against the γ-Al_2O_3 at low temperatures (< 250 °C) [82]. On the other hand, zeolites are highly acidic, which results in the formation of coke and byproducts, which lead to catalyst deactivation [186]. Fr example, Migliori et al. investigated the catalytic activity of MOR, FER, and MFI catalysts and found that the MOR sample, with the highest acidity (1034 μmol g^{-1}) initially exhibited excellent activity (~87% at 220 °C), but its performance degraded within 5 h [72]. Similarly, Y zeolites with a high acidity of 2150 μmol g^{-1} demonstrated stability for less than 10 h in methanol conversion [187]. Another study by Catizzone et al. compared the coke deposition and deactivation rates of Beta zeolite (BEA), MFI, and FER, revealing that BEA showed the highest coke deposition (>60 mg_{coke} $g_{catalyst}^{-1}$) and rapid deactivation [188]. Therefore, while

acidity plays a crucial role in methanol dehydration, it needs to be carefully balanced with other catalyst properties to achieve optimal activity.

Furthermore, factors such as porosity topology, crystal size, and the ratio of strong acid sites to total acidity significantly impact the catalyst's performance and lifetime [189]. A research conducted by Rownaghi et al. evaluated three MFI zeolites with crystal sizes of 1.2, 0.3, and 0.12 μm and results indicated the beneficial effects of smaller crystal size (nanoscale) for facilitating the methanol conversion process [122]. Even though all three catalysts had similar total acid density, 19 % and 16 % enhancement were observed for methanol dehydration and DME selectivity, respectively, changing from micro-scale to nano-sized crystals. Additionally, a similar trend was reported by Catizzonea et al. for FER-type zeolite where nanosized FER (0.3-0.5 μm) and microsized FER (5-10 μm) provided methanol conversion of ~87% and ~73% at 220 ℃, respectively [78]. Also, Catizzone et al. scrutinized two zeolites with a 3-D framework, including BEA and MFI, and a 2-D zeolite, FER-type [188]. In the case of BEA and MFI zeolites, equilibrium was reached at 260 ℃ and 270 ℃, respectively, while for FER, temperatures over 300 ℃ were required. However, the 2-D FER zeolite showed 100% DME selectivity at high temperatures (300 ℃) and exhibited longer stability.

In addition, alkali treatment (desilication) through ion exchange in NaOH solution, has been investigated to create mesoporous structures and improve catalytic activity and stability [190]. Rutkowska et al. performed alkali treatment on MFI zeolites for 1, 2, and 4 h, and they observed that the MFI zeolite treated for 2 h achieved 83% conversion whereas the unmodified zeolite only provided 49% methanol conversion at 200 ℃. Similarly, Aloise et al. demonstrated that a 1-hour alkaline treatment on MFI significantly increased the mesoporosity volume from 0.089 ($cm^3\ g^{-1}$) to 0.185 ($cm^3\ g^{-1}$) [191]. This structure modification enhanced the methanol conversion at 200 ℃ from 75% to 83% and sustained the DME selectivity for 80 h. However, even with the modified MFI catalysts, high temperatures (>225 ℃) were still required to achieve equilibrium conversion.

Recent studies have placed emphasis on synthesizing zeolites with tailored properties to enable thermodynamic conversion of methanol at lower temperatures while maintaining high DME selectivity. For instance, Masih et al. assessed the performance of KFI and RHO zeolites for methanol dehydration at temperatures ranging from 150 – 200 ℃ [121]. The RHO type indicated the equilibrium methanol conversion at 200 ℃ and maintained the activity for 25 h at a low WHSV

of 1 h^{-1}. Aside from that, there is evidence to suggest that different preparation parameters, such as the type and amount of template (structure directing agent) and crystallization duration, have substantial impacts on the chemical and physical properties of synthesized zeolite [192,193].

In this experimental work, the performance of lab-prepared KFI zeolites with a Si/Al ratio of 5 (~4.3), as well as two commercial (MFI) ZSM-5 zeolites with Si/Al ratios of 15 and 25, and a commercial γ-Al_2O_3 catalyst were studied for DME production via methanol dehydration, employing a WHSV of 4 h^{-1}. To the best of our knowledge, this is the first investigation into the effect of the template and hydrothermal processing time on KFI zeolite performance for DME formation. The results obtained using KFI with Si:Al:T (T = template) ratio of 10:2:1 (molar ratios) and a hydrothermal processing time of 7 days demonstrated the highest activity and stability for methanol dehydration in the temperature range of 130 – 220 ℃. These findings shed light on the potential of tailored KFI zeolites as promising catalysts for efficient DME synthesis.

5.3 Experimental

5.3.1 Catalyst preparation

The commercial MFI (ZSM-5) zeolite with Si/Al = 15 (referred to as MFI_15) provided by Clarient Co., the commercial MFI with Si/Al = 25 (referred to as MFI_25) purchased from Alfa Aesar, and the γ-Al_2O_3 catalyst purchased from Alfa Aesar were employed as reference catalysts for DME production to assess the synthesized KFI catalysts.

The KFI zeolites were prepared using a hydrothermal crystallization process based on a previously reported procedure [168]. The materials used in this study for the synthesis and activation of zeolites included potassium hydroxide (KOH, 85%, ACP chemicals), aluminum hydroxide ($Al(OH)_3$, extra pure, Thermo Scientific), 18-Crown-6 ($[C_2H_4O]_6$, 99%, Thermo Scientific), strontium chloride hexahydrate ($SrCl_2.6H_2O$, 99%, Alfa Aesar), colloidal silica (SiO_2, 40 w% solutions in water, LUDOX AS-4O, Sigma Aldrich), sodium hydroxide (NaOH, 97%, ACP chemicals), and ammonium chloride (NH_4Cl, 99.5%, Sigma Aldrich).

Initially, three KFI catalysts were synthesized with different Si:T ratios including 10:1, 10:0.5, and 10:0, using a 5-days hydrothermal reactor process. In the next step, the selected catalyst was reproduced with 3, 5, and 7 days of hydrothermal processing time. For the synthesis of KFI (Si/Al

= 5) with a Si:T ratio of 10:1, solution A was prepared under stirring from 1.00 g of KOH, 2.33 g of deionized water, and 0.52 g of $Al(OH)_3$ powder. Once $Al(OH)_3$ was added, the temperature was raised to the boiling point until a clear solution was obtained. The solution was then cooled, weighed to correct for weight loss, and mixed with solution B, which contained 0.90 g of 18-C-6 (18-Crown-6), 0.09 g of $SrCl_2.6H_2O$, and 3.97 g of deionized water. Next, 5 g of silica source was added dropwise to the combined solution while stirring. After 30 minutes of stirring, the final gel with a composition of $2.3K_2O$:$1.0Al_2O_3$:0.1SrO:1.0(18-C-6):$10SiO_2$:$160H_2O$ was transferred into a PTFE lined stainless steel hydrothermal reactor (Parr Instruments Acid Digestion Vessel 45 mL), and subjected to crystallization under autogenous pressure at 150 ℃ for 5 days (Thermo Scientific™ Heratherm™ General Protocol Oven). The resulting mixture was then filtered and washed until it the filtrate reached a neutral pH, and the solid was dried overnight at 60 ℃ for 10 h. Afterward, the dried zeolite was calcined at 600 ℃ for 3 h to remove 18-Crown-6 from the structure (Thermo Scientific™ Thermolyne™ Muffle Furnace). The same procedure was followed with half the amount of 18-Crown-6 to synthesize KFI zeolites with a Si:T ratio of 10:0.5.

A slightly different method was employed to synthesize template-free crystallized KFI zeolites. Solution A was similar to the previous methods and contained deionized water, KOH, and $Al(OH)_3$. In a separate beaker, solution B was prepared by dissolving $SrCl_2.6H_2O$ in water, followed by the dropwise addition of LUDOX AS4O while vigorously stirring for a few minutes. The rest of the water was added to the solution and stirred for an additional 6 minutes. The two solutions were then combined by adding solution A to solution B in a PTFE beaker, resulting in a composition of $2.3K_2O$:$1.0Al_2O_3$:0.1SrO:$10SiO_2$:$160H_2O$. The resulting mixture underwent hydrothermal crystallization for 5 days at 150 ℃. The mixture was then washed and filtered until the filtrate reached a neutral pH and the solid was dried overnight at 60 ℃ for 10 h. Finally, the solid was calcined at 600 ℃ for 3 h to stabilize the structure.

To obtain the H-form of zeolites, which is active for methanol dehydration, an ion-exchange was performed with an NH_4Cl solution. The process was completed in 3 cycles while in each step 1 g of zeolites was dissolved in 100 ml of 1 M NH_4Cl solution and stirred for 1.5 h at 80 ℃, followed by filtration and washing with deionized water. Finally, the calcination at 600 ℃ for 5 h was carried out to change NH_4-type to H-type zeolites. The obtained zeolites were labeled as KFI_XTY where X = 1, 0.5, 0 shows the amount of template in the Si/Template ratio, and Y = 3, 5, 7 indicates

the hydrothermal processing duration in days. For example, KFI_1T3 refers to a sample with initial gel composition containing Si/Template ratio of 10:1 with 3 days of crystallization under hydrothermal condition.

5.3.2 Characterization

Powder XRD analysis was performed using Rigaku SmartLab SE X-ray diffractometer with Cu Kα at 40 kV and 44 mA to evaluate if the crystallization process was completed during zeolites preparation. The pattern was collected in the 2θ range between 5° and 80° while the scanning rate was 5° min^{-1}.

In order to study the textural properties including specific surface area and total volumes of micropores and mesopores, the N_2 adsorption was conducted by 3FLEX Surface Characterization (ATS Scientific Inc.) automated gas adsorption system at liquid nitrogen temperature (-196 ℃). Before starting the analysis, samples were degassed for 12 h at 150 ℃. Based on the results of N_2 adsorption, the micropores volumes, the specific surface area, and mesopores volumes were calculated using Harkins and Jura (t-plot analysis), BET (Brunauer–Emmett–Teller), and BJH model (Kruk–Jaroniec–Sayari empirical procedure) models. Standard error was calculated based on standard deviation divided by square root of sample size after performing three BET tests on the KFI_1T7 sample.

Temperature program desorption of ammonia (NH_3-TPD) was performed on a Altamira AMI-300 instrument to measure the samples' surface acidity. Samples were also degassed under pure He flow for 120 min at 300 ℃ before accomplishing the analysis. Upon cooling to 60 ℃, the gas stream was changed to the mixture including 10 vol.% NH_3 and He as carrier gas. The ammonium flow was kept for 1 h, then, the sample was purged with He gas for 60 min to remove the unstable adsorbed NH_3. Finally, the desorption was conducted under the increasing temperature with 5 ℃ min rate and the pattern of ammonium desorption was recorded at 60 – 550 ℃ under the constant flow of helium (10 mL min^{-1}).

Additionally, scanning electron microscopy (SEM) was carried out using a S-3400N HITACHI equipment at 15 kV to study the surface morphology of catalysts and particle size distribution. To prepare samples for SEM, catalysts were mounted on an aluminum slab and gold layer were sputter-coated on the samples. The average particle size was estimated by taking a sample size

containing 50 – 55 individual particles. Also, the Energy dispersive spectroscopy (EDS) was performed to calculate the Si/Al ratio in synthesized and commercial zeolites using the attached Link Pentafet OXFORD instrument.

After performing the methanol conversion over 100 h, the TGA/DTA analysis was performed on a Netzsch TG 209 F1 analyzer to measure the deposited coke on samples. In this regard, the loaded sample in an Al_2O_3 crucible was heated from 25 °C to 900 °C with a ramp rate of 5 °C min^{-1} under the 30 mL min^{-1} flow of air. To ensure the complete drying and burning of coke, the temperatures were maintained at 200 °C and 600 °C for 0.5 h, respectively. The water content of catalysts, determined by weight loss at temperatures ≤ 200 °C, was utilized to adjust the sample mass and present coke formation rate derived from the dried catalyst weight.

To evaluate the coke composition deposited on various zeolite types, the following procedure was employed: 20 mg of spent catalyst (40 mg in case of KFI zeolite) was combined with 5 ml of a 4M KOH solution to digest the zeolite structure. Subsequently, 5 mL of dichloromethane was added to the solution to complete the extraction process. The resulting solution comprising coke was then analyzed using a GC-MS instrument. The investigation was conducted in a temperature range of 50 – 300 °C, with a solvent delay of 3 minutes.

The diffuse reflectance infrared Fourier transform spectroscopy (DRIFTS) test was carried out to study acid types on catalysts. The sample was first dried at 300 °C for 120 minutes under an N_2 stream, and after cooling to room temperature, a N_2 gas flow containing approximately 10 torr of acetonitrile-d3 (CD_3CN) was passed through the dried sample. This process continued for 120 minutes to complete the saturation. Finally, the saturated sample was purged with pure N_2 flow for 120 minutes to desorb unstable acetonitrile-d3 molecules, and the DRIFTS analysis was performed using a Nicolet™ iS50 FTIR instrument equipped with an MCT detector. The spectra were recorded in the 600 – 4000 cm^{-1} wavenumber range with an optical resolution of 4 cm^{-1} at 50 °C.

5.3.3 Catalytic activity

The DME formation process was investigated using a fixed-bed quartz reactor within specified temperature ranges under atmospheric pressure inside an electric furnace. For the zeolite samples, the temperatures ranged from 130 °C to 220 °C, while for γ-Al_2O_3, the temperature range extended

from 130 ℃ to 310 ℃. A gas chromatograph (GC) equipped with an FID detector, with a HP plot Q column (30 m length, 0.32 mm ID), was used to measure both the feed and output gas concentrations from the reactor. Additionally, a K-type thermocouple was employed to measure the temperature of the catalyst at the top of the bed. To prevent methanol condensation, the feed gas was heated to 120 ℃ between the mass flow controller and the reactor.

Each experiment utilized 100 mg of catalyst, which was placed into the reactor. Prior to the reaction, pretreatment procedures were implemented. For γ-Al_2O_3, the catalyst was pretreated at 400 ℃ for 1 hour, while for zeolites, pretreatment was conducted at 500 ℃, both under a pure Ar flow rate of 20 mL min^{-1}. After pretreatment, the reactor was cooled down to 125 ℃, and the gas flow was switched to a mixture of methanol and argon. The liquid methanol was injected into the heated lines (at 120 ℃) by a syringe pump, mixing with the Ar flow (as an inert gas) to achieve a gas composition containing 30 vol.% methanol. The weight hourly space velocity (WHSV) and total flow were adjusted to 4 $g_{MeOH}\ g_{Catalyst}^{-1}\ h^{-1}$ and 22 mL min^{-1}, respectively. Data collection was conducted under steady-state conditions, with product analysis performed every 30 minutes for 3 h at each temperature setpoint.

In order to check reproducibility, the activity test was replicated for the KFI zeolite sample (KFI_1T5) prepared with the full amount of template under 5 days of crystallization time (Figure 67). A comparison of KFI_1T7, MFI_15, and MFI_25 activity for methanol conversion at a specific temperature in two series of tests also confirmed reproducibility.

5.4 Results and discussion

5.4.1 Characterization

The XRD-recorded patterns of synthesized KFI zeolites are depicted in Figure 40. The major picks were observed at 2θ = 9.56°, 20.24°, 21.3°, 23.4°, 27,91°, 29.53°, and 31.84°, which were also observed for activated catalysts indicating no structural changes. These peaks are associated with crystal phases of well-prepared KFI zeolites and in agreement with literature [194]. The effect of the template on the crystallization of catalysts was obvious by comparing the KFI_1T5, KFI_0.5T5, and KFI_0T5, where the synthesized zeolite without template had lower crystallinity than the other two. The influence of this crystallization degree will be studied in the activity

section. The best-produced samples were achieved by complete Si/Template = 10 under a 5- and 7-day synthesis process.

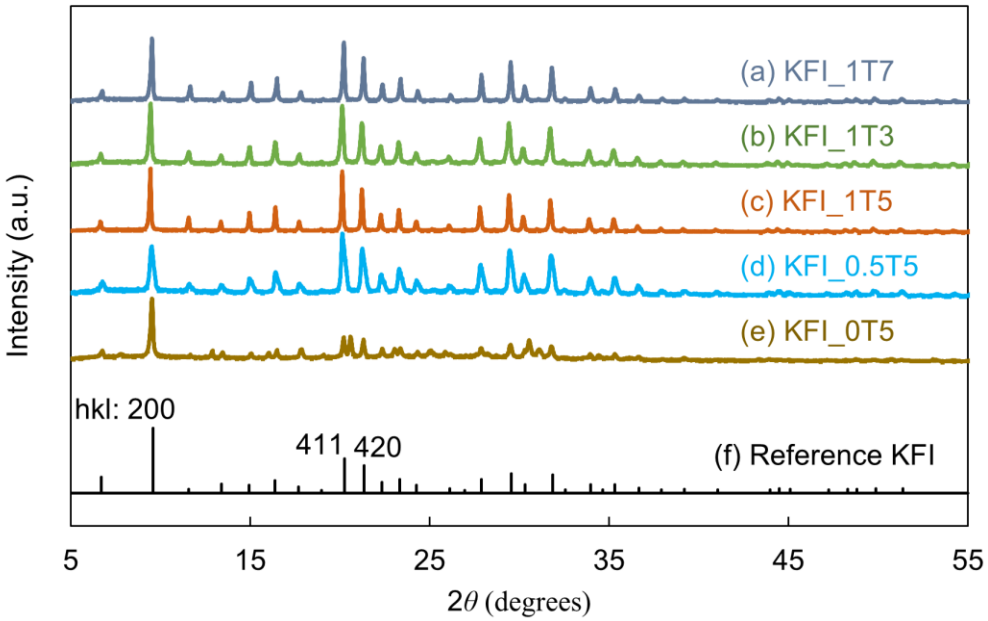

Figure 40. XRD patterns of synthesized KFIs with different template amounts and hydrothermal processing time durations including (a) KFI_1T7, (b) KFI_1T3, (c) KFI_1T5, (d) KFI_0.5T5, (e) KFI_0T5, (f) reference from literature [195].

The SEM images, as depicted in Figure 41, indicated the cube-like morphology of synthesized KFI zeolites and the spherical shape of MFI zeolites. Also, they confirmed the results obtained from XRD analysis which show the successful crystallization process for prepared gel except for the sample without a template (KFI_0T5). Based on the SEM images, the average particle sizes of zeolites were estimated at 1.5 – 1.7 µm, 2 µm, and 3 µm in case of full, half, and no template used, respectively. Therefore, the presence of a template can result in a smaller particle size. The crystal size of 6 µm and 0.49 µm were also measured for MFI_15 and MFI_25 and their effect on catalytic activity will be discussed later.

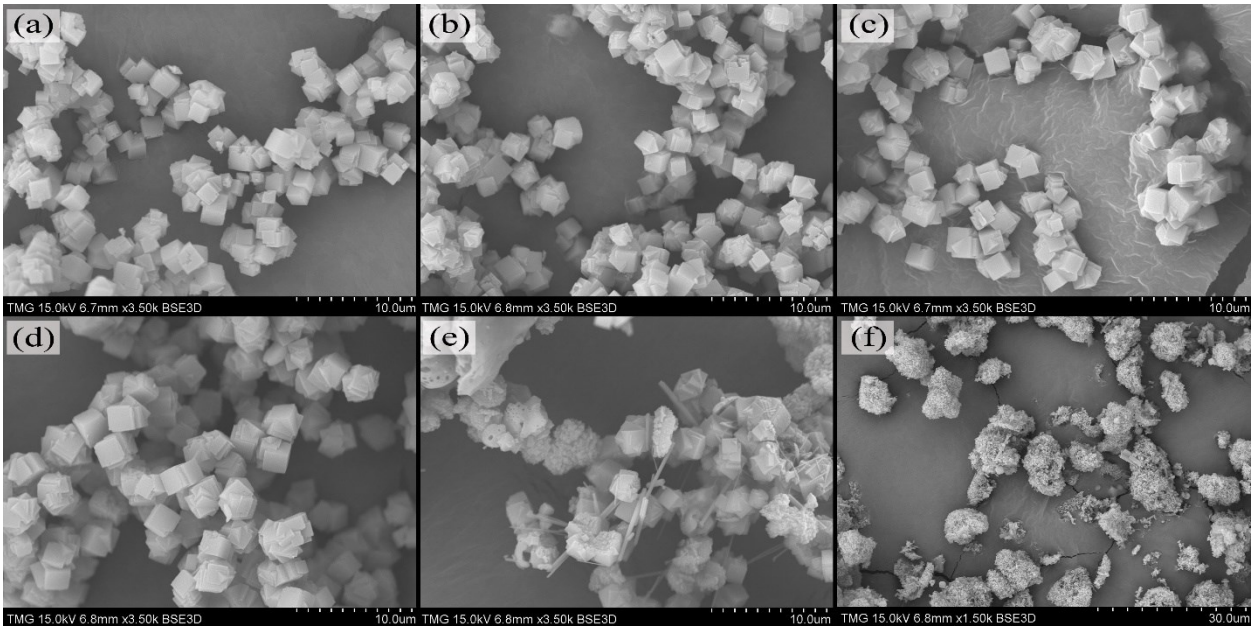

Figure 41. SEM images of synthesized KFIs including (a) KFI_1T7, (b) KFI_1T3, (c) KFI_1T5, (d) KFI_0.5T5, (e) KFI_0T5, (f) MFI_15.

Figure 42 and Figure 43 show the nitrogen adsorption/desorption profile for different prepared catalysts. The observed hysteresis in the KFI_1T7 adsorption/desorption profile, which is similar to the type IV of the IUPAC classification, revealed the presence of mesopores in this sample [196]. Mesopores were also observed in KFI_1T5 and KFI_0.5T5 but at a lower level. Consequently, the higher hydrothermal crystallization time has an impact on the structure of the final zeolite [197]. KFI_1T3 and KFI_0T5 exhibited typical type-I isotherms regarding the IUPAC classification, which implies the microporous nature of these samples [198]. The chemical and physical properties of commercial and prepared catalysts have been summarized in Table 6. The EDS analysis demonstrated that the final obtained catalysts had a Si/Al of 4.3 while the value for the initial gel was 5. However, it shows a great preparation method compared to previous studies which reached Si/Al of 3.3 with the same starting gel composition [121]. The high BET surface area of > 390 m^2 g^{-1} was calculated for samples incorporating the template. The low surface of 205 m^2 g^{-1} for KFI_0T5 revealed the importance of a template for KFI-type zeolite synthesis. A direct correlation was found between surface area and the amount of template or crystallization time. Therefore, the highest surface area of 541 ± 2 m^2 g^{-1} was measured for KFI_1T7. Moreover, a higher BET was observed for MFI_25 which corresponds to the nanosized particle size of this commercial sample. The micropore volume and t-plot method results attributed to KFI_1T3,

KFI_1T5, and KFI_1T7 revealed the positive influence of higher processing time on the development of pores with a higher micro-distribution.

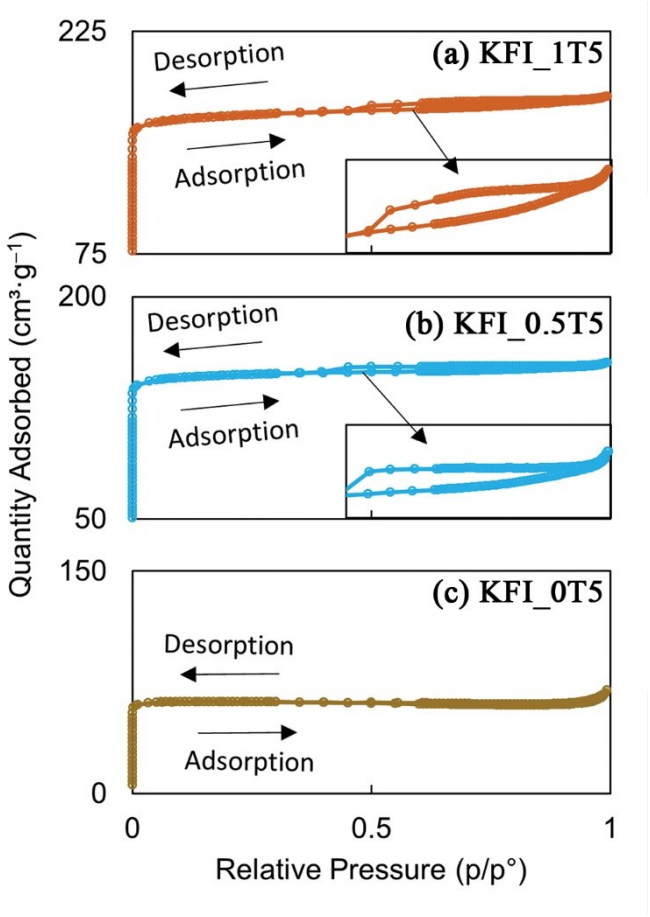

Figure 42. N_2 adsorption–desorption isotherm patterns of (a) KFI_1T5, (b) KFI_0.5T5, (c) KFI_0T5 catalysts.

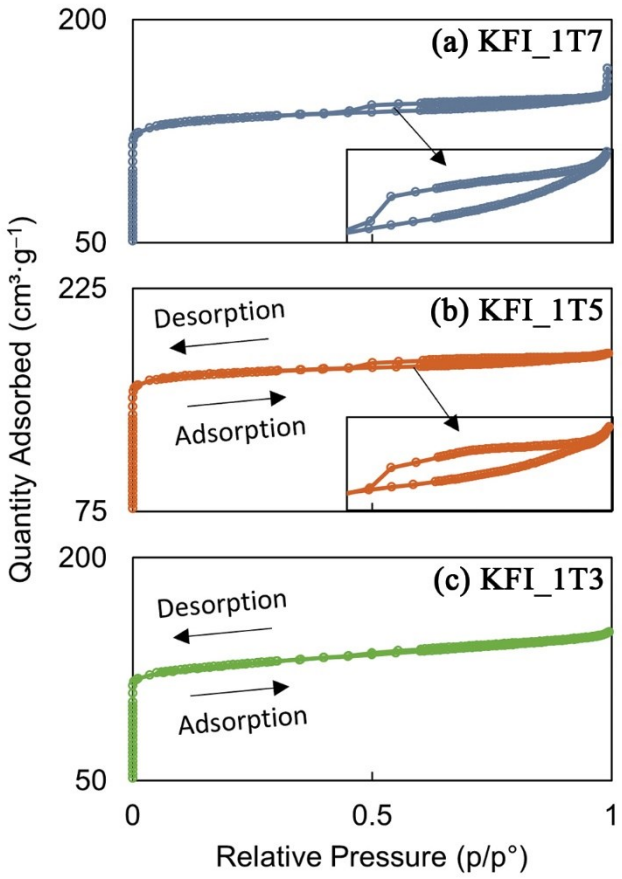

Figure 43. N_2 adsorption/desorption isotherm patterns of KFI with different crystallization times including (a) KFI_1T7, (b) KFI_1T5, (c) KFI_1T3.

Table 6. Chemical and physical properties of investigated catalysts.

Sample	Si/Al ratio [a] of crystal (gel)	S_{BET} [b] ($m^2.g^{-1}$)	Surface area related to micro pores [c] (%)	$V_{micropore}$ [d] ($cm^3.g^{-1}$)	Pore diameter (Å)	Crystal size [e] (µm)
KFI_0T5	4.3 (5)	186	99.0	0.108	23.2	2.44 ± 0.12
KFI_0.5T5	4.3 (5)	445	92.6	0.241	21.7	2.03 ± 0.03
KFI_1T5	4.3 (5)	510	90.8	0.281	22.0	1.77 ± 0.05
KFI_1T3	4.3 (5)	391	81.8	0.232	23.7	1.56 ± 0.05
KFI_1T7	4.3 (5)	541	86.0	0.259	25.4	1.81 ± 0.03
MFI_15	14.0 (15)	233	76.4	0.184	31.5	7.70 ± 0.24
MFI_25	31.6 (25)	360	58.1	0.268	29.8	0.38 ± 0.01
γ-Al_2O_3	-	142	1.5	0.000	106	-

a Determined by EDS.
b Surface areas were calculated using the BET method, with a standard error of ± 2
c Calculated by the t-plot method.
d Volume obtained from N_2 adsorption-desorption isotherms.
e Estimated by SEM images with standard error based on standard deviation divided by the sample size's square root.

The profile from the NH_3-TPD is presented in Figure 44, and the quantitative results for weak, moderate, and strong acid sites were summarized in Table 7. Figure 44 indicates two major peaks at temperatures around 166 – 194 ℃ and 391 – 452 ℃ which are associated with weak and medium/strong acid sites [68]. The lower acid sites of MFI_25 compared to MFI_15 can be attributed to its higher Si/Al ratio. Furthermore, the KFI zeolites exhibited a greater number of acid sites, ranging between 343 and 844 μmol g^{-1} more than MFI_15, demonstrating their potential for increased activity. The Weak/Strong ratio was also calculated to account for the different activity and selectivity toward coke formation among acid sites with varying strengths. Notably, the temperatures corresponding to the recorded peaks (T_{weak} and T_{strong}) in KFI_1T7 were higher than those observed in other synthesized samples, indicating a stronger acid site strength in this sample.

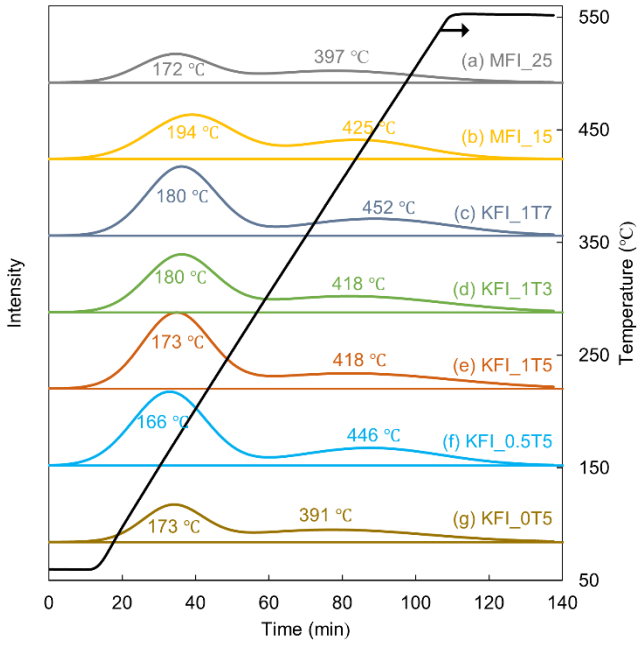

Figure 44. NH_3-TPD pattern of (a) MFI_25, (b) MFI_15, (c) KFI_1T7, (d) KFI_1T3, (e) KFI_1T5, (f) KFI_0.5T5, (g) KFI_0T5 catalysts.

Table 7. The acidity strength of synthesized and commercial zeolites [a]

Sample	Weak (μmol/g)	T^b_{weak} (℃)	Strong (μmol/g)	T^b_{strong} (℃)	Total (μmol/g)	Weak/Strong
KFI_0T5	700.3	173	801.2	391	1501.5	0.87
KFI_0.5T5	1835.7	166	864.3	446	2700.0	2.12
KFI_1T5	1702	173	1084.9	418	2786.9	1.57
KFI_1T3	1265.8	180	1019.5	418	2285.3	1.24
KFI_1T7	1600.9	180	865.2	452	2466.1	1.85
MFI_15	1167.7	194	774.7	425	1942.4	1.51
MFI_25	643.8	172	663.9	397	1307.7	0.97

a Measured using NH_3-TPD.
b Temperature of maximum recorded desorption of NH_3.

5.4.2 Catalytic Activity

5.4.2.1 The effect of template

Figure 45 presents the experimental results of methanol conversion rates obtained using KFI zeolites with varying template quantities and γ-Al_2O_3, commonly employed catalysts in the industry. The investigation covered a temperature range from 130 ℃ to 220 ℃, allowing for a comprehensive understanding of catalytic behavior.

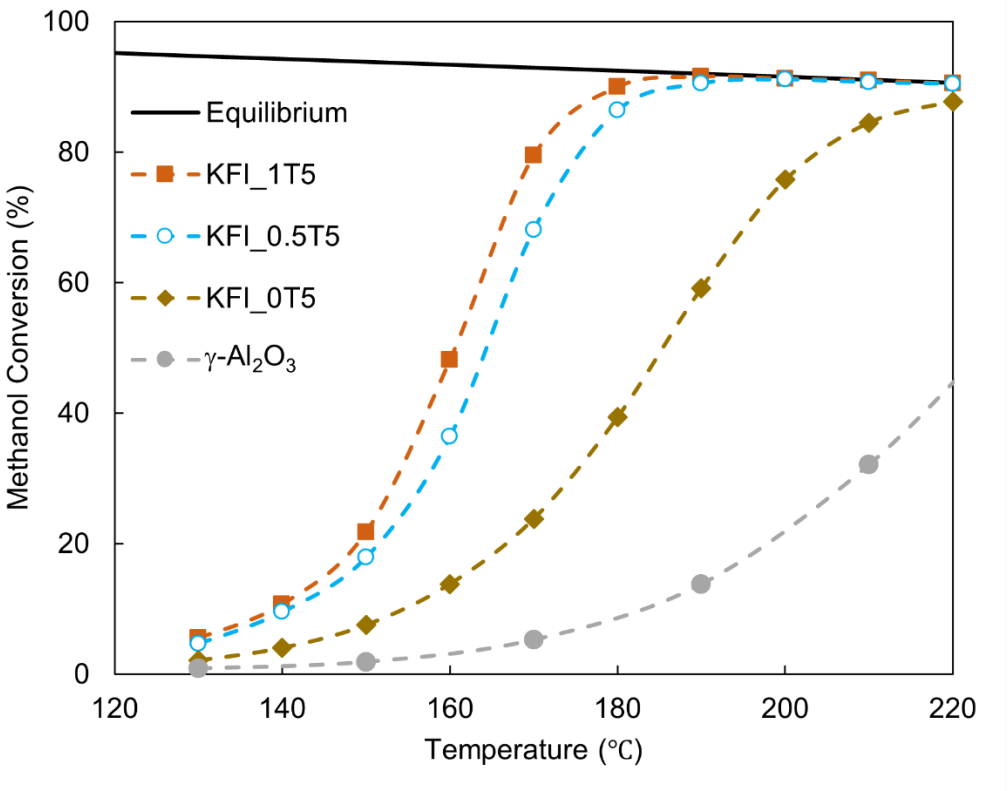

Figure 45. The catalytic activity of (■) KFI_1T5, (○) KFI_0.5T5, (◆) KFI_0T5, and (●) γ-Al_2O_3 for methanol dehydration at different temperature with WHSV = 4 h^{-1}.

A methanol conversion of less than 10% was observed for all samples at the lowest temperature of 130 °C. It was observed that as the temperature increased, there was a positive impact on methanol conversion. As a catalyst type comparison, zeolite samples yielded 4.3 – 6.6 times more conversion than γ-Al_2O_3 at 190 °C. Even at the highest temperature of 220 °C, the conversion rate over the alumina catalyst reached only approximately 40%. This lower performance can be attributed to the weak acidity exhibited by alumina, which possesses Lewis acid sites and lacks the strong acidity of zeolites which contain both Lewis and Bronsted acid sites.

FTIR spectroscopy analysis, provided in the literature, suggests that water adsorption on Lewis acid sites, such as those present on γ-Al_2O_3, is stronger than on Bronsted ones [199]. This implies significant competition between water molecules and methanol molecules for adsorption on the γ-Al_2O_3 catalyst surface. This competition becomes critical in methanol dehydration since equal moles of water and DME are produced during methanol dehydration. In contrast, higher slope of conversion curves were observed when KFI zeolites were employed as solid acid catalysts.

Remarkably, even the least active zeolite, KFI_0T5, exhibited a conversion of 59% at a low temperature of 190 ℃.

Analysis of the conversion rates, as reported in Table 8, revealed a specific catalytic activity order: KFI_1T5 > KFI_0.5T5 > KFI_0T5, which aligned with the surface area and number of acid sites order of these zeolite samples. The KFI_1T5 had 2.3 times higher conversion than KFI_0T5 at 180 ℃. Additionally, the results showed a reverse correlation between crystal size and catalytic activity, consistent with previous investigations [123]. These findings suggest that the utilization of templates in the synthesis of KFI zeolites has a beneficial effect on the degree of crystallinity, surface area, acid sites, and crystal size, ultimately improving methanol conversion efficiency. The results are in line with previous studies which have shown that the type and amount of template in synthetic gel and the removal method after synthesis have profound effects on the final zeolite activity [200,201].

Table 8. Methanol conversion at different temperature over commercial and synthesized zeolites

Sample	Conversion at 160 ℃	Conversion at 180 ℃	Conversion at 200 ℃	Conversion at 220 ℃
KFI1T5	48.1	89.9	91.2	90.4
KFI0T5	13.8	39.4	75.7	87.7
KFI0.5T5	36.4	86.4	91.1	90.4
KFI1T3	73.6	88.1	91.3	90.5
KFI1T7	49.6	90.8	91.4	90.5
MFI_15	29.2	76.5	90.7	90.4
MFI_25	19.4	55.9	87.5	90.3

Furthermore, the analysis of the gas released from the reactor demonstrated remarkable 100% selectivity for DME when each zeolite was employed as a catalyst. This high selectivity signifies the potential of KFI zeolites as efficient catalysts for DME production through methanol dehydration by reducing separation costs.

The experimental investigation illustrated in Figure 45, combined with the insights from previous literature, emphasizes the significant impact of catalyst selection on methanol conversion efficiency. Zeolites, particularly the KFI variants, outperformed the alumina catalyst due to their higher acidity and unique properties. The use of templates in the synthesis of KFI zeolites further enhanced their catalytic activity by improving crystallinity, surface area, and crystal size. These

findings contribute to the advancement of sustainable energy solutions by promoting the utilization of efficient catalysts in DME production from renewable sources.

5.4.2.2 The effect of hydrothermal processing duration

Among the KFI zeolites samples with different template quantities, KFI_1T5 demonstrated superior methanol dehydration activity. To further investigate the influence of crystallization time on the catalytic activity of KFI-type zeolites, additional tests were conducted at the same temperature range for zeolites with varying crystallization times of 3, 5, and 7 days. Figure 46 also shows the methanol conversion over commercial MFI zeolites for comparison.

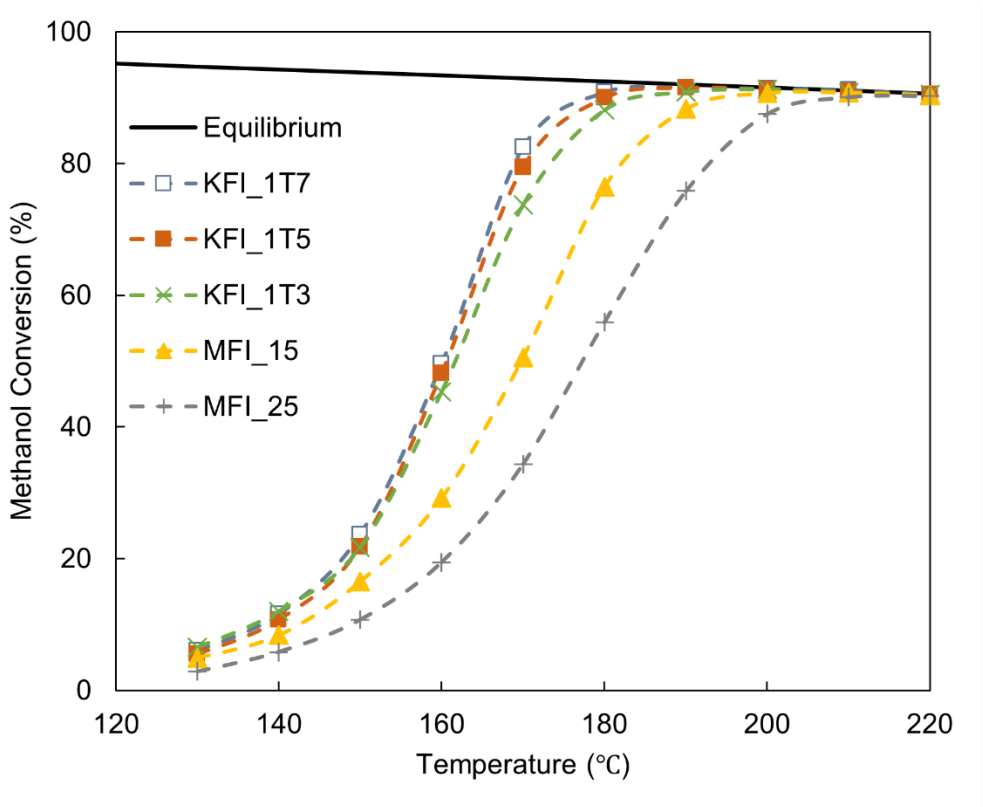

Figure 46. Methanol conversion versus temperature over (□) KFI_1T7, (■) KFI_1T5, (×) KFI_1T3, (▲) MFI_15, and (+) MFI_25 for methanol dehydration at different temperature with WHSV = 4 h^{-1}.

In the case of MFI_15 zeolites, the methanol conversion reached equilibrium at 210 – 220 °C, exhibiting superior conversion compared to previous studies involving this type of zeolite [23,72,96,191]. This is related to various initial gel compositions and preparation parameters used in the synthesis. For example, Migliori et al. prepared a gel with a Si/Al ratio of 25 (resulting in a final sample with 34 ratio) which exhibited 439 µmol g^{-1} total acidity. The catalyst required

temperatures > 240 °C for equilibrium conversion [72]. In another research, Rutkowska et al utilized a commercial MFI zeolite with Si/Al ratio of 16.5 (close to the ratio in this study) and achieved equilibrium conversion at 275 °C. The lower activity observed in their catalyst is attributed to its highly microporous structure (91% of surface area related to microporosity), whereas in this study, the catalyst has 76.4% of surface area related to microporosity due to different preparation factors [23]. Similarly, the enhanced performance of the MFI_15 sample compared to MFI_25 can be attributed to higher acidity (1942.4 μmol g^{-1} and 1307.7 μmol g^{-1}, respectively) stemming from its lower Si/Al ratio, as observed in other investigations. In addition, it has a higher micropore volume [175].

KFI zeolite samples with different crystallization times exhibited a shift in the conversion curve towards lower temperatures, indicating their increased activity in methanol dehydration while maintaining 100% selectivity for DME. KFI zeolites with full template presented at least 2.14 and 1.46 times higher DME yield than MFI_25 and MFI_15 at 170 °C, respectively. The activity results revealed the following order: KFI_1T7 > KFI_1T5 > KFI_1T3, highlighting the significant influence of hydrothermal processing time on the structure, surface area, and activity of the prepared zeolites. In this regard, the sample prepared by full template and 7 days of crystallization achieved an equilibrium conversion of ~91% at < 180 °C. While the activity improvement was less pronounced when increasing the crystallization time from 5 to 7 days than 3 to 5 days, the sample with a 9 day crystallization time was not investigated. Furthermore, an increase in acidity was observed when the synthesis time was extended from 3 days to 5 days. However, a reverse trend was observed when the synthesis time was further extended from 5 days to 7 days. Therefore, based on these findings, it can be concluded that both 5 and 7 days of crystallization represent the optimum synthesis times for KFI zeolite.

Achieving the highest specific surface area with 7 days of crystallization, the higher degree of crystallinity, the formation of mesopores, and a higher W/S acid sites ratio improved the zeolite's performance for the reaction in question. It became more suitable for methanol adsorption, dehydration, and efficient DME desorption. Mesoporosity creation through alkaline treatment and its beneficial effect on DME production have been studied extensively in previous projects [126,202]. This type of porosity, which increases the external surface area as determined by the T-plot method, enhances the accessibility of active sites for methanol molecules and facilitates the

diffusion of coke precursors, thereby preventing active area loss. This could explain why the more mesoporous sample with the higher crystallization time resulted in very good performance.

Additionally, it is worth mentioning that achieving an optimum value for the W/S ratio is crucial. Excessively high W/S ratio values can result in less active catalysts at low temperatures. Conversely, excessively low ratios can lead to rapid deactivation due to the susceptibility of strong acid sites to coke deposition. The recorded values of around 1.85 for KFI_1T7 appear to be the optimal ratio in this context.

Overall, the investigation of crystallization time and its impact on KFI zeolite catalytic activity revealed the importance of both structural characteristics and mesoporous formation in determining methanol conversion efficiency. The findings align with previous studies emphasizing the role of porosity in enhancing methanol dehydration and DME production.

5.4.2.3 Stability tests

The production of DME as an industrial process requires a catalyst that exhibits high activity and selectivity for methanol dehydration to DME, thereby reducing the cost of subsequent process separation steps for the reactor's output gas. In the previous section, the KFI_1T7 catalyst demonstrated excellent performance in meeting these requirements. However, catalyst stability is another critical factor in evaluating a catalyst for industrial-scale applications, as it directly impacts the need for reactor shutdowns or switching to replace or regenerate the catalyst, thereby affecting overall process costs.

For instance, certain highly acidic catalysts, such as HPAs (heteropoly acids), exhibit strong acidity and suitable activity at low temperatures but suffer from rapid deactivation within a few hours of operation (~4 h) [71,95]. To assess catalyst stability, the selected KFI catalyst and two commercial MFI samples were subjected to a continuous 100-hour reaction test. Figure 47 illustrates that MFI_15 and MFI_25 maintained stable conversion rates for 20 and 60 h of continuous operation, respectively. The loss of active sites caused by coke formation and particle agglomeration (Figure 48) led to adverse effects on MFI zeolite catalysts. In contrast, the methanol conversion over the synthesized KFI-type zeolite remained stable for at least 100 h. The consistent methanol dehydration rate after 100 h indicates high selectivity for DME and a low rate of coke formation, as investigated in Figure 49. The estimated coke formation was 0.33 $mg_{coke}\ g_{cat}^{-1}\ h^{-1}$,

0.25 $mg_{coke}\ g_{cat}^{-1}\ h^{-1}$, and 0.20 $mg_{coke}\ g_{cat}^{-1}\ h^{-1}$ for MFI_15, MFI_25, and KFI_1T7, respectively. Maintaining the temperature at 200 ℃ facilitated the drying of the catalysts, and the weight loss observed between 200 ℃ and 600 ℃ was attributed to the amount of coke deposited on the catalysts. First, the lowest coke deposit value measured on KFI_1T7 revealed its exceptional selectivity toward DME. Second, a high Weak/Strong (W/S) ratio aided the KFI sample in retaining its catalytic activity even with coke deposition. Moreover, SEM images of fresh and used catalysts revealed the structural stability of the KFI catalyst under process conditions.

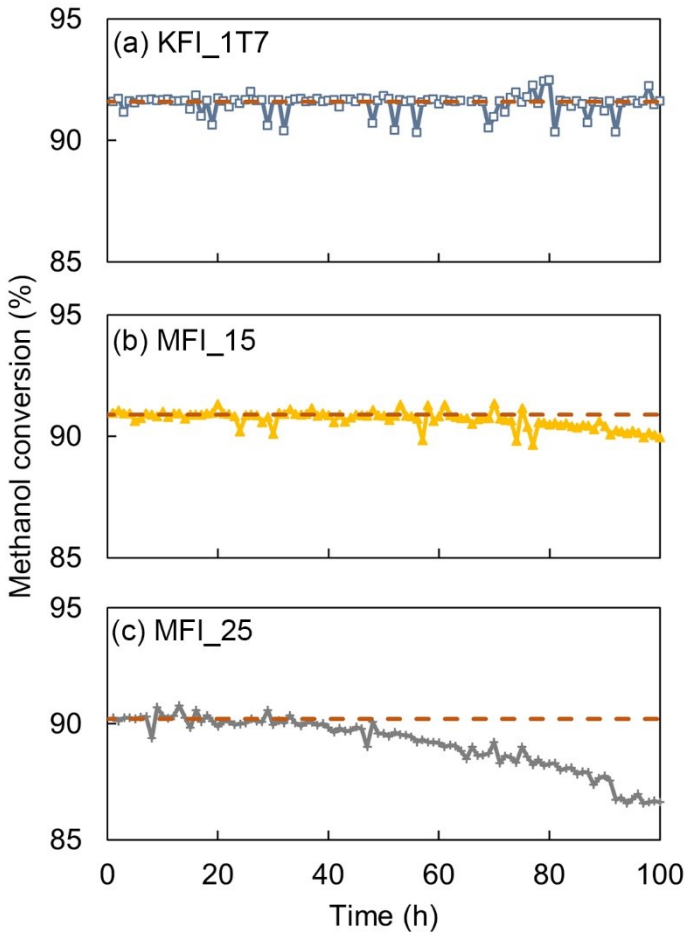

Figure 47. The conversion of methanol using (a) KFI_1T7, (b) MFI_15, (c) MFI_25, at their optimum temperatures for 100 h continuous reaction with WHSV = 4 h^{-1} (dash lines = the average of first 10 h conversion).

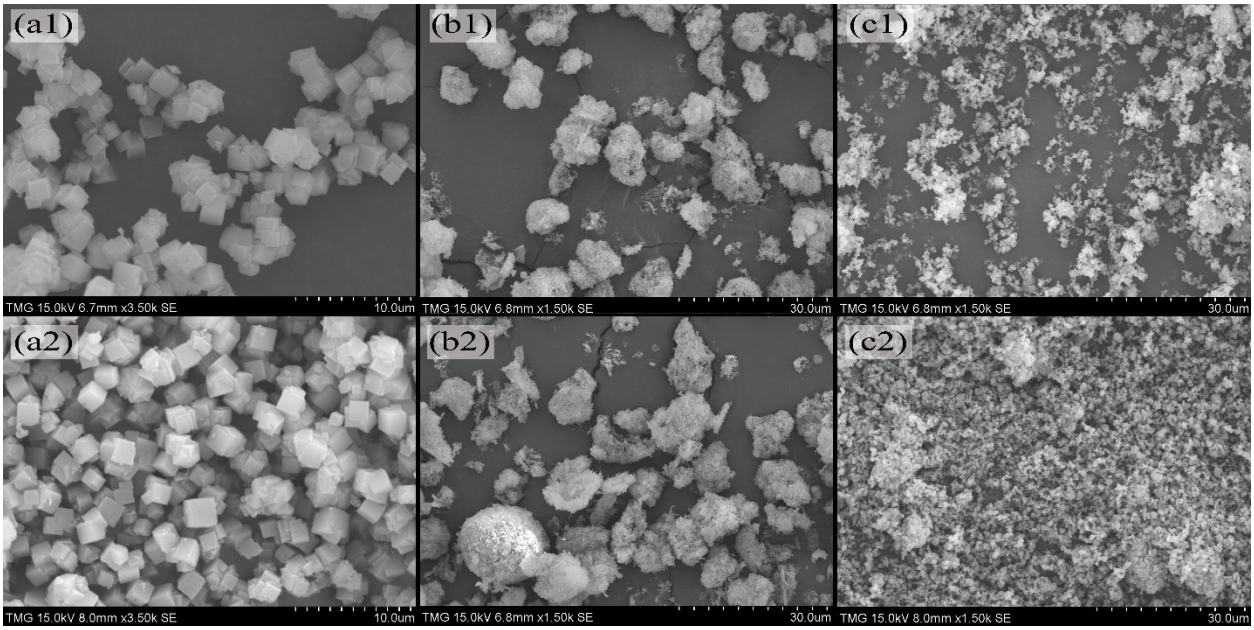

Figure 48. SEM images of spent catalysts before and after 100 h reaction including (a1) fresh KFI_1T7, (a2) used KFI_1T7, (b1) fresh MFI_15, (b2) used MFI_15, (c1) fresh MFI_25, (c2) used MFI_25.

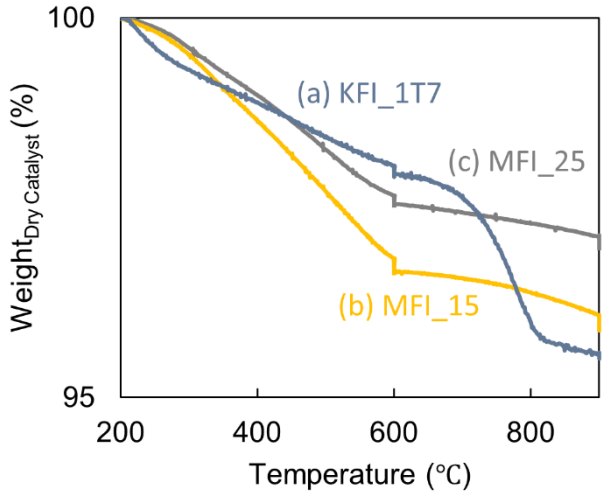

Figure 49. TGA path for spent (a) KFI_1T7 (b) MFI_15, (c) MFI_25 catalysts.

Moreover, to assess the activity of acid sites for methanol dehydration, the turnover frequency was calculated at 130 – 170 °C using Equation 10, where n, x, AS, and m represent the molar flow of methanol (mol h^{-1}), reaction conversion (dimensionless), acid sites (mol g^{-1}), and the catalyst weight, respectively. The results were shown in Figure 50, confirming the higher activity of acid sites present in KFI_1T7. As summarized in Table 9, KFI with TOF of 41.8 h^{-1} provided 1.26 times higher TOF than MFI zeolites. Therefore, the type of zeolite can have an important effect on the methanol dehydration while both KFI and MFI possess Bronsted and Lewis acid sites.

$$TOF = \frac{n_{MeOH} \times x_{MeOH}}{AS_{total} m_{cat}} \quad (10)$$

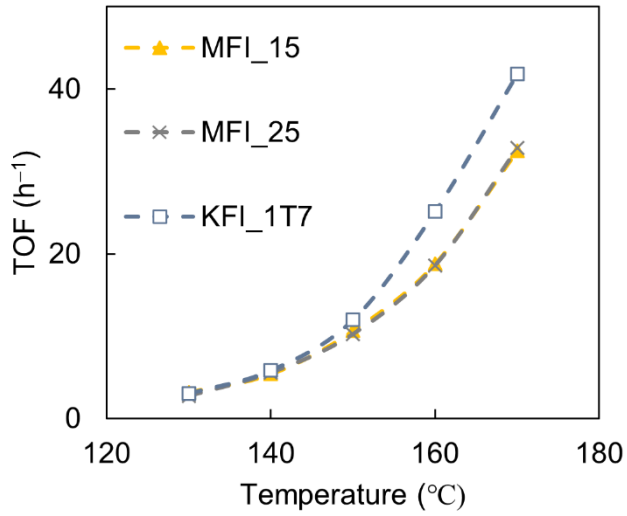

Figure 50. Turnover frequency calculated for KFI_1T7, MFI_15, and MFI_25 at low temperatures (130 – 170 °C)

Figure 51 illustrates the results of acidity analysis by DRIFTS for KFI_1T7 and two reference MFI zeolites. The KFI zeolites displayed two peaks, while the MFI zeolites exhibited three peaks in the wavenumber range of 2240-2340 cm^{-1}, which corresponds to the vibration of CN bonds to acid sites. According to Pelmenschikov et al., this area reveals five distinct peaks at 2278 cm^{-1}, 2284 cm^{-1}, 2300 cm^{-1}, 2323 cm^{-1}, and 2332 cm^{-1}, which are associated with CN bonds to terminal SiOH, nonacidic sites, bridging OH groups, weak Lewis acid sites, and strong acid sites, respectively [139]. Applying this definition, the L/B ratio was 0.39, 0.33, and 0.13 for KFI_1T7, MFI_15, and MFI_25, respectively, which is in reverse correlation with Si/Al ratio of zeolites as expected. The presence of huge band at 2278 cm^{-1} for KFI_1T7 represents the importance of CN bonds with SiOH groups while the previous papers focused on the band at 2300 cm^{-1} [191].

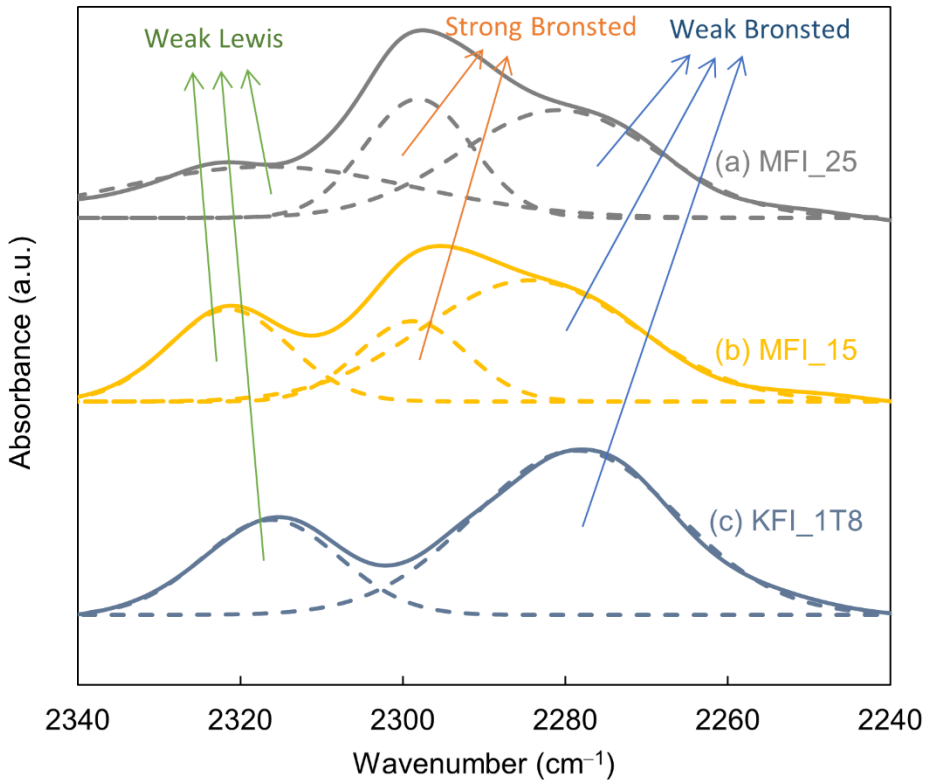

Figure 51. IR Spectra of (a) MFI_25, (b) MFI_15, and (c) KFI_1T7 after saturation with acetonitrile (recorded pattern = solid line, after deconvolution = dash lines)

The results of the coke analysis conducted by GC-MS were presented in Figure 52. It is important to highlight that digestion using 4 M KOH and extraction with DCM were completed, as no insoluble compounds were observed. For MFI zeolites with 10-member ring channels, two aromatic compounds, namely pentamethyl benzene and hexamethyl benzene, were detected, which is consistent with the literature [123]. In contrast, the 8-member ring of KFI zeolite led to the production of coke with a longer length and smaller diameter, resulting in compounds such as 2,6-dimethyl nonane ($C_{11}H_{24}$) and 1,3-bis(1,1-dimethylethyl) benzene ($C_{14}H_{22}$).

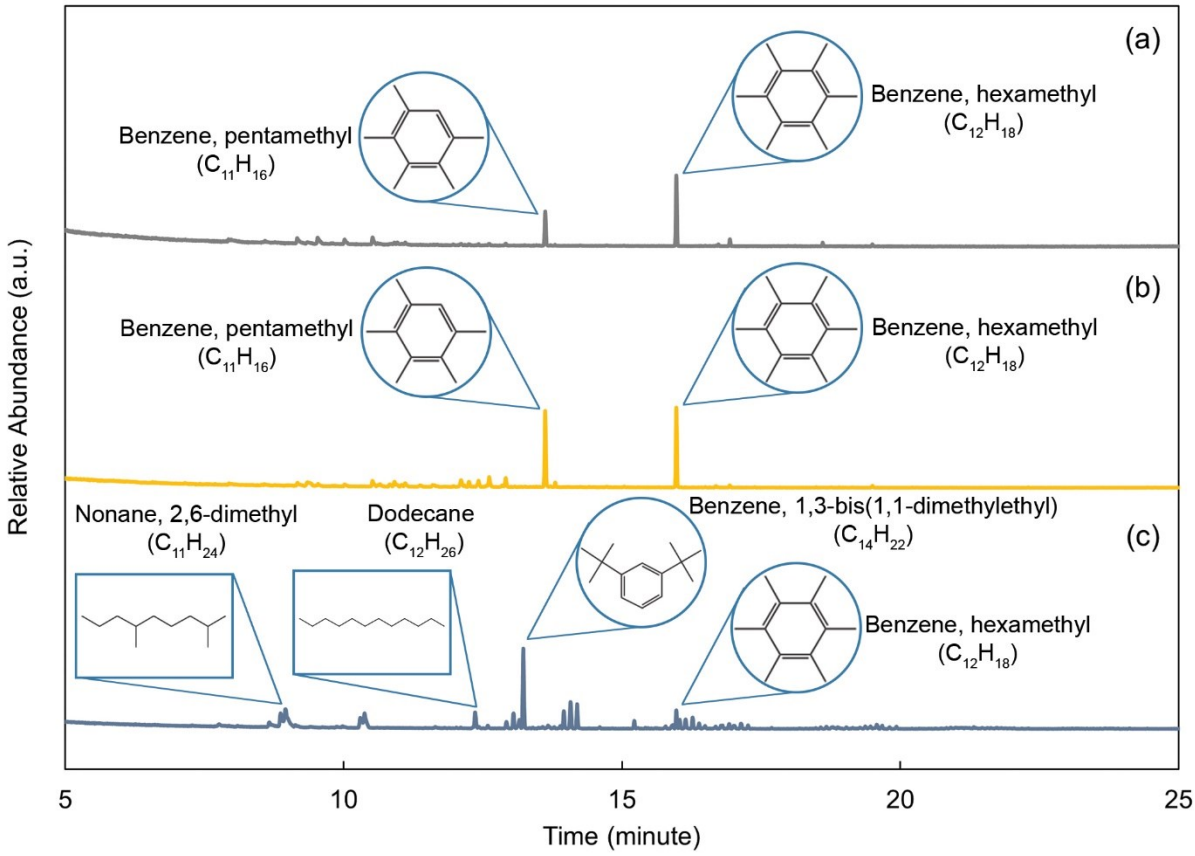

Figure 52. The results of coke analysis by GC-MS for (a) MFI_25, (b) MFI_15, (c) KFI_1T7.

Using equation 11, the selectivity of each catalyst to produce coke from methanol was estimated based on the results of coke deposition on the catalyst by TGA analysis and the composition of coke determined by GC-MS. In equation 2, $M_{MeOH \rightarrow Coke}$, n, x, and t represent methanol converted to coke based on the TGA result (mol), methanol flow (mol h^{-1}), conversion (dimensionless), and total time (100 h). The KFI_1T7 catalyst exhibited the lowest selectivity of 0.011% for coke generation.

$$S_{coke} = \frac{M_{MeOH \rightarrow Coke}}{(n_{MeOH} \times x_{MeOH} \times t) + M_{MeOh \rightarrow Coke}} \quad (11)$$

Table 9. Coke analysis and TOF calculated for various zeolites

Sample	Coke formation rate (mg $g_{dry\_cat}^{-1}$ h^{-1})	Methanol conversion selectivity to coke (%)	Main coke compositions	TOF at 170 °C (h^{-1})
KFI_1T7	0.20	0.011	$C_{12}H_{18}$ (aromatic)	41.8

MFI_15	0.34	0.021	$C_{11}H_{16}$ (aromatic) $C_{12}H_{18}$ (aromatic)	32.5
MFI_25	0.25	0.016	$C_{11}H_{24}$ (aliphatic) $C_{14}H_{22}$ (aromatic)	32.8

The presence of a mesoporous morphology in KFI zeolite played a dual role: first, enhancing activity by providing more accessible active sites, and second, increasing stability by preventing heavy coke deposits and pore collapse. The remarkable activity and stability test results highlight the substantial potential of synthesized KFI zeolite, prepared using the provided method, for cost-effective DME production. This zeolite shows promise in reducing catalyst costs by undergoing a long process time while maintaining excellent activity and selectivity for DME synthesis [8].

5.5 Conclusions

This paper investigates the production of DME through methanol dehydration, utilizing synthesized KFI-type zeolites in comparison to commercial MFI (ZSM-5) zeolites, a γ-Al_2O_3 catalyst as benchmarks. Five KFI zeolites were prepared by varying the template amount (zero, half, full) and crystallization time (3, 5, 7 days). XRD, SEM, and BET analyses revealed the significance of the template in transforming the initial gel into zeolites with high crystallinity and surface area. Moreover, N_2 adsorption/desorption profiles indicated that a crystallization time of 7 days played a crucial role in creating a mesoporous structure. The analysis of acid sites and acidity strength using NH_3-TPD revealed the positive influence of a lower Si/Al ratio on the increased acidity of MFI zeolites. Moreover, the synthesis parameters demonstrated a beneficial impact on achieving an optimal sample (KFI_1T7). This sample contained a remarkable 2466 μmol/g of acid sites and a favorable weak/strong ratio of 1.85. These characteristics enable the KFI_1T7 sample to provide thermodynamic conversion at various temperatures (weak acid sites for high temperatures and strong ones for low temperatures) over an extended period of time.

Activity tests were conducted at temperatures ranging from 130 ℃ to 220 ℃, using a WHSV of 4 h^{-1} and a feed containing 30% methanol. The conversion-temperature relationship demonstrated that zeolite with a full template and 7 days of crystallization exhibited improved methanol

conversion, reaching equilibrium conversion at approximately 180 °C. Furthermore, the stability of the most active KFI zeolite was compared to commercial MFI zeolites over a 100-hour methanol dehydration reaction. The synthesized KFI_1T7 zeolite displayed stable activity over 100 h, while the two commercial catalysts maintained stability for only 25-60 h. TGA/DTA indicated the lowest coke formation rate (0.20 mg_{coke} g_{cat}^{-1} h^{-1}) for KFI_1T7 compared to other catalysts. Also, the highest TOF of 41.8 h^{-1} and lowest selectivity to coke (0.011%) was calculated for optimum KFI. Coke analysis indicated that smaller channel size of KFI than MFI zeolites led to coke composition with smaller diameter.

These findings demonstrate the importance of template amount and crystallization time in synthesizing KFI zeolites with enhanced activity, stability, and lower coke formation. The KFI_1T7 zeolite shows significant potential for DME production, outperforming commercial catalysts in terms of activity at low temperatures, stability, and coke formation.

CHAPTER 6: CONCLUSIONS AND FUTURE WORK

6.1 Conclusions

In this comprehensive study, the potential of two types of zeolites, RHO and KFI, for DME production from methanol was thoroughly investigated. Methanol dehydration experiments were conducted at various temperatures to identify the most active samples from each zeolite type, and various characterization techniques were employed to understand catalytic properties responsible for these changes.

Among the RHO-type zeolites, the sample synthesized with a 10-day crystallization period using a full template exhibited the highest activity. This sample achieved an impressive conversion rate of over 91% at 190°C with more than 70 h stability. Similarly, within the KFI zeolite group, the sample prepared with a 7-day crystallization duration and utilizing a full template displayed superior activity compared to other synthesized KFI zeolites. Notably, this sample achieved equilibrium methanol conversion at a low temperature of 180°C, which is a significant advancement in the DME production process.

Subsequently, the activity of these selected zeolite samples was compared to two commercially available MFI (ZSM-5) catalysts. This catalyst is commonly employed in industrial settings for methanol dehydration. The KFI zeolite demonstrated exceptional stability, maintaining high conversion rates for over 100 h of continuous reaction. Also, only a 0.5% decrease was observed using RHO zeolite in the reactor.

To gain deeper insights into the physicochemical properties of the prepared catalysts, a set of characterization experiments was conducted. Techniques such as XRD, BET, NH3-TPD, SEM, EDS, and TGA were employed. The results revealed that both KFI and RHO samples exhibited high surface areas of over 391 and 671 $m^2 g^{-1}$, respectively, surpassing the surface areas of the two MFI zeolites (233 and 360 $m^2 g^{-1}$). Furthermore, the synthesized zeolites displayed higher acidity strength than commercial catalysts, which provides an explanation for their superior activity. The characterization also revealed the order of coke formation as RHO > ZSM > KFI, indicating the high selectivity of the KFI-type zeolite towards DME production. The optimum KFI sample

exhibited the lowest coke production rate of 0.20 $mg_{coke}\ g_{cat}^{-1}\ h^{-1}$ among MFI and RHO zeolites with a high turnover frequency of 41 h^{-1}.

Collectively, these findings underscore the high potential of KFI zeolite as an industrial catalyst for the methanol dehydration reaction. The superior activity, stability, and physicochemical characteristics exhibited by KFI zeolite, coupled with its high selectivity towards DME production, make it a promising candidate for implementation in large-scale DME synthesis processes.

6.2 Future Work

Regarding the numerous applications of DME, further investigation is necessary to establish a more cost-effective production pathway. Direct DME production has been proposed as a more convenient approach to overcome thermodynamic limitations and reduce production costs. Therefore, it is essential to explore the potential of hybrid catalysts combining prepared KFI zeolite with a suitable copper-based catalyst for efficient DME synthesis from CO/CO_2 mixtures. Moreover, future studies should focus on developing template-free KFI zeolite with comparable activity. Additionally, conducting in situ methanol conversion experiments can shed light on the mechanisms of methanol adsorption, surface reactions, formation of transitional compounds on catalyst surfaces, and DME desorption, thereby enhancing our understanding of the process.

REFERENCES

[1] N. Teasdale, P.K. Panegyres, Climate change in Western Australia and its impact on human health, J. Clim. Chang. Heal. 12 (2023). https://doi.org/10.1016/j.joclim.2023.100243.

[2] M.J.B. Kabeyi, O.A. Olanrewaju, Sustainable Energy Transition for Renewable and Low Carbon Grid Electricity Generation and Supply, Front. Energy Res. 9 (2022). https://doi.org/10.3389/fenrg.2021.743114.

[3] M. Semmel, R.E. Ali, M. Ouda, A. Schaadt, J. Sauer, C. Hebling, Power-to-DME: A cornerstone towards a sustainable energy system, in: Power to Fuel How to Speed Up a Hydrog. Econ., Elsevier, 2021: pp. 123–151. https://doi.org/10.1016/B978-0-12-822813-5.00010-2.

[4] C. Mevawala, Y. Jiang, D. Bhattacharyya, Techno-economic optimization of shale gas to dimethyl ether production processes via direct and indirect synthesis routes, Appl. Energy. 238 (2019) 119–134. https://doi.org/10.1016/j.apenergy.2019.01.044.

[5] A.T. Aguayo, J. Ereña, D. Mier, J.M. Arandes, M. Olazar, J. Bilbao, Kinetic modeling of dimethyl ether synthesis in a single step on a CuO-ZnO-Al2O3/γ-Al2O3 catalyst, Ind. Eng. Chem. Res. 46 (2007) 5522–5530. https://doi.org/10.1021/ie070269s.

[6] A. Khaleque, M.M. Alam, M. Hoque, S. Mondal, J. Bin Haider, B. Xu, M.A.H. Johir, A.K. Karmakar, J.L. Zhou, M.B. Ahmed, M.A. Moni, Zeolite synthesis from low-cost materials and environmental applications: A review, Environ. Adv. 2 (2020). https://doi.org/10.1016/j.envadv.2020.100019.

[7] M. Król, Natural vs. Synthetic zeolites, Crystals. 10 (2020) 1–8. https://doi.org/10.3390/cryst10070622.

[8] A. Lotfollahzade Moghaddam, M.J. Hazlett, Methanol dehydration catalysts in direct and indirect dimethyl ether (DME) production and the beneficial role of DME in energy supply and environmental pollution, J. Environ. Chem. Eng. 11 (2023) 110307. https://doi.org/https://doi.org/10.1016/j.jece.2023.110307.

[9] I. Dincer, M.A. Rosen, Exergy: Energy, Environment and Sustainable Development, Elsevier, 2020. https://doi.org/10.1016/B978-0-12-824372-5.09986-3.

[10] Total energy production (eia reports), Washington, n.d. https://www.eia.gov/international/data/world.

[11] S.M. Bernard, J.M. Samet, A. Grambsch, K.L. Ebi, I. Romieu, The potential impacts of climate variability and change on air pollution-related health effects in the United States, Environ. Health Perspect. 109 (2001) 199–209. https://doi.org/10.2307/3435010.

[12] M. Mahmoud, M. Ramadan, A.G. Olabi, K. Pullen, S. Naher, A review of mechanical energy storage systems combined with wind and solar applications, Energy Convers. Manag. 210 (2020). https://doi.org/10.1016/j.enconman.2020.112670.

[13] M. Tabassum, S.B.A. Kashem, M.B.M. Siddique, Feasibility of using Photovoltaic (PV)

technology to generate solar energy in Sarawak, in: 1st Int. Conf. Comput. Drone Appl. Ethical Integr. Comput. Drone Technol. Humanit. Sustain. IConDA 2017, Institute of Electrical and Electronics Engineers Inc., 2017: pp. 11–16. https://doi.org/10.1109/ICONDA.2017.8270391.

[14] A.M.A. Haidar, M.F.M. Senan, A. Noman, T. Radman, Utilization of pico hydro generation in domestic and commercial loads, Renew. Sustain. Energy Rev. 16 (2012) 518–524. https://doi.org/10.1016/j.rser.2011.08.017.

[15] R. Bhandari, C.A. Trudewind, P. Zapp, Life cycle assessment of hydrogen production via electrolysis - A review, J. Clean. Prod. 85 (2014) 151–163. https://doi.org/10.1016/j.jclepro.2013.07.048.

[16] E. Catizzone, C. Freda, G. Braccio, F. Frusteri, G. Bonura, Dimethyl ether as circular hydrogen carrier: Catalytic aspects of hydrogenation/dehydrogenation steps, J. Energy Chem. 58 (2021) 55–77. https://doi.org/10.1016/j.jechem.2020.09.040.

[17] T. Xiu, J. Wang, Q. Liu, Ordered bimodal mesoporous boria-alumina composite: One-step synthesis, structural characterization, active catalysis for methanol dehydration, Microporous Mesoporous Mater. 143 (2011) 362–367. https://doi.org/10.1016/j.micromeso.2011.03.014.

[18] Y. Onaka, A. Miyara, K. Tsubaki, Experimental study on evaporation heat transfer of CO2/DME mixture refrigerant in a horizontal smooth tube, Int. J. Refrig. 33 (2010) 1277–1291. https://doi.org/10.1016/j.ijrefrig.2010.06.014.

[19] V. Rao, W. Vizuete, Chapter Eleven - Alternative fuels, in: V. Rao, W.B.T.-P.M. Vizuete (Eds.), Emerg. Issues Anal. Chem., Elsevier, 2021: pp. 181–197. https://doi.org/https://doi.org/10.1016/B978-0-12-816904-9.00023-4.

[20] W. An, K.T. Chuang, A.R. Sanger, Dehydration of methanol to dimethyl ether by catalytic distillation, Can. J. Chem. Eng. 82 (2004) 948–955. https://doi.org/10.1002/cjce.5450820510.

[21] A. García-Trenco, A. Vidal-Moya, A. Martínez, Study of the interaction between components in hybrid CuZnAl/HZSM-5 catalysts and its impact in the syngas-to-DME reaction, Catal. Today. 179 (2012) 43–51. https://doi.org/10.1016/j.cattod.2011.06.034.

[22] C. Herrera, M. Cortés-Reyes, M.Á. Larrubia, M.V. Domínguez-Barroso, M.R. Díaz-Rey, L.J. Alemany, Dimethyl ether synthesis via methanol dehydration over Ta-supported catalysts, Appl. Catal. A Gen. 582 (2019) 117088. https://doi.org/10.1016/j.apcata.2019.05.022.

[23] M. Rutkowska, D. Macina, N. Mirocha-Kubień, Z. Piwowarska, L. Chmielarz, Hierarchically structured ZSM-5 obtained by desilication as new catalyst for DME synthesis from methanol, Appl. Catal. B Environ. 174–175 (2015) 336–343. https://doi.org/10.1016/j.apcatb.2015.03.006.

[24] K. Saravanan, H. Ham, N. Tsubaki, J.W. Bae, Recent progress for direct synthesis of dimethyl ether from syngas on the heterogeneous bifunctional hybrid catalysts, Appl. Catal. B Environ. 217 (2017) 494–522. https://doi.org/10.1016/j.apcatb.2017.05.085.

[25] M.C. Lee, S. Bin Seo, J.H. Chung, Y.J. Joo, D.H. Ahn, Industrial gas turbine combustion performance test of DME to use as an alternative fuel for power generation, Fuel. 88 (2009) 657–662. https://doi.org/10.1016/j.fuel.2008.10.027.

[26] K.C. Tokay, T. Dogu, G. Dogu, Dimethyl ether synthesis over alumina based catalysts, Chem. Eng. J. 184 (2012) 278–285. https://doi.org/10.1016/j.cej.2011.12.034.

[27] D. Cocco, V. Tola, G. Cau, Performance evaluation of chemically recuperated gas turbine (CRGT) power plants fuelled by di-methyl-ether (DME), Energy. 31 (2006) 1446–1458. https://doi.org/10.1016/j.energy.2005.05.015.

[28] T.H. Fleisch, A. Basu, M.J. Gradassi, J.G. Masin, Dimethyl ether: A fuel for the 21st century, Stud. Surf. Sci. Catal. 107 (1997) 117–125. https://doi.org/10.1016/s0167-2991(97)80323-0.

[29] L. Xing-Cai, Y. Jian-Guang, Z. Wu-Gao, H. Zhen, Effect of cetane number improver on heat release rate and emissions of high speed diesel engine fueled with ethanol-diesel blend fuel, in: Fuel, 2004: pp. 2013–2020. https://doi.org/10.1016/j.fuel.2004.05.003.

[30] R. Li, Z. Wang, P. Ni, Y. Zhao, M. Li, L. Li, Effects of cetane number improvers on the performance of diesel engine fuelled with methanol/biodiesel blend, Fuel. 128 (2014) 180–187. https://doi.org/10.1016/j.fuel.2014.03.011.

[31] S.H. Park, C.S. Lee, Applicability of dimethyl ether (DME) in a compression ignition engine as an alternative fuel, Energy Convers. Manag. 86 (2014) 848–863. https://doi.org/10.1016/j.enconman.2014.06.051.

[32] M. Marchionna, R. Patrini, D. Sanfilippo, G. Migliavacca, Fundamental investigations on di-methyl ether (DME) as LPG substitute or make-up for domestic uses, Fuel Process. Technol. 89 (2008) 1255–1261. https://doi.org/10.1016/j.fuproc.2008.07.013.

[33] T.H. Fleisch, A. Basu, R.A. Sills, Introduction and advancement of a new clean global fuel: The status of DME developments in China and beyond, J. Nat. Gas Sci. Eng. 9 (2012) 94–107. https://doi.org/10.1016/j.jngse.2012.05.012.

[34] C. Ortega, G. Kolb, DME-to-Hydrocarbon over an MFI Zeolite: Product Selectivity Controlled by Oxygenates under the Kinetic Regime, Ind. Eng. Chem. Res. 58 (2019) 22893–22904. https://doi.org/10.1021/acs.iecr.9b04735.

[35] R.B. Diemer, W.L. Luyben, Design and control of a methyl acetate process using carbonylation of dimethyl ether, Ind. Eng. Chem. Res. 49 (2010) 12224–12241. https://doi.org/10.1021/ie101583j.

[36] D. Liu, X. Huang, L. Hu, D. Fang, W. Ying, D. Chen, Synthesis of ethylidene diacetate from dimethyl ether, CO and H2, J. Nat. Gas Chem. 19 (2010) 165–168. https://doi.org/10.1016/S1003-9953(09)60052-9.

[37] T.A. Semelsberger, R.L. Borup, H.L. Greene, Dimethyl ether (DME) as an alternative fuel, J. Power Sources. 156 (2006) 497–511. https://doi.org/10.1016/j.jpowsour.2005.05.082.

[38] T. Fukunaga, N. Ryumon, S. Shimazu, The influence of metals and acidic oxide species

on the steam reforming of dimethyl ether (DME), Appl. Catal. A Gen. 348 (2008) 193–200. https://doi.org/10.1016/j.apcata.2008.06.031.

[39] E. Ozensoy, D. Herling, J. Szanyi, NOx reduction on a transition metal-free γ-Al2O3 catalyst using dimethylether (DME), Catal. Today. 136 (2008) 46–54. https://doi.org/10.1016/j.cattod.2007.12.095.

[40] K. Faungnawakij, T. Fukunaga, R. Kikuchi, K. Eguchi, Deactivation and regeneration behaviors of copper spinel-alumina composite catalysts in steam reforming of dimethyl ether, J. Catal. 256 (2008) 37–44. https://doi.org/10.1016/j.jcat.2008.02.022.

[41] G. Centi, S. Perathoner, Opportunities and prospects in the chemical recycling of carbon dioxide to fuels, Catal. Today. 148 (2009) 191–205. https://doi.org/10.1016/j.cattod.2009.07.075.

[42] A.T. Aguayo, J. Ereña, I. Sierra, M. Olazar, J. Bilbao, Deactivation and regeneration of hybrid catalysts in the single-step synthesis of dimethyl ether from syngas and CO2, Catal. Today. 106 (2005) 265–270. https://doi.org/10.1016/j.cattod.2005.07.144.

[43] W.H. Chen, C.L. Hsu, X.D. Wang, Thermodynamic approach and comparison of two-step and single step DME (dimethyl ether) syntheses with carbon dioxide utilization, Energy. 109 (2016) 326–340. https://doi.org/10.1016/j.energy.2016.04.097.

[44] T. Nakyai, Y. Patcharavorachot, A. Arpornwichanop, D. Saebea, Comparative exergoeconomic analysis of indirect and direct bio-dimethyl ether syntheses based on air-steam biomass gasification with CO2 utilization, Energy. 209 (2020) 118332. https://doi.org/10.1016/j.energy.2020.118332.

[45] A. Wodołażski, A. Smoliński, Modelling and process integration study of dimethyl ether synthesis from syngas derived from biomass gasification: Flowsheet simulation, Alexandria Eng. J. 59 (2020) 4441–4448. https://doi.org/10.1016/j.aej.2020.07.050.

[46] S. Natesakhawat, J.W. Lekse, J.P. Baltrus, P.R. Ohodnicki, B.H. Howard, X. Deng, C. Matranga, Active sites and structure-activity relationships of copper-based catalysts for carbon dioxide hydrogenation to methanol, ACS Catal. 2 (2012) 1667–1676. https://doi.org/10.1021/cs300008g.

[47] N.A. Samiran, M.N.M. Jaafar, J.H. Ng, S.S. Lam, C.T. Chong, Progress in biomass gasification technique - With focus on Malaysian palm biomass for syngas production, Renew. Sustain. Energy Rev. 62 (2016) 1047–1062. https://doi.org/10.1016/j.rser.2016.04.049.

[48] Y. Richardson, M. Drobek, A. Julbe, J. Blin, F. Pinta, Biomass Gasification to Produce Syngas, in: Recent Adv. Thermochem. Convers. Biomass, Elsevier Inc., 2015: pp. 213–250. https://doi.org/10.1016/B978-0-444-63289-0.00008-9.

[49] A. Molino, S. Chianese, D. Musmarra, Biomass gasification technology: The state of the art overview, J. Energy Chem. 25 (2016) 10–25. https://doi.org/10.1016/j.jechem.2015.11.005.

[50] Z. Shi, Q. Tan, C. Tian, Y. Pan, X. Sun, J. Zhang, D. Wu, CO2 hydrogenation to methanol over Cu-In intermetallic catalysts: Effect of reduction temperature, J. Catal. 379 (2019)

78–89. https://doi.org/10.1016/j.jcat.2019.09.024.

[51] C. Peinado, D. Liuzzi, M. Retuerto, J. Boon, M.A. Peña, S. Rojas, Study of catalyst bed composition for the direct synthesis of dimethyl ether from CO2-rich syngas, Chem. Eng. J. Adv. 4 (2020) 100039. https://doi.org/10.1016/j.ceja.2020.100039.

[52] S. Ren, X. Fan, Z. Shang, W.R. Shoemaker, L. Ma, T. Wu, S. Li, N.B. Klinghoffer, M. Yu, X. Liang, Enhanced catalytic performance of Zr modified CuO/ZnO/Al2O3 catalyst for methanol and DME synthesis via CO2 hydrogenation, J. CO2 Util. 36 (2020) 82–95. https://doi.org/10.1016/j.jcou.2019.11.013.

[53] M.M.J. Li, Z. Zeng, F. Liao, X. Hong, S.C.E. Tsang, Enhanced CO2 hydrogenation to methanol over CuZn nanoalloy in Ga modified Cu/ZnO catalysts, J. Catal. 343 (2016) 157–167. https://doi.org/10.1016/j.jcat.2016.03.020.

[54] C. Liu, X. Guo, Q. Guo, D. Mao, J. Yu, G. Lu, Methanol synthesis from CO2 hydrogenation over copper catalysts supported on MgO-modified TiO2, J. Mol. Catal. A Chem. 425 (2016) 86–93. https://doi.org/10.1016/j.molcata.2016.09.032.

[55] H. Ren, C.H. Xu, H.Y. Zhao, Y.X. Wang, J.Y.J. Liu, J.Y.J. Liu, Methanol synthesis from CO2 hydrogenation over Cu/γ-Al2O3 catalysts modified by ZnO, ZrO2 and MgO, J. Ind. Eng. Chem. 28 (2015) 261–267. https://doi.org/10.1016/j.jiec.2015.03.001.

[56] J. Zuo, K. Chen, J. Zheng, L. Ye, Y. Yuan, Enhanced CO2 hydrogenation to methanol over La oxide-modified Cu nanoparticles socketed on Cu phyllosilicate nanotubes, J. CO2 Util. 52 (2021). https://doi.org/10.1016/j.jcou.2021.101699.

[57] P. Gao, F. Li, N. Zhao, F. Xiao, W. Wei, L. Zhong, Y. Sun, Influence of modifier (Mn, La, Ce, Zr and Y) on the performance of Cu/Zn/Al catalysts via hydrotalcite-like precursors for CO2 hydrogenation to methanol, Appl. Catal. A Gen. 468 (2013) 442–452. https://doi.org/10.1016/j.apcata.2013.09.026.

[58] G. Wang, D. Mao, X. Guo, J. Yu, Enhanced performance of the CuO-ZnO-ZrO 2 catalyst for CO 2 hydrogenation to methanol by WO 3 modification, Appl. Surf. Sci. 456 (2018) 403–409. https://doi.org/10.1016/j.apsusc.2018.06.090.

[59] X. Cui, S. Chen, H. Yang, Y. Liu, H. Wang, H. Zhang, Y. Xue, G. Wang, Y. Niu, T. Deng, W. Fan, Improving methanol selectivity in CO2 hydrogenation by tuning the distance of Cu on catalyst, Appl. Catal. B Environ. 298 (2021). https://doi.org/10.1016/j.apcatb.2021.120590.

[60] G. Behrendt, B. Mockenhaupt, N. Prinz, M. Zobel, E.J. Ras, M. Behrens, CO Hydrogenation to Methanol over Cu/MgO Catalysts and Their Synthesis from Amorphous Magnesian Georgeite Precursors, ChemCatChem. 14 (2022) 1–13. https://doi.org/10.1002/cctc.202200299.

[61] Z. Ding, Y. Xu, Q. Yang, R. Hou, Pd-modified CuO–ZnO–ZrO2 catalysts for CH3OH synthesis from CO2 hydrogenation, Int. J. Hydrogen Energy. 47 (2022) 24750–24760. https://doi.org/10.1016/j.ijhydene.2022.05.226.

[62] C. Huang, C. Zhu, M. Zhang, J. Chen, K. Fang, Design of efficient ZnO/ZrO2 modified CuCoAl catalysts for boosting higher alcohol synthesis in syngas conversion, Appl. Catal.

B Environ. 300 (2022). https://doi.org/10.1016/j.apcatb.2021.120739.

[63] Y.N. Kochkin, N. V. Vlasenko, N. V. Kasian, O. V. Shvets, Effect of the Acidity of Ca,H-Bea Zeolites on Their Catalytic Characteristics in the Dimethyl Ether Production from Methanol, Theor. Exp. Chem. 51 (2015) 327–332. https://doi.org/10.1007/s11237-015-9433-7.

[64] Y.H. Seo, E.A. Prasetyanto, N. Jiang, S.M. Oh, S.E. Park, Catalytic dehydration of methanol over synthetic zeolite W, Microporous Mesoporous Mater. 128 (2010) 108–114. https://doi.org/10.1016/j.micromeso.2009.08.011.

[65] F. Yaripour, F. Baghaei, I. Schmidt, J. Perregaard, Catalytic dehydration of methanol to dimethyl ether (DME) over solid-acid catalysts, Catal. Commun. 6 (2005) 147–152. https://doi.org/10.1016/j.catcom.2004.11.012.

[66] M. Xu, D.W. Goodman, A. Bhattacharyya, Catalytic dehydration of methanol to dimethyl ether (DME) over Pd/Cab-O-Sil catalysts, Appl. Catal. A Gen. 149 (1997) 303–309. https://doi.org/10.1016/S0926-860X(96)00276-1.

[67] W. Dai, W. Kong, G. Wu, N. Li, L. Li, N. Guan, Catalytic dehydration of methanol to dimethyl ether over aluminophosphate and silico-aluminophosphate molecular sieves, Catal. Commun. 12 (2011) 535–538. https://doi.org/10.1016/j.catcom.2010.11.019.

[68] J. Schnee, A. Eggermont, E.M. Gaigneaux, Boron Nitride: A Support for Highly Active Heteropolyacids in the Methanol-to-DME Reaction, ACS Catal. 7 (2017) 4011–4017. https://doi.org/10.1021/acscatal.7b00808.

[69] R.M. Ladera, J.L.G. Fierro, M. Ojeda, S. Rojas, TiO2-supported heteropoly acids for low-temperature synthesis of dimethyl ether from methanol, J. Catal. 312 (2014) 195–203. https://doi.org/10.1016/j.jcat.2014.01.016.

[70] R.M. Ladera, M. Ojeda, J.L.G. Fierro, S. Rojas, TiO2-supported heteropoly acid catalysts for dehydration of methanol to dimethyl ether: Relevance of dispersion and support interaction, Catal. Sci. Technol. 5 (2015) 484–491. https://doi.org/10.1039/c4cy00998c.

[71] C. Peinado, D. Liuzzi, R.M. Ladera-Gallardo, M. Retuerto, M. Ojeda, M.A. Peña, S. Rojas, Effects of support and reaction pressure for the synthesis of dimethyl ether over heteropolyacid catalysts, Sci. Rep. 10 (2020) 1–12. https://doi.org/10.1038/s41598-020-65296-3.

[72] M. Migliori, E. Catizzone, A. Aloise, G. Bonura, L. Gómez-Hortigüela, L. Frusteri, C. Cannilla, F. Frusteri, G. Giordano, New insights about coke deposition in methanol-to-DME reaction over MOR-, MFI- and FER-type zeolites, J. Ind. Eng. Chem. 68 (2018) 196–208. https://doi.org/10.1016/j.jiec.2018.07.046.

[73] P. Huber, F. Studt, P.N. Plessow, Reactivity of Surface Lewis and Brønsted Acid Sites in Zeolite Catalysis: A Computational Case Study of DME Synthesis Using H-SSZ-13, J. Phys. Chem. C. 126 (2022) 5896–5905. https://doi.org/10.1021/acs.jpcc.2c00668.

[74] J. Abu-Dahrieh, D. Rooney, A. Goguet, Y. Saih, Activity and deactivation studies for direct dimethyl ether synthesis using CuO-ZnO-Al2O3 with NH4ZSM-5, HZSM-5 or γ-Al2O3, Chem. Eng. J. 203 (2012) 201–211. https://doi.org/10.1016/j.cej.2012.07.011.

[75] B. Pekmezci Karaman, N. Oktar, G. Doğu, T. Doğu, Bifunctional Silicotungstic Acid and Tungstophosphoric Acid Impregnated Cu–Zn–Al & Cu–Zn–Zr Catalysts for Dimethyl Ether Synthesis from Syngas, Catal. Letters. 150 (2020) 2744–2761. https://doi.org/10.1007/s10562-020-03171-6.

[76] Y.J. Lee, J.M. Kim, J.W. Bae, C.H. Shin, K.W. Jun, Phosphorus induced hydrothermal stability and enhanced catalytic activity of ZSM-5 in methanol to DME conversion, Fuel. 88 (2009) 1915–1921. https://doi.org/10.1016/j.fuel.2009.04.007.

[77] R. Montesano, A. Narvaez, D. Chadwick, Shape-selectivity effects in syngas-to-dimethyl ether conversion over Cu/ZnO/Al2O3 and zeolite mixtures: Carbon deposition and by-product formation, Appl. Catal. A Gen. 482 (2014) 69–77. https://doi.org/https://doi.org/10.1016/j.apcata.2014.05.009.

[78] E. Catizzone, S. Van Daele, M. Bianco, A. Di Michele, A. Aloise, M. Migliori, V. Valtchev, G. Giordano, Catalytic application of ferrierite nanocrystals in vapour-phase dehydration of methanol to dimethyl ether, Appl. Catal. B Environ. 243 (2019) 273–282. https://doi.org/10.1016/j.apcatb.2018.10.060.

[79] L. Kovarik, M. Bowden, J. Szanyi, High temperature transition aluminas in δ-Al2O3/θ-Al2O3 stability range: Review, J. Catal. 393 (2021) 357–368. https://doi.org/https://doi.org/10.1016/j.jcat.2020.10.009.

[80] S. Sahebdelfar, P.M. Bijani, F. Yaripour, Deactivation kinetics of γ-Al2O3 catalyst in methanol dehydration to dimethyl ether, Fuel. 310 (2022) 122443. https://doi.org/https://doi.org/10.1016/j.fuel.2021.122443.

[81] S.S. Akarmazyan, P. Panagiotopoulou, A. Kambolis, C. Papadopoulou, D.I. Kondarides, Methanol dehydration to dimethylether over Al2O3 catalysts, Appl. Catal. B Environ. 145 (2014) 136–148. https://doi.org/10.1016/j.apcatb.2012.11.043.

[82] M. Xu, J.H. Lunsford, D.W. Goodman, A. Bhattacharyya, Synthesis of dimethyl ether (DME) from methanol over solid-acid catalysts, Appl. Catal. A Gen. 149 (1997) 289–301. https://doi.org/10.1016/S0926-860X(96)00275-X.

[83] A. Masudi, N.W. Che Jusoh, O. Muraza, Recent progress on low rank coal conversion to dimethyl ether as clean fuel: A critical review, J. Clean. Prod. 277 (2020) 124024. https://doi.org/10.1016/j.jclepro.2020.124024.

[84] F. Yaripour, Z. Shariatinia, S. Sahebdelfar, A. Irandoukht, The effects of synthesis operation conditions on the properties of modified γ-alumina nanocatalysts in methanol dehydration to dimethyl ether using factorial experimental design, Fuel. 139 (2015) 40–50. https://doi.org/10.1016/j.fuel.2014.08.029.

[85] S.Y. Hosseini, M.R. Khosravi Nikou, Investigation of different precipitating agents effects on performance of γ-Al2O3 nanocatalysts for methanol dehydration to dimethyl ether, J. Ind. Eng. Chem. 20 (2014) 4421–4428. https://doi.org/10.1016/j.jiec.2014.02.010.

[86] M.A. Armenta, R. Valdez, J.M. Quintana, R. Silva-Rodrigo, L. Cota, A. Olivas, Highly selective CuO/Γ–Al2O3 catalyst promoted with hematite for efficient methanol dehydration to dimethyl ether, Int. J. Hydrogen Energy. 43 (2018) 6551–6560.

https://doi.org/10.1016/j.ijhydene.2018.02.051.

[87] A. Khaleel, Titanium-doped alumina for catalytic dehydration of methanol to dimethyl ether at relatively low temperatures, Fuel. 90 (2011) 2422–2427. https://doi.org/10.1016/j.fuel.2011.03.008.

[88] A. Khaleel, M. Ahmed, S.B. Sowaid, Ti-doped γ-Al 2 O 3 versus ZSM5 zeolites for methanol to dimethyl ether conversion: In-situ DRIFTS investigation of surface interactions and reaction mechanism, Colloids Surfaces A Physicochem. Eng. Asp. 571 (2019) 174–181. https://doi.org/10.1016/j.colsurfa.2019.03.052.

[89] A.I. Osman, J.K. Abu-Dahrieh, A. Abdelkader, N.M. Hassan, F. Laffir, M. McLaren, D. Rooney, Silver-Modified η-Al2O3 Catalyst for DME Production, J. Phys. Chem. C. 121 (2017) 25018–25032. https://doi.org/10.1021/acs.jpcc.7b04697.

[90] M. Nosonovsky, B. Bhushan, Hierarchical roughness optimization for biomimetic superhydrophobic surfaces, Ultramicroscopy. 107 (2007) 969–979. https://doi.org/10.1016/j.ultramic.2007.04.011.

[91] M.A. Armenta, V.M. Maytorena, L.A. Flores–Sánchez, J.M. Quintana, R. Valdez, A. Olivas, Dimethyl ether production via methanol dehydration using Fe3O4 and CuO over γ–χ–Al2O3 nanocatalysts, Fuel. 280 (2020) 118545. https://doi.org/10.1016/j.fuel.2020.118545.

[92] D.M. Sung, Y.H. Kim, E.D. Park, J.E. Yie, Correlation between acidity and catalytic activity for the methanol dehydration over various aluminum oxides, Res. Chem. Intermed. 36 (2010) 653–660. https://doi.org/10.1007/s11164-010-0201-y.

[93] I. V. Kozhevnikov, Catalysis by heteropoly acids and multicomponent polyoxometalates in liquid-phase reactions, Chem. Rev. 98 (1998) 171–198. https://doi.org/10.1021/cr960400y.

[94] H. Ilbeygi, I.Y. Kim, M.G. Kim, W. Cha, P.S.M. Kumar, D.-H. Park, A. Vinu, Highly Crystalline Mesoporous Phosphotungstic Acid: A High-Performance Electrode Material for Energy-Storage Applications, Angew. Chemie Int. Ed. 58 (2019) 10849–10854. https://doi.org/https://doi.org/10.1002/anie.201901224.

[95] W. Alharbi, E.F. Kozhevnikova, I. V. Kozhevnikov, Dehydration of Methanol to Dimethyl Ether over Heteropoly Acid Catalysts: The Relationship between Reaction Rate and Catalyst Acid Strength, ACS Catal. 5 (2015) 7186–7193. https://doi.org/10.1021/acscatal.5b01911.

[96] E. Catizzone, A. Aloise, M. Migliori, G. Giordano, From 1-D to 3-D zeolite structures: performance assessment in catalysis of vapour-phase methanol dehydration to DME, Microporous Mesoporous Mater. 243 (2017) 102–111. https://doi.org/10.1016/j.micromeso.2017.02.022.

[97] O. Verdes, V. Sasca, A. Popa, M. Suba, S. Borcanescu, Catalytic activity of heteropoly tungstate catalysts for ethanol dehydration reaction: Deactivation and regeneration, Catal. Today. 366 (2021) 123–132. https://doi.org/10.1016/j.cattod.2019.12.040.

[98] W. Vermeiren, J.P. Gilson, Impact of zeolites on the petroleum and petrochemical

industry, Top. Catal. 52 (2009). https://doi.org/10.1007/s11244-009-9271-8.

[99] J. Přech, P. Pizarro, D.P. Serrano, J. Áejka, From 3D to 2D zeolite catalytic materials, Chem. Soc. Rev. 47 (2018). https://doi.org/10.1039/c8cs00370j.

[100] S. Mintova, M. Jaber, V. Valtchev, Nanosized microporous crystals: emerging applications, Chem. Soc. Rev. 44 (2015). https://doi.org/10.1039/c5cs00210a.

[101] Y. Li, J. Yu, New stories of zeolite structures: Their descriptions, determinations, predictions, and evaluations, Chem. Rev. 114 (2014) 7268–7316. https://doi.org/10.1021/cr500010r.

[102] Y. Li, L. Li, J. Yu, Applications of Zeolites in Sustainable Chemistry, Chem. 3 (2017). https://doi.org/10.1016/j.chempr.2017.10.009.

[103] P. Guo, K. Strohmaier, H. Vroman, M. Afeworki, P.I. Ravikovitch, C.S. Paur, J. Sun, A. Burton, X. Zou, Accurate structure determination of a borosilicate zeolite EMM-26 with two-dimensional 10 × 10 ring channels using rotation electron diffraction, Inorg. Chem. Front. 3 (2016) 1444–1448. https://doi.org/10.1039/c6qi00262e.

[104] C. Tan, Z. Liu, Y. Yonezawa, S. Sukenaga, M. Ando, H. Shibata, Y. Sasaki, T. Okubo, T. Wakihara, Unique crystallization behavior in zeolite synthesis under external high pressures, Chem. Commun. 56 (2020) 2811–2814. https://doi.org/10.1039/c9cc09966b.

[105] S. Mintova, V. Valtchev, T. Onfroy, C. Marichal, H. Knözinger, T. Bein, Variation of the Si/Al ratio in nanosized zeolite Beta crystals, Microporous Mesoporous Mater. 90 (2006) 237–245. https://doi.org/10.1016/j.micromeso.2005.11.026.

[106] C.S. Cundy, P.A. Cox, The hydrothermal synthesis of zeolites: Precursors, intermediates and reaction mechanism, Microporous Mesoporous Mater. 82 (2005) 1–78. https://doi.org/10.1016/j.micromeso.2005.02.016.

[107] A. Burton, Recent trends in the synthesis of high-silica zeolites, Catal. Rev. - Sci. Eng. 60 (2018) 132–175. https://doi.org/10.1080/01614940.2017.1389112.

[108] Y. Wang, Q. Wu, X. Meng, F.S. Xiao, Insights into the Organotemplate-Free Synthesis of Zeolite Catalysts, Engineering. 3 (2017) 567–574. https://doi.org/10.1016/J.ENG.2017.03.029.

[109] X. Meng, Q. Wu, F. Chen, F.S. Xiao, Solvent-free synthesis of zeolite catalysts, Sci. China Chem. 58 (2015) 6–13. https://doi.org/10.1007/s11426-014-5252-2.

[110] Z. Wang, Y. Jiang, O. Lafon, J. Trébosc, K. Duk Kim, C. Stampfl, A. Baiker, J.P. Amoureux, J. Huang, Brønsted acid sites based on penta-coordinated aluminum species, Nat. Commun. 7 (2016). https://doi.org/10.1038/ncomms13820.

[111] M. Ravi, V.L. Sushkevich, J.A. van Bokhoven, On the location of Lewis acidic aluminum in zeolite mordenite and the role of framework-associated aluminum in mediating the switch between Brønsted and Lewis acidity, Chem. Sci. 12 (2021) 4094–4103. https://doi.org/10.1039/d0sc06130a.

[112] T. Juzsakova, A. Csavdari, Á. Rédey, T. Fráter, L. Dióssy, G.E. Popita, I. Ráduly, L.

Ráduly, J. Lauer, Study on the alkylaton mechanism of isobutane with 1-butene using environmental friendly catalysts, Environ. Eng. Manag. J. 13 (2014) 2343–2347. https://doi.org/10.30638/eemj.2014.261.

[113] M. Trachta, R. Bulánek, O. Bludský, M. Rubeš, Brønsted acidity in zeolites measured by deprotonation energy, Sci. Rep. 12 (2022). https://doi.org/10.1038/s41598-022-11354-x.

[114] H. Pang, G. Yang, L. Li, J. Yu, Efficient transesterification over two-dimensional zeolites for sustainable biodiesel production, Green Energy Environ. 5 (2020) 405–413. https://doi.org/10.1016/j.gee.2020.10.024.

[115] H. Xu, P. Wu, Two-dimensional zeolites in catalysis: current state-of-the-art and perspectives, Catal. Rev. - Sci. Eng. 63 (2021) 234–301. https://doi.org/10.1080/01614940.2021.1948298.

[116] A.T. Aguayo, A.E. Sánchez Del Campo, A.G. Gayubo, A. Tarrío, J. Bilbao, Deactivation by coke of a catalyst based on a SAPO-34 in the transformation of methanol into olefins, J. Chem. Technol. Biotechnol. 74 (1999) 315–321. https://doi.org/10.1002/(SICI)1097-4660(199904)74:4<315::AID-JCTB34>3.0.CO;2-G.

[117] H. Schulz, "Coking" of zeolites during methanol conversion: Basic reactions of the MTO-, MTP- and MTG processes, Catal. Today. 154 (2010) 183–194. https://doi.org/10.1016/j.cattod.2010.05.012.

[118] E. Catizzone, Z. Cirelli, A. Aloise, P. Lanzafame, M. Migliori, G. Giordano, Methanol conversion over ZSM-12, ZSM-22 and EU-1 zeolites: from DME to hydrocarbons production, Catal. Today. 304 (2018) 39–50. https://doi.org/10.1016/j.cattod.2017.08.037.

[119] M. Boronat, C. Martínez, A. Corma, Mechanistic differences between methanol and dimethyl ether carbonylation in side pockets and large channels of mordenite, Phys. Chem. Chem. Phys. 13 (2011) 2603–2612. https://doi.org/10.1039/c0cp01996h.

[120] Database of Zeolite Structures, Struct. Comm. Int. Zeolite Assoc. (2017). https://asia.iza-structure.org/IZA-SC/ftc_table.php.

[121] D. Masih, S. Rohani, J.N. Kondo, T. Tatsumi, Low-temperature methanol dehydration to dimethyl ether over various small-pore zeolites, Appl. Catal. B Environ. 217 (2017) 247–255. https://doi.org/10.1016/j.apcatb.2017.05.089.

[122] A.A. Rownaghi, F. Rezaei, M. Stante, J. Hedlund, Selective dehydration of methanol to dimethyl ether on ZSM-5 nanocrystals, Appl. Catal. B Environ. 119–120 (2012) 56–61. https://doi.org/10.1016/j.apcatb.2012.02.017.

[123] E. Catizzone, A. Aloise, E. Giglio, G. Ferrarelli, M. Bianco, M. Migliori, G. Giordano, MFI vs. FER zeolite during methanol dehydration to dimethyl ether: The crystal size plays a key role, Catal. Commun. 149 (2021) 106214. https://doi.org/10.1016/j.catcom.2020.106214.

[124] U. Olsbye, S. Svelle, M. Bjrgen, P. Beato, T.V.W. Janssens, F. Joensen, S. Bordiga, K.P. Lillerud, Conversion of methanol to hydrocarbons: How zeolite cavity and pore size controls product selectivity, Angew. Chemie - Int. Ed. 51 (2012) 5810–5831. https://doi.org/10.1002/anie.201103657.

[125] F. Schmidt, C. Hoffmann, F. Giordanino, S. Bordiga, P. Simon, W. Carrillo-Cabrera, S. Kaskel, Coke location in microporous and hierarchical ZSM-5 and the impact on the MTH reaction, J. Catal. 307 (2013) 238–245. https://doi.org/10.1016/j.jcat.2013.07.020.

[126] K. Krim, A. Sachse, A. Le Valant, Y. Pouilloux, S. Hocine, One Step Dimethyl Ether (DME) Synthesis from CO2 Hydrogenation over Hybrid Catalysts Containing Cu/ZnO/Al2O3 and Nano-Sized Hollow ZSM-5 Zeolites, Catal. Letters. 153 (2023) 83–94. https://doi.org/10.1007/s10562-022-03949-w.

[127] S.M.K. Aboul-Fotouh, L.I. Ali, M.A. Naghmash, N.A.K. Aboul-Gheit, Effect of the Si/Al ratio of HZSM-5 zeolite on the production of dimethyl ether before and after ultrasonication, Ranliao Huaxue Xuebao/Journal Fuel Chem. Technol. 45 (2017) 581–588. https://doi.org/10.1016/s1872-5813(17)30030-0.

[128] B. Sabour, M.H. Peyrovi, T. Hamoule, M. Rashidzadeh, Catalytic dehydration of methanol to dimethyl ether (DME) over Al-HMS catalysts, J. Ind. Eng. Chem. 20 (2014) 222–227. https://doi.org/10.1016/j.jiec.2013.03.044.

[129] N. Khandan, M. Kazemeini, M. Aghaziarati, Determining an optimum catalyst for liquid-phase dehydration of methanol to dimethyl ether, Appl. Catal. A Gen. 349 (2008) 6–12. https://doi.org/10.1016/j.apcata.2008.07.029.

[130] D. Mao, W. Yang, J. Xia, B. Zhang, Q. Song, Q. Chen, Highly effective hybrid catalyst for the direct synthesis of dimethyl ether from syngas with magnesium oxide-modified HZSM-5 as a dehydration component, J. Catal. 230 (2005) 140–149. https://doi.org/10.1016/j.jcat.2004.12.007.

[131] C.G. Pope, X-ray diffraction and the bragg equation, J. Chem. Educ. 74 (1997) 129–131. https://doi.org/10.1021/ed074p129.

[132] A. Ali, Y.W. Chiang, R.M. Santos, X-Ray Diffraction Techniques for Mineral Characterization: A Review for Engineers of the Fundamentals, Applications, and Research Directions, Minerals. 12 (2022). https://doi.org/10.3390/min12020205.

[133] N. Widjonarko, Introduction to Advanced X-ray Diffraction Techniques for Polymeric Thin Films, Coatings. 6 (2016) 54. https://doi.org/10.3390/coatings6040054.

[134] X-Ray Diffraction Laboratory, Univ. Alberta. (n.d.). https://cms.eas.ualberta.ca/xrd/how-xrd-works/.

[135] L. Chen, T.V.W. Janssens, M. Skoglundh, H. Grönbeck, Interpretation of NH 3 -TPD Profiles from Cu-CHA Using First-Principles Calculations, Top. Catal. 62 (2019). https://doi.org/10.1007/s11244-018-1095-y.

[136] K. Leistner, K. Xie, A. Kumar, K. Kamasamudram, L. Olsson, Ammonia Desorption Peaks Can Be Assigned to Different Copper Sites in Cu/SSZ-13, Catal. Letters. 147 (2017) 1882–1890. https://doi.org/10.1007/s10562-017-2083-8.

[137] M.O. Guerrero-Pérez, G.S. Patience, Experimental methods in chemical engineering: Fourier transform infrared spectroscopy—FTIR, Can. J. Chem. Eng. 98 (2020) 25–33. https://doi.org/10.1002/cjce.23664.

[138] I. Miletto, E. Catizzone, G. Bonura, C. Ivaldi, M. Migliori, E. Gianotti, L. Marchese, F. Frusteri, G. Giordano, In situ FT-IR characterization of CuZnZr/ferrierite hybrid catalysts for one-pot CO2-to-DME conversion, Materials (Basel). 11 (2018). https://doi.org/10.3390/ma11112275.

[139] A.G. Pelmenschikov, R.A. Van Santen, J. Jänchen, E. Meijer, CD3CN as a probe of Lewis and Bronsted acidity of zeolites, J. Phys. Chem. 97 (1993) 11071–11074. https://doi.org/10.1021/j100144a028.

[140] J.I. Goldstein, D.E. Newbury, J.R. Michael, N.W.M. Ritchie, J.H.J. Scott, D.C. Joy, Scanning electron microscopy and x-ray microanalysis, Springer New York, 2017. https://doi.org/10.1007/978-1-4939-6676-9.

[141] Susan Swapp (University of Wyoming), Geochemical Instrumentation and Analysis, (n.d.). https://serc.carleton.edu/research_education/geochemsheets/techniques/SEM.html.

[142] L.T. Gibson, Archaeometry and Antique Analysis - Metallic and Ceramic Objects, in: Encycl. Anal. Sci. Second Ed., Elsevier Inc., 2004: pp. 117–123. https://doi.org/10.1016/B0-12-369397-7/00020-0.

[143] D. Titus, E. James Jebaseelan Samuel, S.M. Roopan, Nanoparticle characterization techniques, in: Green Synth. Charact. Appl. Nanoparticles, Elsevier, 2018: pp. 303–319. https://doi.org/10.1016/B978-0-08-102579-6.00012-5.

[144] N. Saadatkhah, A. Carillo Garcia, S. Ackermann, P. Leclerc, M. Latifi, S. Samih, G.S. Patience, J. Chaouki, Experimental methods in chemical engineering: Thermogravimetric analysis—TGA, Can. J. Chem. Eng. 98 (2020) 34–43. https://doi.org/10.1002/cjce.23673.

[145] M. Migliori, A. Aloise, G. Giordano, Methanol to dimethylether on H-MFI catalyst: The influence of the Si/Al ratio on kinetic parameters, Catal. Today. 227 (2014) 138–143. https://doi.org/10.1016/j.cattod.2013.09.033.

[146] Z.A. Alothman, A review: Fundamental aspects of silicate mesoporous materials, Materials (Basel). 5 (2012) 2874–2902. https://doi.org/10.3390/ma5122874.

[147] A.J. Schwanke, R. Balzer, S. Pergher, Microporous and mesoporous materials from natural and inexpensive sources, in: Handb. Ecomater., Springer International Publishing, 2019: pp. 3379–3399. https://doi.org/10.1007/978-3-319-68255-6_43.

[148] O.D. Neikov, N.A. Yefimov, Powder Characterization and Testing, in: Handb. Non-Ferrous Met. Powders, Elsevier, 2019: pp. 3–62. https://doi.org/10.1016/b978-0-08-100543-9.00001-4.

[149] R. Bardestani, G.S. Patience, S. Kaliaguine, Experimental methods in chemical engineering: specific surface area and pore size distribution measurements—BET, BJH, and DFT, Can. J. Chem. Eng. 97 (2019) 2781–2791. https://doi.org/10.1002/cjce.23632.

[150] E. Santos, Nanostructure Materials as Catalysts for the Degradation of Polyolefins, UNIVERSIDADE DE LISBOA INSTITUTO SUPERIOR TÉCNICO, 2018. https://doi.org/10.13140/RG.2.2.12960.94726.

[151] A. Kalair, N. Abas, M.S. Saleem, A.R. Kalair, N. Khan, Role of energy storage systems in

energy transition from fossil fuels to renewables, Energy Storage. 3 (2021). https://doi.org/10.1002/est2.135.

[152] IEA (2022), Energy Statistics Data Browser, IEA, Paris https://www.iea.org/data-and-statistics/data-tools/energy-statistics-data-browser, n.d.

[153] E.M. Eaton, N.A. Day, Petro-pedagogy: fossil fuel interests and the obstruction of climate justice in public education, Environ. Educ. Res. 26 (2020) 457–473. https://doi.org/10.1080/13504622.2019.1650164.

[154] D. Liuzzi, C. Peinado, M.A. Peña, J. Van Kampen, J. Boon, S. Rojas, Increasing dimethyl ether production from biomass-derived syngas: via sorption enhanced dimethyl ether synthesis, Sustain. Energy Fuels. 4 (2020) 5674–5681. https://doi.org/10.1039/d0se01172j.

[155] J. Sun, G. Yang, Y. Yoneyama, N. Tsubaki, Catalysis chemistry of dimethyl ether synthesis, ACS Catal. 4 (2014) 3346–3356. https://doi.org/10.1021/cs500967j.

[156] K. Takeishi, Y. Wagatsuma, H. Ariga, K. Kon, K. ichi Shimizu, Promotional Effect of Water on Direct Dimethyl Ether Synthesis from Carbon Monoxide and Hydrogen Catalyzed by Cu-Zn/Al2O3, ACS Sustain. Chem. Eng. 5 (2017) 3675–3680. https://doi.org/10.1021/acssuschemeng.6b02915.

[157] F. Meshkini, M. Taghizadeh, M. Bahmani, Investigating the effect of metal oxide additives on the properties of Cu/ZnO/Al2O3 catalysts in methanol synthesis from syngas using factorial experimental design, Fuel. 89 (2010) 170–175. https://doi.org/10.1016/j.fuel.2009.07.007.

[158] N.D. Nielsen, A.D. Jensen, J.M. Christensen, The roles of CO and CO2 in high pressure methanol synthesis over Cu-based catalysts, J. Catal. 393 (2021) 324–334. https://doi.org/10.1016/j.jcat.2020.11.035.

[159] K. Chen, H. Fang, S. Wu, X. Liu, J. Zheng, S. Zhou, X. Duan, Y. Zhuang, S. Chi Edman Tsang, Y. Yuan, CO2 hydrogenation to methanol over Cu catalysts supported on La-modified SBA-15: The crucial role of Cu–LaOx interfaces, Appl. Catal. B Environ. 251 (2019) 119–129. https://doi.org/10.1016/j.apcatb.2019.03.059.

[160] M. Huš, V.D.B.C. Dasireddy, N. Strah Štefančič, B. Likozar, Mechanism, kinetics and thermodynamics of carbon dioxide hydrogenation to methanol on Cu/ZnAl2O4 spinel-type heterogeneous catalysts, Appl. Catal. B Environ. 207 (2017) 267–278. https://doi.org/10.1016/j.apcatb.2017.01.077.

[161] H. Heriyanto, O. Muraza, G.A. Nasser, M.A. Sanhoob, I.A. Bakare, Budhijanto, Rochmadi, A. Budiman, Development of New Kinetic Models for Methanol to Hydrocarbons over a Ca-ZSM-5 Catalyst, Energy and Fuels. 34 (2020) 6245–6260. https://doi.org/10.1021/acs.energyfuels.9b04327.

[162] A. Brunetti, M. Migliori, D. Cozza, E. Catizzone, G. Giordano, G. Barbieri, Methanol Conversion to Dimethyl Ether in Catalytic Zeolite Membrane Reactors, ACS Sustain. Chem. Eng. 8 (2020) 10471–10479. https://doi.org/10.1021/acssuschemeng.0c02557.

[163] M.A. Armenta, V.M. Maytorena, R. Silva–Rodrigo, L.A. Flores-Sánchez, J.M. Quintana,

A. Olivas, R. Silva-Rodrigo, L.A. Flores-Sánchez, J.M. Quintana, A. Olivas, Effect of acidity on ferric oxide nanoparticles supported on γ–χ–Al2O3 in the methanol dehydration reaction toward dimethyl ether, Fuel. 296 (2021) 120618. https://doi.org/10.1016/j.fuel.2021.120618.

[164] Y. Sang, H. Liu, S. He, H. Li, Q. Jiao, Q. Wu, K. Sun, Catalytic performance of hierarchical H-ZSM-5/MCM-41 for methanol dehydration to dimethyl ether, J. Energy Chem. 22 (2013) 769–777. https://doi.org/10.1016/S2095-4956(13)60102-3.

[165] G. Bellussi, A. Carati, C. Rizzo, R. Millini, New trends in the synthesis of crystalline microporous materials, Catal. Sci. Technol. 3 (2013) 833–857. https://doi.org/10.1039/c2cy20510f.

[166] J. Čjka, O. V. Shvets, N. Kasian, A. Zukal, J. Pinkas, The role of template structure and synergism between inorganic and organic structure directing agents in the synthesis of utl zeolite, Chem. Mater. 22 (2010) 3482–3495. https://doi.org/10.1021/cm1006108.

[167] M. Ghavipour, A.S. Mehr, Y. Wang, R.M. Behbahani, S. Hajimirzaee, K. Bahrami, Investigating the mixing sequence and the Si content in SAPO-34 synthesis for selective conversion of methanol to light olefins using morpholine / TEAOH templates, RSC Adv. 6 (2016) 17583–17594. https://doi.org/10.1039/c5ra23432h.

[168] H. Robson, KFI High-silica KFI Si(79), Al(21), in: Verif. Synth. Zeolitic Mater., Second Rev, Elsevier Science Ltd, 2001: pp. 174–176. https://doi.org/https://doi.org/10.1016/B978-0-444-50703-7.X5094-7.

[169] Q. Ke, T. Sun, X. Wei, Y. Guo, S. Xu, S. Wang, Economical synthesis strategy of RHO zeolites with fine-tuned composition and porosity for enhanced trace CO2 capture, Chem. Eng. J. 359 (2019) 344–353. https://doi.org/10.1016/j.cej.2018.11.098.

[170] J. Grand, N. Barrier, M. Debost, E.B. Clatworthy, F. Laine, P. Boullay, N. Nesterenko, J.P. Dath, J.P. Gilson, S. Mintova, Flexible Template-Free RHO Nanosized Zeolite for Selective CO2Adsorption, Chem. Mater. 32 (2020) 5985–5993. https://doi.org/10.1021/acs.chemmater.0c01016.

[171] Z. Guo, X. Zhang, Y. Kang, J. Zhang, Biomass-Derived Carbon Sorbents for Cd(II) Removal: Activation and Adsorption Mechanism, ACS Sustain. Chem. Eng. 5 (2017) 4103–4109. https://doi.org/10.1021/acssuschemeng.7b00061.

[172] M.R. Gafurov, I.N. Mukhambetov, B. V. Yavkin, G. V. Mamin, A.A. Lamberov, S.B. Orlinskii, Quantitative Analysis of Lewis Acid Centers of γ-Alumina by Using EPR of the Adsorbed Anthraquinone as a Probe Molecule: Comparison with the Pyridine, Carbon Monoxide IR, and TPD of Ammonia, J. Phys. Chem. C. 119 (2015) 27410–27415. https://doi.org/10.1021/acs.jpcc.5b09759.

[173] S. Van De Vyver, Y. Román-Leshkov, Metalloenzyme-Like Zeolites as Lewis Acid Catalysts for C-C Bond Formation, Angew. Chemie - Int. Ed. 54 (2015) 12554–12561. https://doi.org/10.1002/anie.201503701.

[174] E. Catizzone, M. Migliori, A. Purita, G. Giordano, Ferrierite vs. Γ-Al2O3: The superiority of zeolites in terms of water-resistance in vapour-phase dehydration of methanol to

dimethyl ether, J. Energy Chem. 30 (2019) 162–169. https://doi.org/10.1016/j.jechem.2018.05.004.

[175] E. Catizzone, A. Aloise, M. Migliori, G. Giordano, The effect of FER zeolite acid sites in methanol-to-dimethyl-ether catalytic dehydration, J. Energy Chem. 26 (2017) 406–415. https://doi.org/10.1016/j.jechem.2016.12.005.

[176] A.G. Olabi, M.A. Abdelkareem, Renewable energy and climate change, Renew. Sustain. Energy Rev. 158 (2022). https://doi.org/10.1016/j.rser.2022.112111.

[177] C.J. Li, Y.J. Zhang, H. Chen, P.Y. He, Highly-effective production of renewable energy dimethyl ether over geopolymer-based ferrierite, Fuel. 293 (2021). https://doi.org/10.1016/j.fuel.2021.120486.

[178] G. Issayev, B.R. Giri, A.M. Elbaz, K.P. Shrestha, F. Mauss, W.L. Roberts, A. Farooq, Ignition delay time and laminar flame speed measurements of ammonia blended with dimethyl ether: A promising low carbon fuel blend, Renew. Energy. 181 (2022) 1353–1370. https://doi.org/10.1016/j.renene.2021.09.117.

[179] A. Tripathi, S. Park, S. Park, A.K. Agarwal, Prospects of Dual-Fuel Injection System in Compression Ignition (CI) Engines Using Di-Methyl Ether (DME), in: Energy, Environ. Sustain., Springer Nature, 2022: pp. 223–259. https://doi.org/10.1007/978-981-16-8344-2_9.

[180] S. Michailos, S. McCord, V. Sick, G. Stokes, P. Styring, Dimethyl ether synthesis via captured CO2 hydrogenation within the power to liquids concept: A techno-economic assessment, Energy Convers. Manag. 184 (2019) 262–276. https://doi.org/10.1016/j.enconman.2019.01.046.

[181] K. Im-orb, P. Piroonlerkgul, Sustainability analysis of the bio-dimethyl ether (bio-DME) production via integrated biomass gasification and direct DME Synthesis Process, Renew. Energy. 208 (2023) 324–330. https://doi.org/10.1016/j.renene.2023.03.092.

[182] M.A. Armenta, V.M. Maytorena, D.A. Buentello-Montoya, E. Arroyo, M. Cota-Leal, D. Yong, A. Olivas, Effect of catalytic hydrodynamics over microagglomerates of Mn2O3 and PdO supported on γ-χ-Al2O3 for dimethyl ether production, Fuel. 317 (2022). https://doi.org/10.1016/j.fuel.2022.123509.

[183] F. Li, M. Ao, G. Hung Pham, Y. Jin, M. Hoang Nguyen, N. Majd Alawi, M.O. Tade, S. Liu, A novel UiO-66 encapsulated 12-silicotungstic acid catalyst for dimethyl ether synthesis from syngas, Catal. Today. 355 (2020) 3–9. https://doi.org/10.1016/j.cattod.2019.07.057.

[184] Y. Tao, H. Kanoh, L. Abrams, K. Kaneko, Mesopore-modified zeolites: Preparation, characterization, and applications, Chem. Rev. 106 (2006) 896–910. https://doi.org/10.1021/cr040204o.

[185] N. Kosinov, J. Gascon, F. Kapteijn, E.J.M. Hensen, Recent developments in zeolite membranes for gas separation, J. Memb. Sci. 499 (2016) 65–79. https://doi.org/10.1016/j.memsci.2015.10.049.

[186] Q. Tang, H. Xu, Y. Zheng, J. Wang, H. Li, J. Zhang, Catalytic dehydration of methanol to

dimethyl ether over micro-mesoporous ZSM-5/MCM-41 composite molecular sieves, Appl. Catal. A Gen. 413–414 (2012) 36–42. https://doi.org/10.1016/j.apcata.2011.10.039.

[187] D. Jin, B. Zhu, Z. Hou, J. Fei, H. Lou, X. Zheng, Dimethyl ether synthesis via methanol and syngas over rare earth metals modified zeolite Y and dual Cu-Mn-Zn catalysts, Fuel. 86 (2007) 2707–2713. https://doi.org/10.1016/j.fuel.2007.03.011.

[188] E. Catizzone, A. Aloise, M. Migliori, G. Giordano, Dimethyl ether synthesis via methanol dehydration: Effect of zeolite structure, Appl. Catal. A Gen. 502 (2015) 215–220. https://doi.org/10.1016/j.apcata.2015.06.017.

[189] M. Rutkowska, D. Macina, Z. Piwowarska, M. Gajewska, U. Díaz, L. Chmielarz, Hierarchically structured ZSM-5 obtained by optimized mesotemplate-free method as active catalyst for methanol to DME conversion, Catal. Sci. Technol. 6 (2016) 4849–4862. https://doi.org/10.1039/c6cy00040a.

[190] L. Sommer, D. Mores, S. Svelle, M. Stöcker, B.M. Weckhuysen, U. Olsbye, Mesopore formation in zeolite H-SSZ-13 by desilication with NaOH, Microporous Mesoporous Mater. 132 (2010) 384–394. https://doi.org/10.1016/j.micromeso.2010.03.017.

[191] A. Aloise, A. Marino, F. Dalena, G. Giorgianni, M. Migliori, L. Frusteri, C. Cannilla, G. Bonura, F. Frusteri, G. Giordano, Desilicated ZSM-5 zeolite: Catalytic performances assessment in methanol to DME dehydration, Microporous Mesoporous Mater. 302 (2020) 110198. https://doi.org/https://doi.org/10.1016/j.micromeso.2020.110198.

[192] R. Simancas, D. Dari, N. Velamazán, M.T. Navarro, A. Cantín, J.L. Jordá, G. Sastre, A. Corma, F. Rey, Modular organic structure-directing agents for the synthesis of zeolites, Science (80-.). 330 (2010) 1219–1222. https://doi.org/10.1126/science.1196240.

[193] M. Zaarour, B. Dong, I. Naydenova, R. Retoux, S. Mintova, Progress in zeolite synthesis promotes advanced applications, Microporous Mesoporous Mater. 189 (2014) 11–21. https://doi.org/10.1016/j.micromeso.2013.08.014.

[194] J. Kim, S.J. Cho, D.H. Kim, Facile Synthesis of KFI-type Zeolite and Its Application to Selective Catalytic Reduction of NOx with NH3, ACS Catal. 7 (2017) 6070–6081. https://doi.org/10.1021/acscatal.7b00697.

[195] H. Robson, Verified Syntheses of Zeolitic Materials, Elsevier, 2001. https://doi.org/10.1016/B978-0-444-50703-7.X5094-7.

[196] M. Auta, B.H. Hameed, Modified mesoporous clay adsorbent for adsorption isotherm and kinetics of methylene blue, Chem. Eng. J. 198–199 (2012) 219–227. https://doi.org/10.1016/j.cej.2012.05.075.

[197] Z. Chen, X. Li, Y. Xu, Y. Dong, W. Lai, W. Fang, X. Yi, Fabrication of nano-sized SAPO-11 crystals with enhanced dehydration of methanol to dimethyl ether, Catal. Commun. 103 (2018) 1–4. https://doi.org/10.1016/j.catcom.2017.09.002.

[198] F. Chen, Z. Zhang, Q. Yang, Y. Yang, Z. Bao, Q. Ren, Microporous Carbon Adsorbents Prepared by Activating Reagent-Free Pyrolysis for Upgrading Low-Quality Natural Gas, ACS Sustain. Chem. Eng. 8 (2020) 977–985. https://doi.org/10.1021/acssuschemeng.9b05627.

[199] V. Sanchez Escribano, G. Garbarino, E. Finocchio, G. Busca, γ-Alumina and Amorphous Silica–Alumina: Structural Features, Acid Sites and the Role of Adsorbed Water, Top. Catal. 60 (2017) 1554–1564. https://doi.org/10.1007/s11244-017-0838-5.

[200] L. Čapek, J. Dědeček, B. Wichterlová, Co-beta zeolite highly active in propane-SCR-NOx in the presence of water vapor: Effect of zeolite preparation and A1 distribution in the framework, J. Catal. 227 (2004) 352–366. https://doi.org/10.1016/j.jcat.2004.08.001.

[201] X. Meng, F. Nawaz, F.S. Xiao, Templating route for synthesizing mesoporous zeolites with improved catalytic properties, Nano Today. 4 (2009) 292–301. https://doi.org/10.1016/j.nantod.2009.06.002.

[202] E. Catizzone, M. Migliori, A. Aloise, R. Lamberti, G. Giordano, Hierarchical low si/al ratio ferrierite zeolite by sequential postsynthesis treatment: Catalytic assessment in dehydration reaction of methanol, J. Chem. 2019 (2019). https://doi.org/10.1155/2019/3084356.

APPENDICES

Appendix A: XRD Pattern of RHO Zeolites, Particle Size Distributions, and Reproducibility Experiments

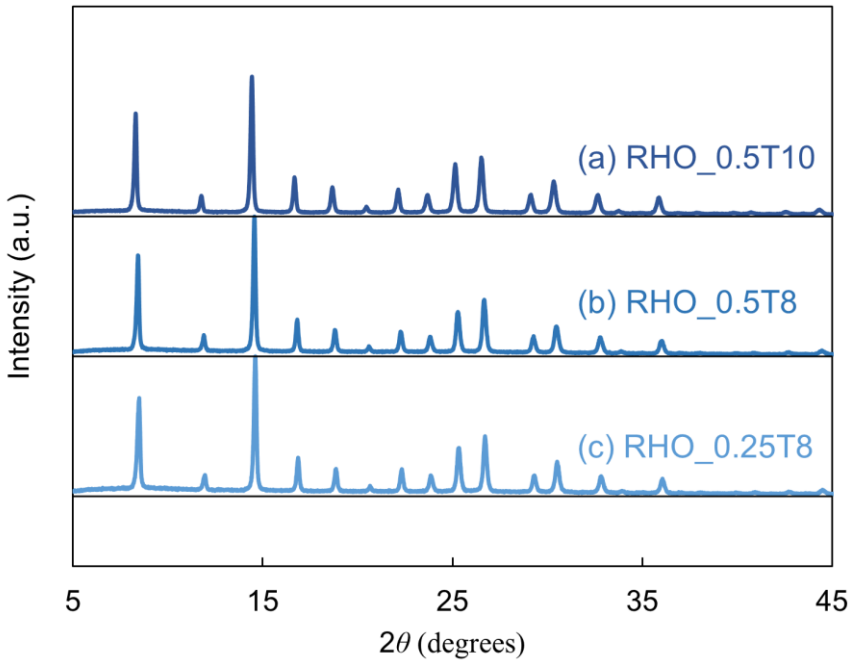

Figure 53. XRD patters of RHO zeolites including (a) RHO_0.5T10, (b) RHO_0.5T8, and (c) RHO_0.25T6 after activation by 1 M NH_4Cl solution.

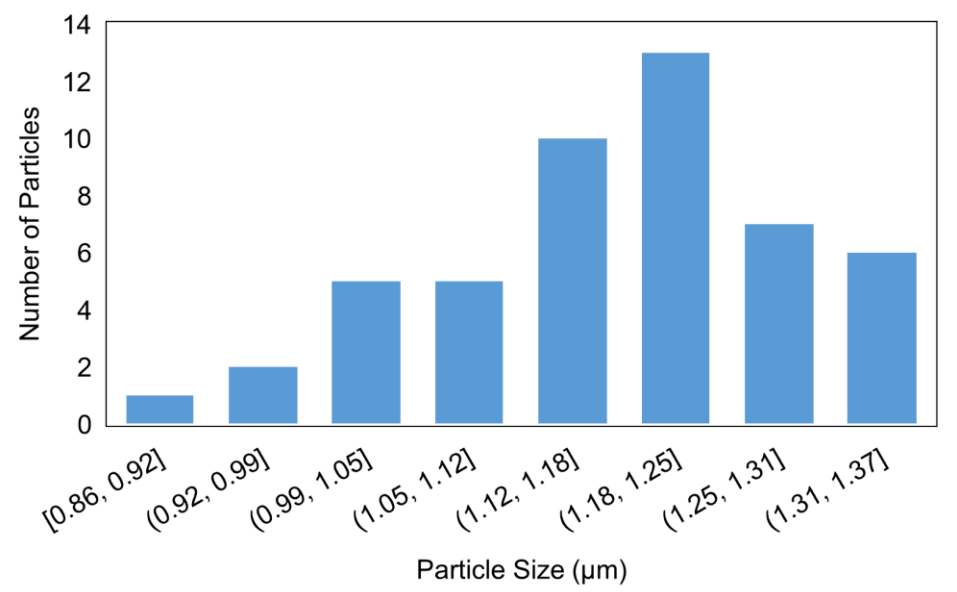

Figure 54. Particle size distribution for RHO_0.5T6 using SEM images.

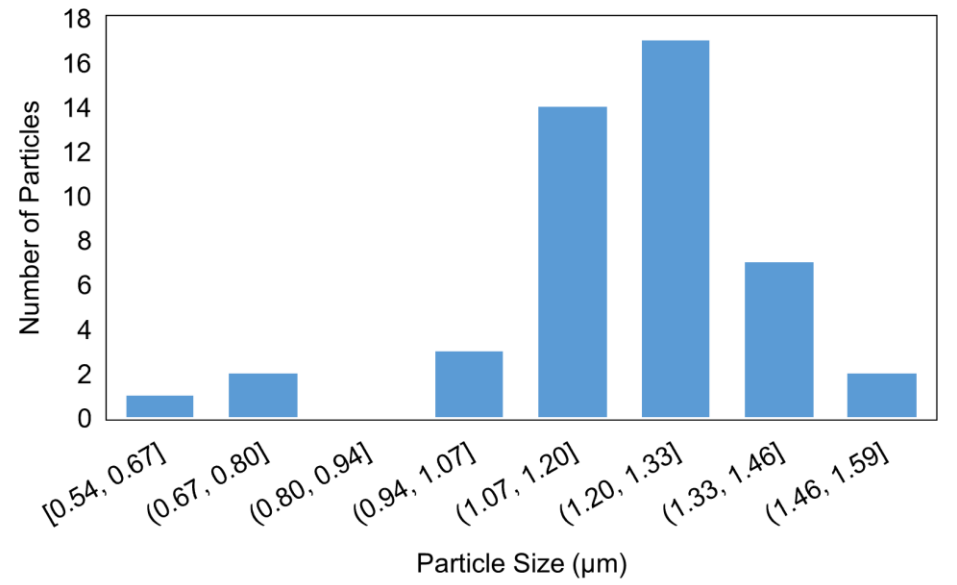

Figure 55. Particle size distribution for RHO_0.5T8 using SEM images

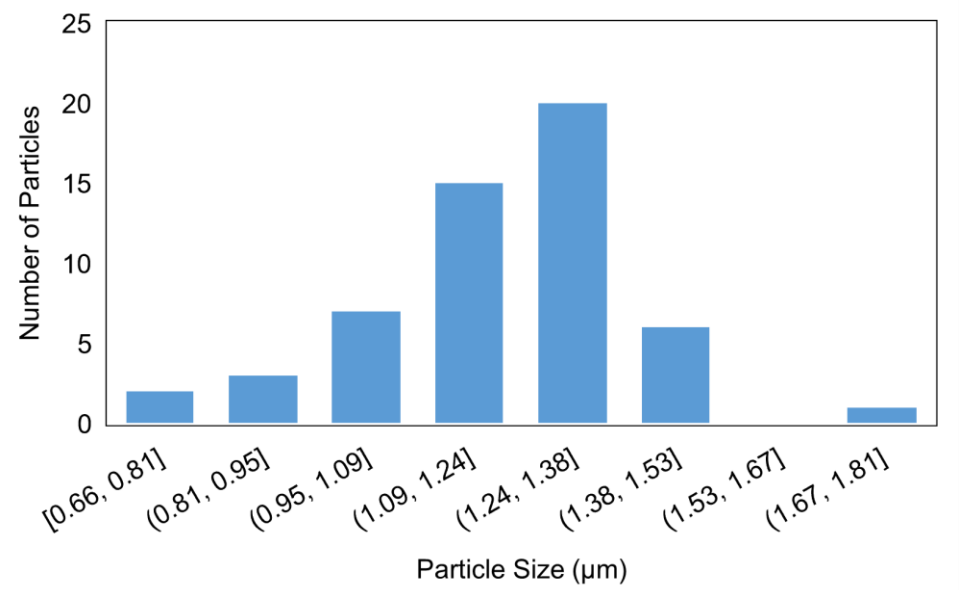

Figure 56. Particle size distribution for RHO_0.5T10 using SEM images

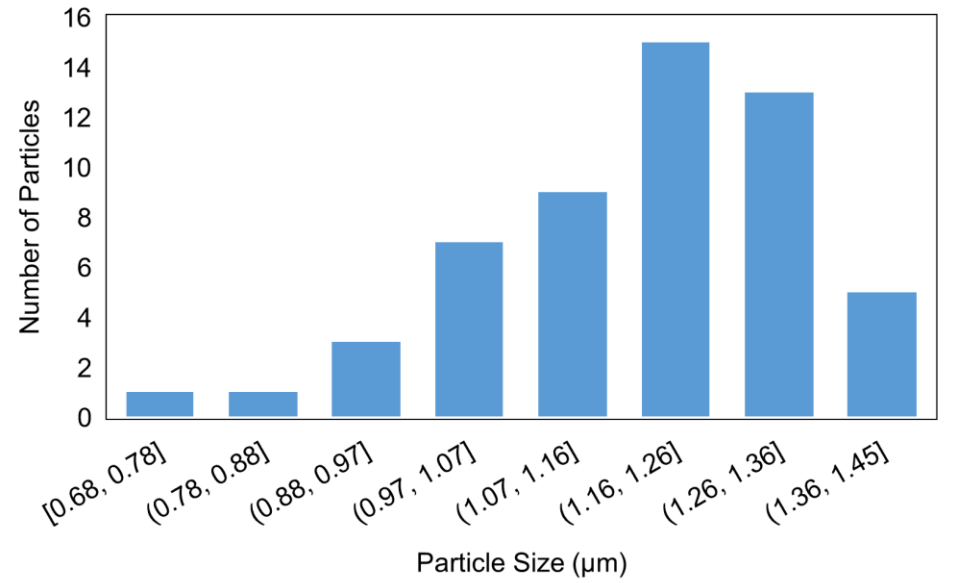

Figure 57. Particle size distribution for RHO_0.25T6 using SEM images

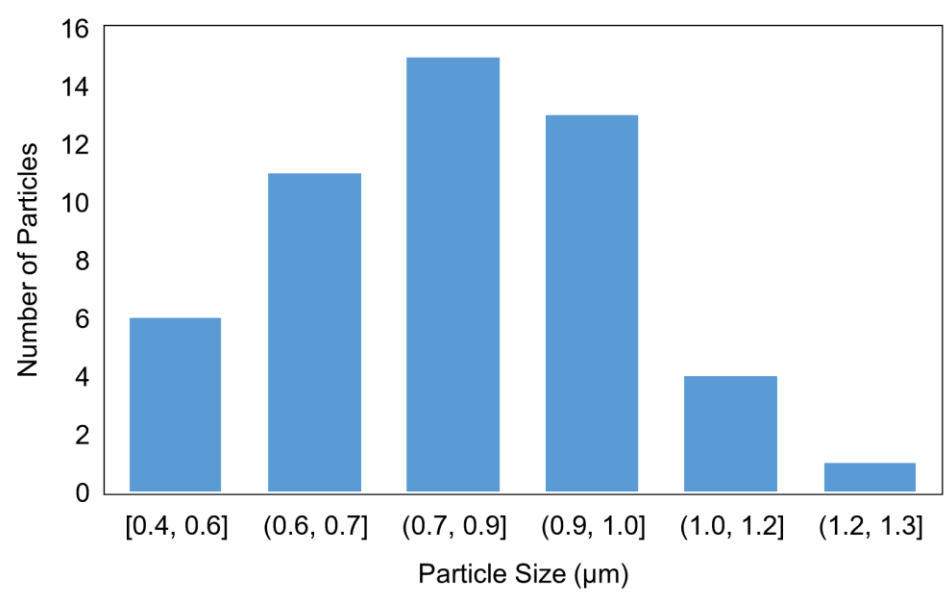

Figure 58. Particle size distribution for RHO_0T7 using SEM images.

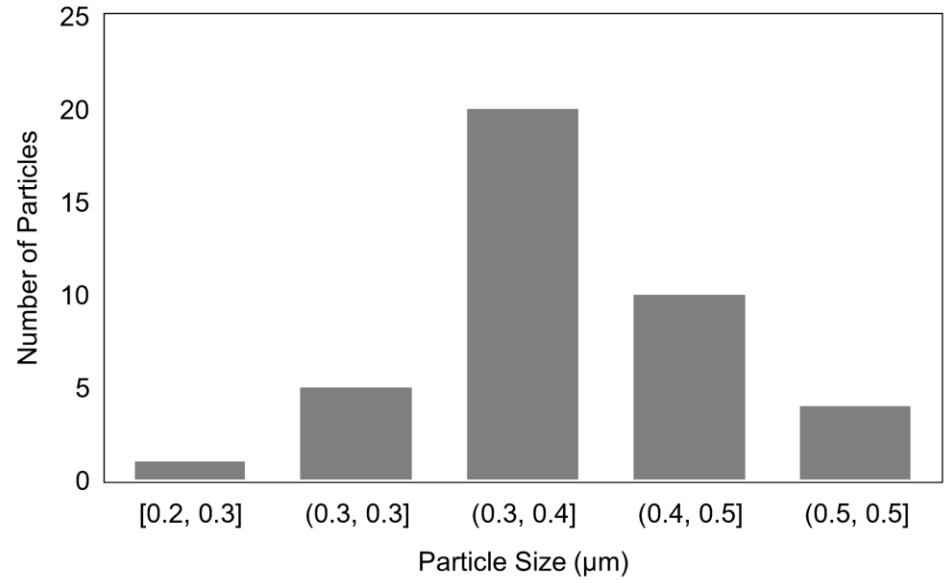

Figure 59. Particle size distribution for MFI_25 using SEM images.

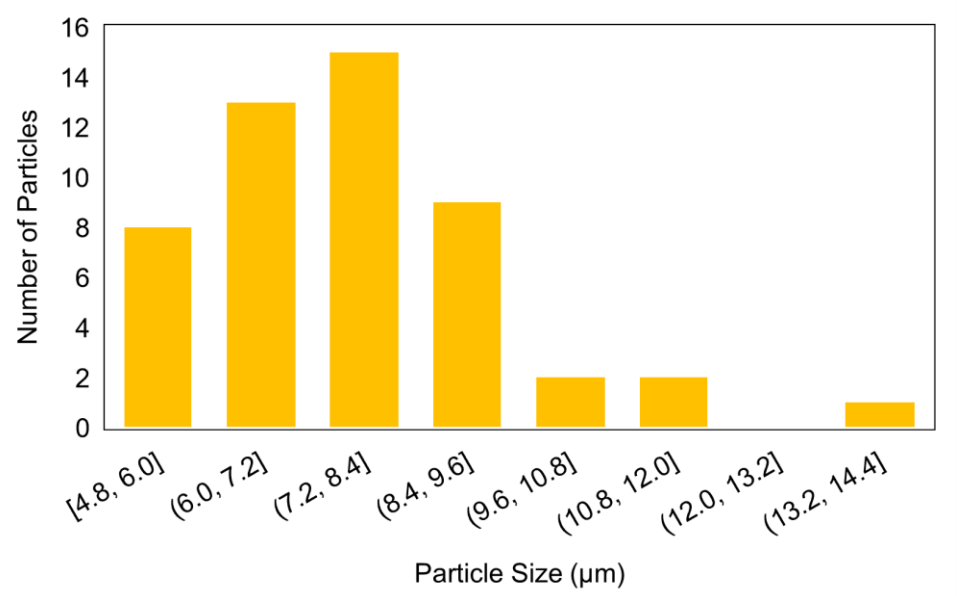

Figure 60. Particle size distribution for MFI_15 using SEM images.

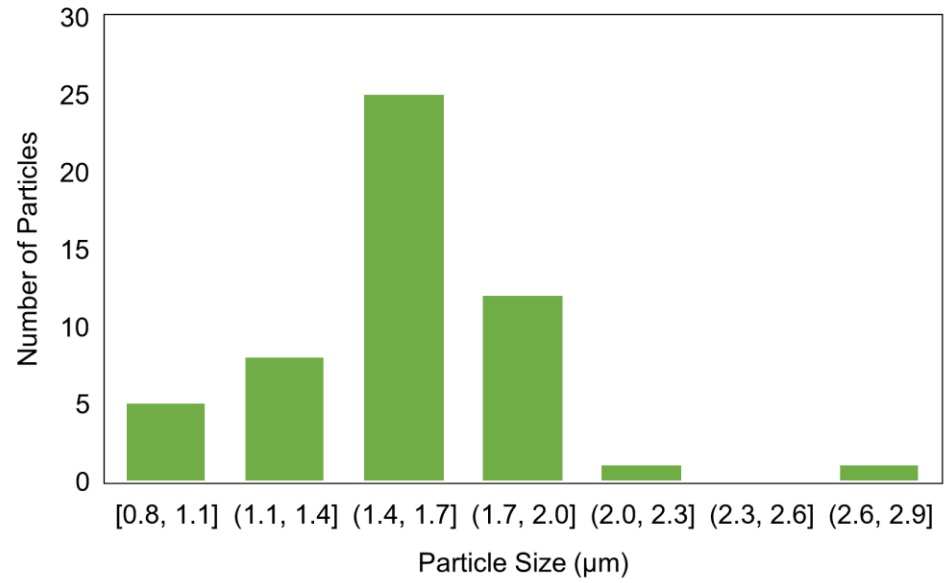

Figure 61. Particle size distribution for KFI_1T3 using SEM images.

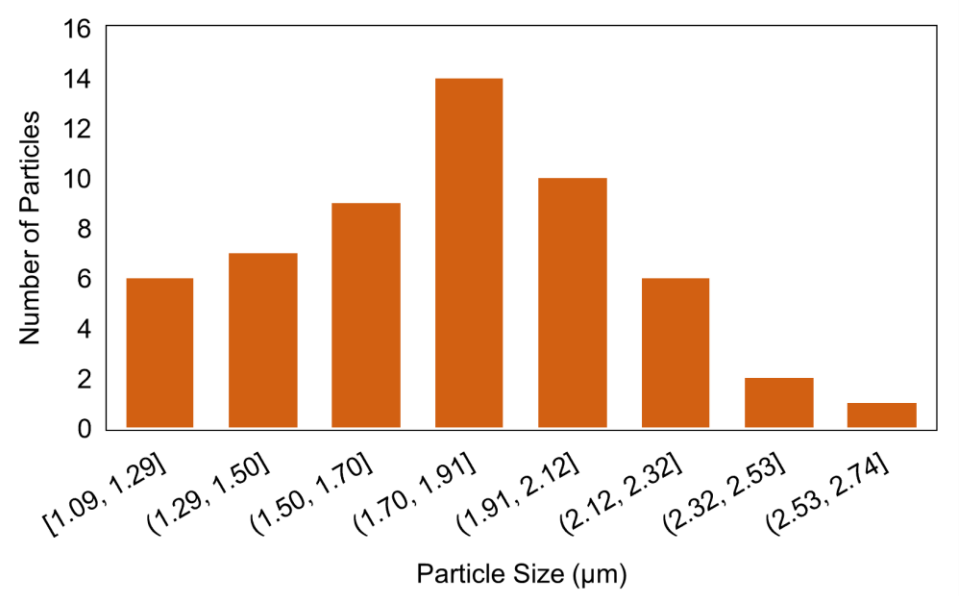

Figure 62. Particle size distribution for KFI_1T5 using SEM images.

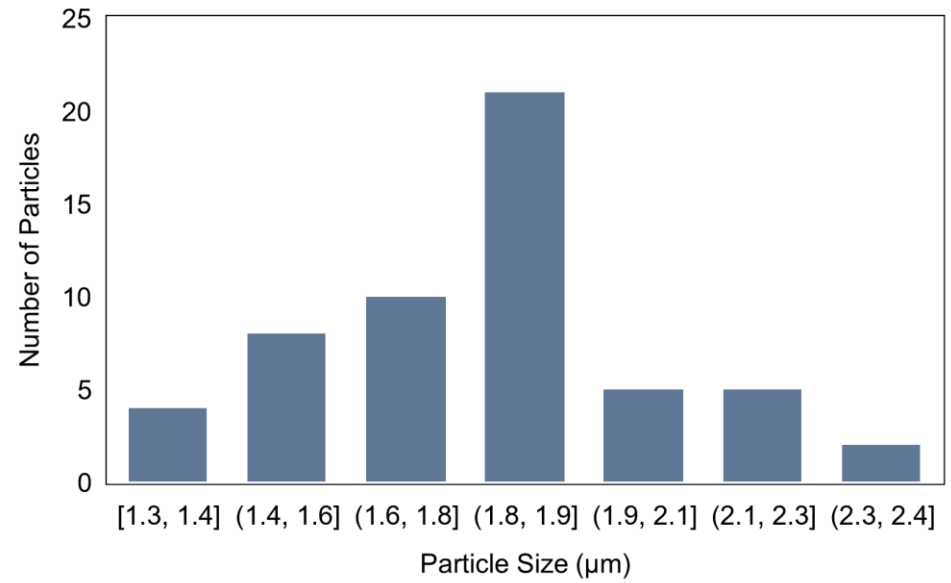

Figure 63. Particle size distribution for KFI_1T7 using SEM images.

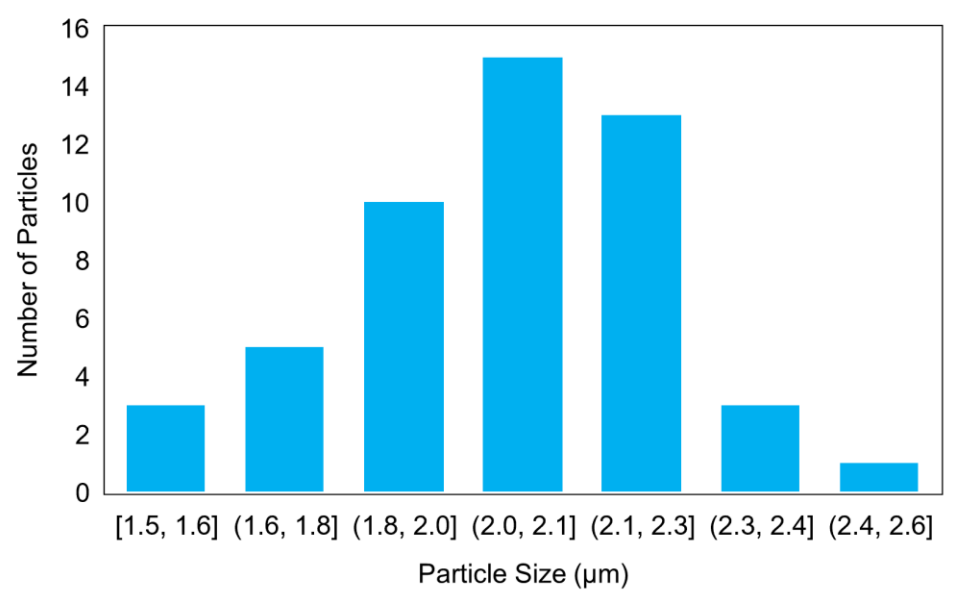

Figure 64. Particle size distribution for KFI_0.5T5 using SEM images.

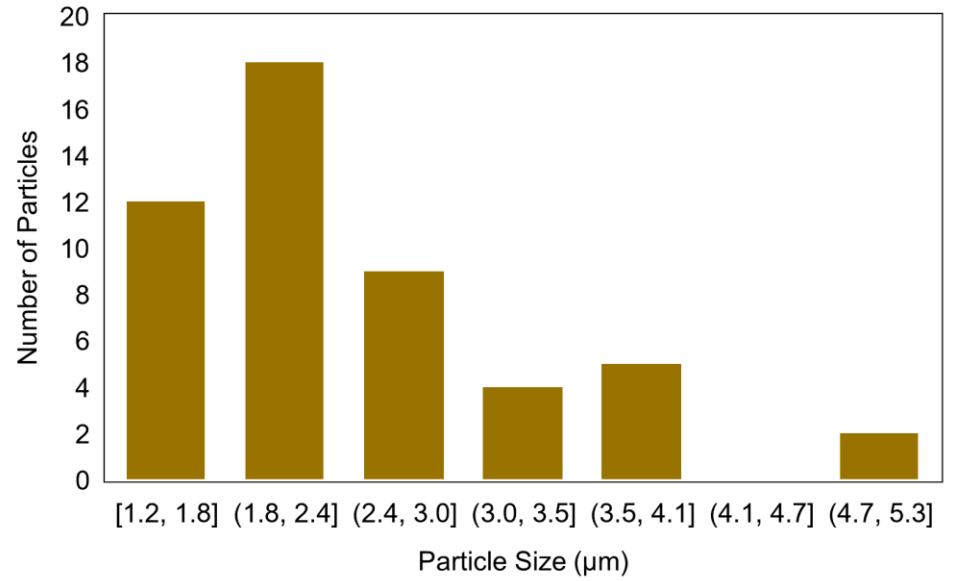

Figure 65. Particle size distribution for KFI_0T5 using SEM images.

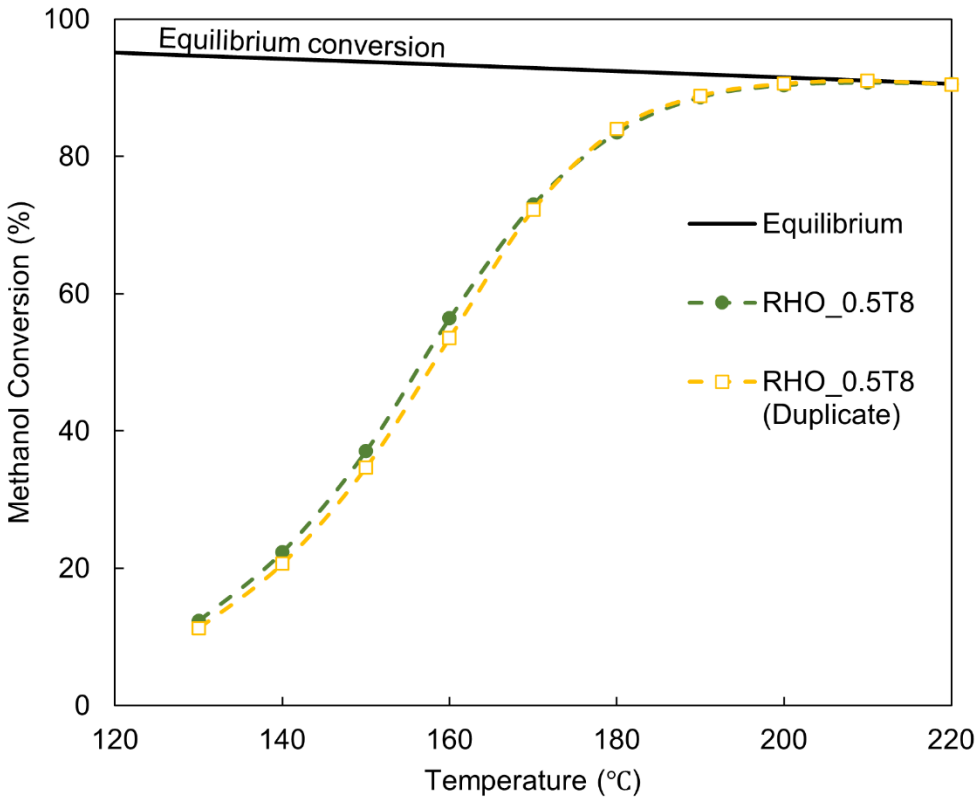

Figure 66. The methanol dehydration using prepared RHO_0.5T8 zeolites in two series at 130 – 220 °C with WHSV = 4 h^{-1}.

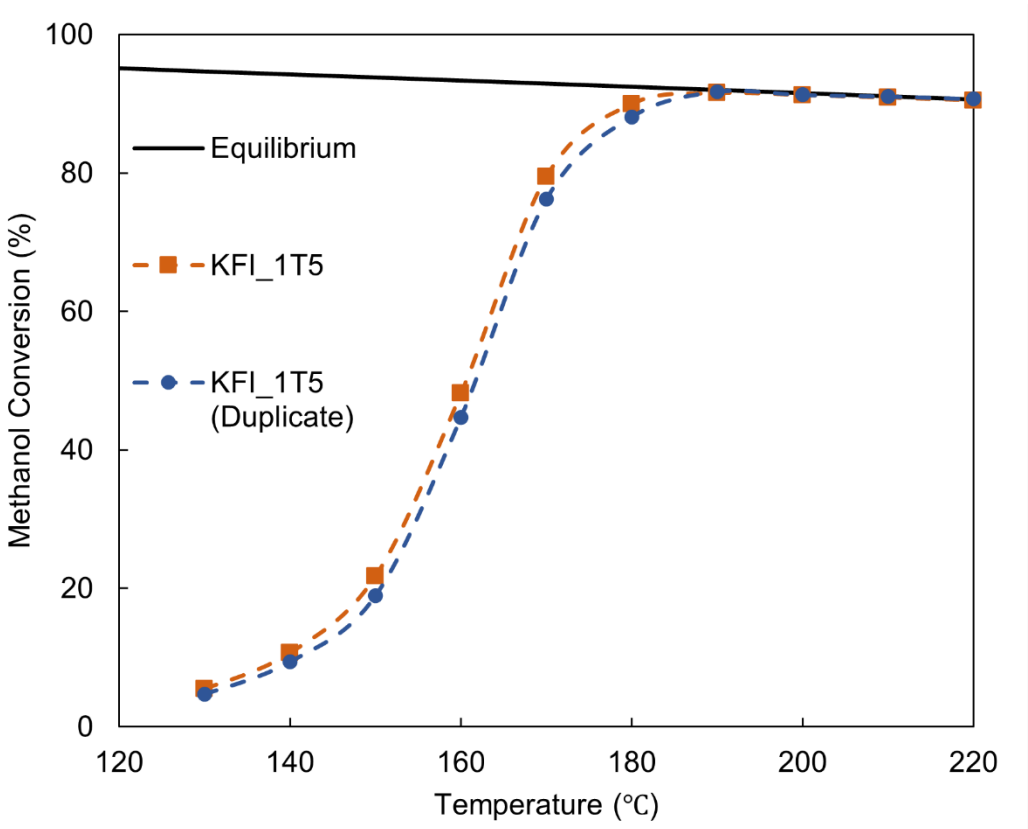

Figure 67. The methanol conversion over two different prepared KFI_1T5 samples at 130 – 220 ℃ with WHSV = 4 h^{-1}.